5-2023

The Effects of Carbon Coating on the Electrochemical Performance of Metal-Oxide Short Fiber Anodes for Lithium-Ion Batteries

David A. Sanchez
The University of Texas Rio Grande Valley

THE EFFECTS OF CARBON COATING ON THE ELECTROCHEMICAL PERFORMANCE OF METAL-OXIDE SHORT FIBER ANODES FOR LITHIUM-ION BATTERIES

A Thesis

by

DAVID A. SANCHEZ

Submitted in Partial Fulfillment of the

Requirements for the Degree of

MASTER OF SCIENCE IN ENGINEERING

Major Subject: Mechanical Engineering

The University of Texas Rio Grande Valley

May 2023

THE EFFECTS OF CARBON COATING ON THE ELECTROCHEMICAL PERFORMANCE OF METAL-OXIDE SHORT FIBER ANODES FOR LITHIUM-ION BATTERIES

A Thesis
by
DAVID A. SANCHEZ

COMMITTEE MEMBERS

Dr. Mataz Alcoutlabi
Chair of Committee

Dr. Ali Ashraf
Committee Member

Dr. Javier Ortega
Committee Member

May 2023

ABSTRACT

Sanchez, David A., The Effects of Carbon Coating on the Electrochemical Performance of Metal-Oxide Short Fiber Anodes for Lithium-Ion Batteries. Master of Science in Engineering (MSE), May, 2023, 95 pp., 21 tables, 57 figures, references, 107 titles.

This thesis focuses on the process of oxidizing centrifugally spun precursor fibers and the subsequent process of carbon coating via chemical vapor deposition (CVD) for use as anode material in lithium-ion batteries (LIBs). Metal oxides have been studied as a potential replacement for graphite as they have been shown to have high theoretical capacities, good electronic conductivity, and can be synthesized using low-cost, scalable methods. However, metal oxides with high theoretical capacities also have low cycle life. To avoid this, metal oxides have been integrated with carbon to expand their life cycle. The work in this thesis shows the synthesis of SnO_2/TiO_2 composite short fibers with different ratios, followed by the deposition of carbon to be used as active material for LIB anodes. When tested, SnO_2/TiO_2 (3:1) CVD with a deposition time of 60-min demonstrated a specific capacity of 499 mAh g^{-1} and capacity retention of 111% after 100 cycles. In comparison, the 30-min had a specific capacity of 653 mAh g^{-1} after 61 cycles and is projected to have a capacity retention of 93.2% after 100 cycles. The results were individually compared to the non-coated and parent materials of SnO_2 and TiO_2.

DEDICATION

I want to take the time to thank my family, who has been the driving force behind my success in earning a master's degree, and I am thankful to them for their love, support, and motivation. Specifically, my parents, Mario and Maria Sanchez have always encouraged me to strive for excellence in all aspects of my life. Their unwavering guidance and sacrifices have helped shape my academic and personal endeavors. Additionally, I owe a debt of gratitude to my devoted spouse, Chanel Borrego, who has provided me with the foundation of encouragement, motivation, and support crucial to achieving my academic aspirations. Her patience, understanding, and affection have allowed me to focus entirely on my educational goals. Lastly, I would like to thank my son, Elam Sanchez, whose smile and unconditional love have motivated me to work harder and be the best version of myself. I dedicate this achievement to my family, who have been my biggest cheerleaders and source of joy and happiness.

ACKNOWLEDGMENTS

I am incredibly thankful for my thesis committee members, who have been invaluable in assisting me with my master's thesis. Their continual encouragement, direction, and experience have been essential in formulating my research and ensuring its successful completion. My thesis committee chair, Dr. Mataz Alcoutlabi, has been a fantastic mentor throughout my educational journey. His scope of knowledge, commitment, and unquestionable support has been a tremendous source of motivation for me. I would also like to sincerely thank Dr. Ali Ashraf and Dr. Javier Ortega for their precious insights, constructive feedback, and support. Their expertise and guidance were crucial in shaping my research and aiding me in overcoming the difficulties of graduate studies.

Additionally, I would like to acknowledge my colleagues at the lithium-ion battery lab, who kept the atmosphere entertaining and encouraging during some of the most strenuous periods of my research. I owe much of my success to their assistance, companionship, and hilarity. They kept me centered, motivated, and energized during the research. I'm grateful for their kinship and aid, making this experience enjoyable and unforgettable. Without them, this accomplishment wouldn't have been achievable.

TABLE OF CONTENTS

Page

LIST OF TABLES

Page

LIST OF FIGURES

Page

CHAPTER I

INTRODUCTION

The world's reliance on fossil fuels has significantly affected the climate crisis. In response, lithium-ion batteries (LIBs) have emerged as a promising alternative to help reduce our dependence on these non-renewable resources and transition towards a cleaner, more sustainable energy future. Lithium-ion batteries (LIBs) are rechargeable batteries that have gained widespread use in electronics, electric vehicles, and grid storage systems due to their high energy density and efficiency [1, 2]. The cathode of a lithium-ion battery is typically made of lithium cobalt oxide (LCO) [3, 4], lithium manganese oxide (LMO) [4-6], or lithium iron phosphate (LFP) [4, 6, 7]. In contrast, the anode is typically graphite.

The use of graphite as the anode material is limited by its low capacity and poor rate performance due to the growth of dendrites [8]. As a result, significant research has been done into alternative materials for the anode of lithium-ion batteries. Some promising materials investigated include silicon, tin, and graphene.

Silicon is a potential material as an anode for its low discharge potential and high capacity for lithium storage, with a theoretical capacity of approximately 4200 mAh g^{-1}, which is more than ten times higher than that of graphite (372 mAh g^{-1}) [9, 10]. However, silicon suffers

from significant volume expansion upon lithium insertion, which can lead to mechanical failure of the anode [10]. Researchers have explored silicon-based composite materials and silicon nanostructures to overcome this limitation, which can mitigate the volume expansion issue [11-13].

Tin also has a high lithium storage capacity of 994 mAh g^{-1} but suffers from significant volume expansion like silicon, which causes the anode to pulverize and lowers its cyclability [14, 15]. Researchers have synthesized tin-based nanostructures [16] to overcome this limitation and have used oxidized tin materials [17-19].

Graphene is similar to graphite, but graphene is a single layer of carbon atoms arranged in a hexagonal lattice. Graphene has been researched as an alternative anode because it has high electrical conductivity and higher capacity than its counterpart with ~540 mAh g^{-1} [20-22]. Its downside is that it is difficult to produce large quantities and is expensive [23].

Overall, silicon, tin, and graphene are promising materials for LIB anodes. Nevertheless, each material has limitations, and further research is needed to optimize its performance and overcome them. One method that researchers have experimented with to improve the materials for anodes is by incorporating carbon into the material via a method called chemical vapor deposition (CVD). CVD is a process that involves the decomposition of a chemical precursor by heating it to a high temperature resulting in the growth of a thin film on a substrate. In recent years, CVD has synthesized graphene and other two-dimensional materials for lithium-ion batteries. The advantage of using CVD to synthesize graphene is that it allows for the growth of high-quality graphene with a large surface area and a uniform thickness. Additionally, CVD can synthesize graphene on a large scale, making it a potential route for the commercial production

of graphene-based materials [24]. There have been studies on using CVD-synthesized graphene as an anode material for lithium-ion batteries [25]. For example, researchers have demonstrated that CVD-synthesized graphene can be a high-performance anode material in lithium-ion batteries due to its high electrical conductivity, high surface area, and good stability during charge/discharge cycling [26-28].

Another method researchers have used to improve the performances of active materials is by experimenting on their structure and making composites with the help of nanofibers. Nanofibers have been widely used for their flexibility, affordability, and ease of production for many applications, such as water purification, air filtration, sensors, and various biomedical applications [29]. The ease of production of these fibers has been mainly due to the methods used: drawing, template synthesis, self-assembly, and electrospinning [30]. Electrospinning has been a popular method recently, but the method of centrifugal spinning (CS) has been gaining attention recently due to its versatility in using different solutions and melts [31-35]. CS uses centrifugal forces to expel a polymer solution (or melt) through a spinneret causing long fibers to be collected on surrounding pillars. CS produces fibers similar to electrospinning but at a higher production rate making it a newly popular method [36, 37] .

The fiber morphology and structure tremendously affect their properties and performance. For example, long nanofibers have been used in the biomedical field for their flexibility and size in applications such as wound dressings, tissue scaffolds, and even localized drug delivery [38]. Fibers from CS can also be prepared into thin mats forming membranes to be used as filtration systems for dye wastewater treatment, and as water softening for pharmaceutical applications [39]. Fibers have been calcined forming short flat fibers known as nanobelts that have different properties, which can be used in applications such as gas sensors

[40-43], anode materials for lithium-ion batteries [44-48], photocatalysts [41, 49], antibacterial agents [50], and supercapacitors [51]. The wide-range success of micro-belts is attributed to their 1-dimensional structure as well as their physical and electronic properties [40, 43].

Additionally, multiple materials have been studied to prepare metal oxide composite fibers from multi-phase precursor solutions that would pair well and complement each other. Wang et al. conducted experiments to evaluate the gas sensing properties of three different metal oxides (tin oxide, zinc oxide, and indium oxide) and compared the results to those reported on three different composite combinations (tin oxide/zinc oxide, tin oxide/indium oxide, and zinc oxide/indium oxide) [52]. The results showed that the tin oxide/zinc oxide and tin oxide/indium oxide composites had a greater sensitivity to ethanol vapor than their counterparts, while the zinc oxide/indium oxide composite had a lower sensitivity. The team attributed these results to how well the composites' catalytic actions react [52].

Recent results reported on the synthesis of SnO_2/TiO_2 micro-belts composite showed that SnO_2 was an excellent material for gas sensing and lithium storage but has poor conductivity [40, 43, 47]. TiO_2 has been a great addition to SnO_2 for its stability due to its robust structure support [47]. Van Duy et al. prepared a 3:7 mol ratio SnO_2/TiO_2 solution by the sol-gel method and was sonicated with carbon nanotubes to achieve uniform thin films. The results showed that the SnO_2/TiO_2 composite had excellent sensitivity at different operating temperatures. The excellent sensitivity was attributed to the SnO_2 reaction with the gas molecules at a temperature around 250 °C while the TiO_2 reacted with the gas molecules at 380 °C[53].

In this work, SnO_2/TiO_2 composite micro-belt calcined short fibers with different Sn:Ti ratios are prepared by centrifugal spinning of precursor solutions and subsequent heat treatment at different ramp-up rates. Their performances are compared using charge/discharge cycling tests

at a constant current density of 100 mA g^{-1}, and the best performing ratio is chosen to carbon coat by CVD method at different deposition times. Different tests are used to compare the batteries' performances using cycle performance, rate performance, cyclic voltammetry (CV), and electrochemical impedance spectroscopy (EIS). The active material's characterization are studied by scanning electron microscope (SEM), thermalgravimetric analysis (TGA), energy dispersive X-ray spectroscopy (EDS), X-ray photoelectron spectroscopy (XPS), and X-ray diffraction spectroscopy (XRD).

CHAPTER II

REVIEW OF LITERATURE

2.1 Inside the Lithium-ion Battery

A typical lithium-ion cell battery is comprised of seven components: a top cap, the anode, a separator, an electrolyte, the cathode, a spacer, a spring, and an end cap shown in figure 1. The anode and the cathode have their respective active material applied as a thin film on current collectors made up of copper foil (anode) and aluminum foil (cathode).

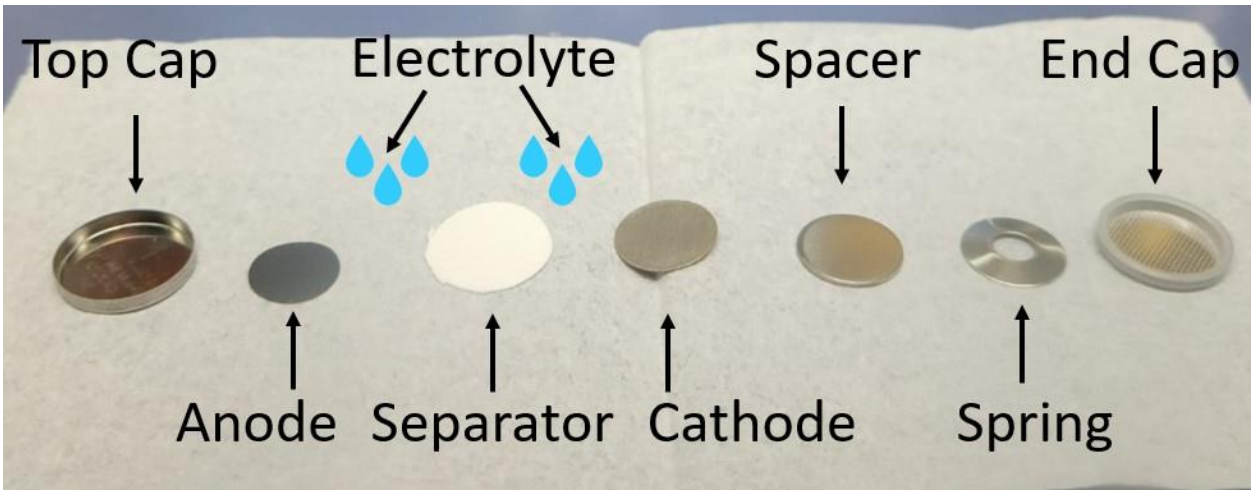

Figure 1: Lithium-ion Cell Battery Schematic.

In a LIB, the cathode typically consists of lithium cobalt oxide, lithium manganese oxide, or lithium iron phosphate. In a half-cell battery where the anode is being studied, the cathode is a lithium chip. Alternatively, the anode consists of graphite.

2.1.1 The Separator

The separator plays a vital role in ensuring safe and efficient operation in LIBs. The primary function of the separator is to allow lithium-ions to flow between the two electrodes while acting as a barrier to prevent the electrodes from coming into contact, which can cause the battery to short circuit [6]. The most common materials used for separators are polyethylene (PE) and polypropylene (PP) membranes, but other materials, such as glass microfibers, have been studied. Research into separators is low compared to the research into the electrodes of a battery. Still, many scientists recently have begun to research the different properties of separators and publish the contributions that separators have on LIBs. To be effective in LIBs, a separator must possess specific traits. These include adequate wettability, mechanical and thermal stability, and consistent thickness uniformity [54].

A separator should have adequate wettability so that the electrolyte can be absorbed fast and easily, so the electrolyte filling time is short. The filling time is crucial to LIBs as it dramatically affects battery performance and life cycle. Filling refers to the electrolyte filling the separator's and the electrodes' pores. If the pores are poorly wetted it can, cause the electrodes to develop non-uniform solid electrolyte interphases (SEI) [55]. Additionally, it can lead to dendrite formation, which significantly reduces the performance of the battery and cause safety issues. It can also lead to the decomposition of the electrolyte during cycling which can increase ionic resistance. Although there is no scientific test to determine wettability, a simple test is to drop a single drop of electrolyte onto the separator and visually inspect if the separator absorbs the drop fast and uniformly [54].

The mechanical stability of a separator is essential in both the assembly and electrochemical processes [6]. During the assembly process, the separator needs to withstand the

handling done to separate the two electrodes as well as to withstand the crimping pressures when closing the battery. Research shows that the minimum requirement for the mechanical strength of a 25 μm thick separator is 1000 kg/mm^2 [54]. During the electrochemical process, the separator's mechanical stability should withstand the cell abuse done during cycling preventing a short circuit between the two electrodes. Aside from mechanical stability, overtime the cell abuse causes cell temperature to rise and risks a thermal runaway to happen. This is where the separator's thermal stability ensures the safety of the battery. If the temperature rises in the battery, the separator is made to soften during these high temperatures causing the pores to close and preventing Li-ions from flowing essentially causing a shutdown of the battery where current ceases to flow. If either the mechanical properties, the thermal properties, or both fail then the electrodes will make contact causing a short circuit that triggers a thermal runaway [56].

On the other hand, the thickness of the separator affects all the previous traits. If the thickness is too thick, then the wettability of the separator will be too low causing resistance in the electrolyte. If the thickness is too thin, then the properties will be affected causing a short circuit between the electrodes leading to a thermal runaway. Additionally, any variance in the uniformity of the thickness can cause performance and safety issues. The thickness of a separator in a battery is based on the desired output of the battery. Typically, higher capacity batteries require thin separators as they offer lower resistance helping to increase battery capacity. Arora et al reported higher capacity cells generally used 16 to 20 μm thick separators compared to 25 μm used by lower capacity cells. It was also reported that increasing the thickness caused the discharge capacity to decrease from 95 to 90 % and a further decrease to 75 % upon further thickness increase [54].

2.1.2 The Solid Electrolyte Interphase (SEI)

The SEI is a layer that forms on the surface of the anode during the initial cycle and plays a crucial role in battery performance and safety. As the battery goes through its cycle, the anode and cathode components undergo Li-ion intercalation and deintercalation, which allows lithium ions to flow between the electrodes. Nonetheless, these ions can also interact with the electrolyte and create a thin layer known as “solid electrolyte interphase” (SEI) on the anode’s surface. This layer can be seen in cyclic performance testing during the first irreversible discharge/charge cycle where Li-ions are consumed causing the capacity to decrease between the initial discharge and charge [57]. Despite this, the SEI is necessary for LIBs since it largely influences their performance and safety. The SEI layer consists of different components such as lithium carbonates (Li_2CO_3), lithium fluoride (LiF), lithium oxide (Li_2O), and organic material such as dilithium ethylene glycol dicarbonate (Li_2EDC) [58]. By acting as a protective shield, the SEI layer prevents further electrolyte degradation that may cause the battery to malfunction [59].

Moreover, the SEI layer controls the lithium-ion flow between the anode and electrolyte and curbs the growth of dendrites that can trigger short circuits and thermal runaway [60]. The SEI formation mechanism is complex and not fully understood. It is known that the SEI layer forms due to the reaction of Li-ions with the electrolyte components and the anode surface [57-59]. The SEI formation process involves several steps, including electrolyte reduction, decomposition, and reactivity with the anode surface. Its formation is affected by several factors, including the current density, voltage, temperature, and composition of the electrolyte [60]. Additionally, its properties may differ according to the cycling conditions and electrolyte constitution. Examples of this are researchers have found different SEI layers to be single, double, multilayer, porous, and sandwich structures as well as be brittle or elastic [57]. Several

electrochemical, spectroscopic, and microscopic techniques are employed to analyze the SEI layer's characteristics such as thickness, resistance, and capacitance. Spectroscopic techniques, such as X-ray photoelectron spectroscopy and Fourier-transform infrared spectroscopy, are used to analyze the SEI layer's chemical composition and bonding [60].

The battery's performance can be influenced by properties of the SEI layer. A uniform and thick SEI layer is helpful in avoiding dendrite formation and enhancing battery cycling stability. However, battery capacity and rate capability may suffer since a thick SEI layer causes more resistance to Li-ion diffusion. Conversely, a thin SEI layer can lead to better capacity and rate capability but may reduce cycling stability due to the anode surface being more reactive [58].

Apart from enhancing battery performance, the SEI layer also plays a crucial role in ensuring battery safety. The properties of the SEI layer may impact thermal stability and the possibility of thermal runaway. Thus, a uniform and thick SEI layer minimizes chances of the anode reacting with the electrolyte that can elevate the chances of a thermal runaway. In contrast, the anode may react with the electrolyte when the SEI layer is unstable or too thin, resulting in thermal runaway [6].

2.2 The Anode

The anode is an important element of the LIB that has a tremendous effect on the performance of the battery. The importance of the anode is in its ability to store and release Li-ions. During discharge an external load transfers the electrons from the anode to the cathode causing the Li-ions to be discharged into the electrolyte, transferred through the separator, and ultimately be absorbed by the cathode. Alternatively, a charger will flip the process and transfer

the electrons from the cathode to the anode and cause the Li-ions to flow back into the electrolyte through the separator and be absorbed by the anode [61].

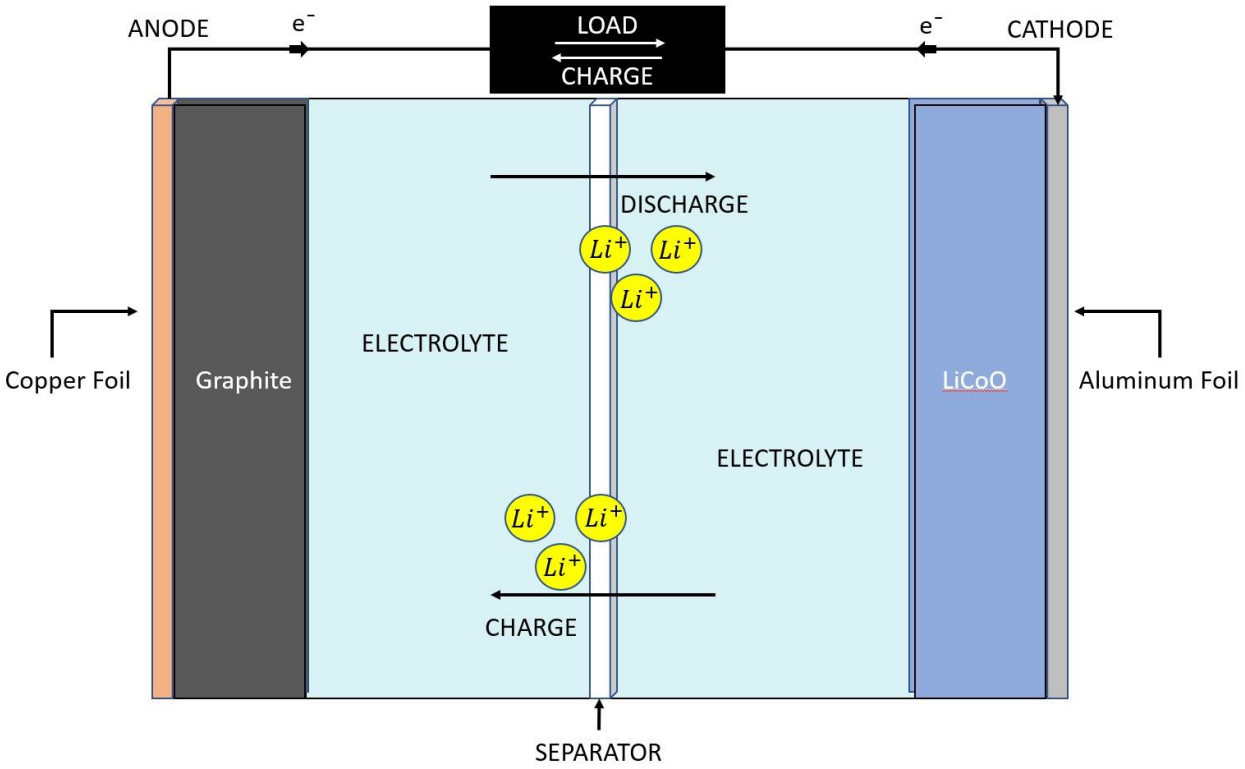

Figure 2: Charge/discharge schematic of a lithium-ion battery.

The performance of the battery depends on the material used for the anode and its intercalation capabilities with Li-ions [62]. Intercalation is the process where Li-ions are inserted into the active material's structure. Typically, commercial anodes are made with graphite which has a theoretical capacity of 372 mAh g^{-1} and is made up of carbon layers shaped in hexagonal rings. It takes 6 carbon atoms to intercalate one Li-ion as shown in figure 3 [22, 63, 64]. Alternatively, silicon has a high theoretical capacity of 4200 mAh g^{-1} and can intercalate ~4.4 Li-ions with only 1 Si atom [9, 12, 15, 61]. This is a disadvantage for graphite since it needs 4 times the material to intercalate the same amount of Li-ions as silicon making batteries bigger and heavier, which is a drawback. This disparity affects the volumetric capacity of graphite (~800

mAh cm^{-3}) [63] which is an important factor when it comes to minimizing space and weight. Comparatively, silicon's volumetric capacity is 2200 mAh cm^{-3} which is almost 3 times more than graphite [65].

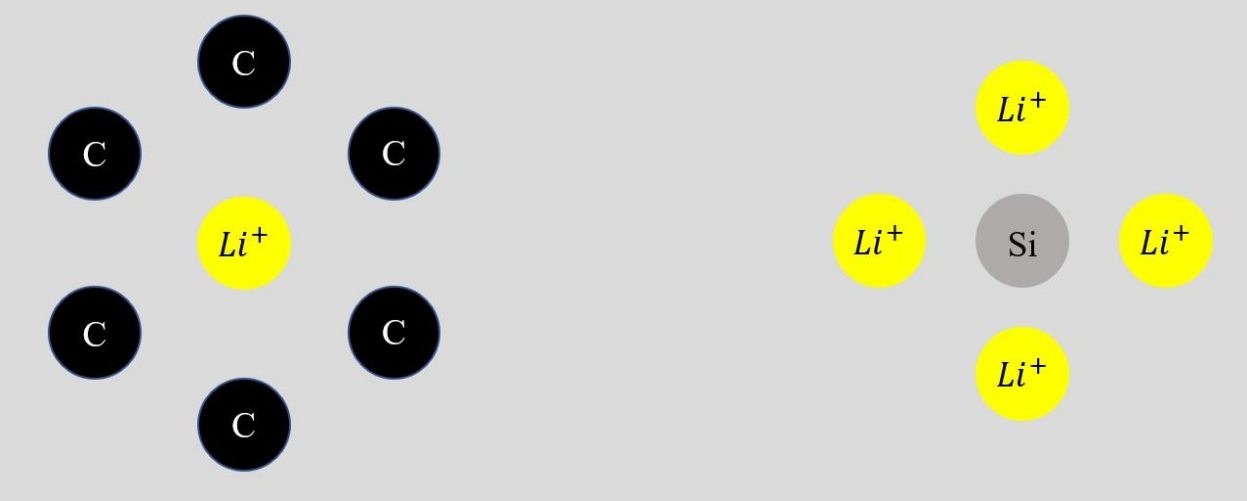

Figure 3: Intercalation diagram of graphite and silicon.

2.2.1 Metal Oxide Anodes

Metal oxides as anode materials have been a point of interest to many researchers for their non-toxicity, high theoretical capacities, abundance in nature, and relatively low cost of fabrication [19, 61, 66-70]. Unfortunately, metal oxides also have drawbacks with rapid capacity decrease, poor rate performance, and poor cycle stability [61]. Researchers have been studying different active material structures and particle sizes to counteract these drawbacks.

2.2.2 Tin Oxide Anodes

A metal oxide that has been of great research interest is tin oxide (SnO_2). Tin oxide has a high theoretical capacity of ~790 mAh g^{-1} [18, 19] comparable to its metal counterpart of tin (Sn) with a capacity of 994 mAh g^{-1}. SnO_2 can achieve a high theoretical capacity due to the

irreversible reduction process from SnO_2 to Sn. However, this process causes a loss of capacity from the first charge/discharge cycle. After the first irreversible cycle, Sn undergoes a reversible process of alloying/dealloying with Li resulting in ~4.4 units of Li being stored into one unit of Sn. Consequently, this large number of intercalating Li-ions cause a large volume change of ~200% in the anode resulting in the pulverization of the electrode and fast capacity fade upon further cycling [18, 19].To improve the electrochemical performance of SnO_2, researchers have been experimenting on the morphology of the active material such as creating SnO_2 nanowires, nanosheets, and hollow nanospheres [9].

2.2.3 Titanium Oxide Anodes

Another metal oxide that has been researched extensively is titanium oxide (TiO_2). TiO_2 is popular not only among Li-ion batteries but in other fields used for gas sensing and antibacterial applications because of the material's remarkable chemical, electronic, and optical properties [50]. As for its performance as anodes for Li-ion batteries, TiO_2 has a low theoretical capacity of ~330 mAh g^{-1} making it lower than graphite (372 mAh g^{-1}) [68, 71]. Nevertheless, TiO_2 has shown to have good cyclability with a steady capacity fade compared to other metal oxides that have steep capacity losses [68]. Research has shown that the electrochemical performance of TiO_2 can be improved by combining the material with other metal oxides [41, 49, 66, 67, 72, 73], changing the morphology of the material [42, 47, 66, 70, 74], or incorporating carbon into its structure [47, 66, 67].

CHAPTER III

METHODOLOGY AND FINDINGS

3.1 State of the Art Equipment

The experiments conducted in this work to synthesize, heat treat, and characterize the active material as well as to assemble and test the batteries were done with the help of the following state of the art equipment and software.

The cyclone machine in figure 4 was used to spin precursor metal oxide solutions into micro-fibers using centrifugal forces. A spinneret with two needles expels the solution at an adjustable rotational speed and time. Parameters such as humidity and temperature need to be taken into consideration before spinning.

Figure 4: Image of cyclone machine.

The vacuum oven in figure 5 is used to dry and store the collected micro-fiber mats. This is a crucial step in synthesizing the active material because it eliminates any remaining solvents from the fibers while preventing any additional moisture from being absorbed.

Figure 5: Image of vacuum oven.

The tube furnace (MTI Corporation, OTF-1200X) in figure 6 is used to oxidize the micro-fibers in air as well as to pyrolyze the copper foil in an argon atmosphere. An argon gas tank is connected to a regulator and flowmeter to control the flow of argon through the furnace.

Figure 6: Image of tube furnace.

The SEM machine (Zeiss Sigma VP) in figure 7 is used to characterize the structure and morphology of the precursor fibers as well as the calcined and carbon-coated material. The SEM machine is equipped with an EDS (EDAX Octane Super) instrument that is used to determine the elemental composition of the materials.

Figure 7: Image of Scanning Electron Microscope (SEM) machine and Energy Dispersive X-ray Spectroscopy (EDS).

Figure 8 shows the TGA (Netzsch, TG 209 F3 Tarsus) instrument used to show the thermal decomposition of the fibers to determine the amount of active material in them. The analysis can be performed in air or in a nitrogen atmosphere.

Figure 8: Image Thermogravimetric Analysis (TGA) instrument.

Figure 9 shows the XPS (ThermoScientific K-Alpha) machine that is used to characterize the material's crystal structure/crystallization phase and surface chemistry. XPS and XRD are used together to further analyze the active material.

Figure 9: Image of X-ray Photoelectron Spectroscopy (XPS) machine.

The XRD (Bruker D2 Phaser) machine in figure 10 is used to determine the active material's crystal structure and chemical bond. XRD and XPS are used together to further analyze the active material.

Figure 10: Image of X-ray Diffraction (XRD) machine.

The rapid mixer and grinder (Hauschild SpeedMixer, DAC 150.1 FVZ-K) in figure 11 is used with 2 mm Zirconia ceramic beads to grind the active material down to a fine powder.

Figure 11: Image of rapid mixer and grinder.

In figure 12, the argon gas-filled glovebox (MBRAUN) is used to safely assemble the Li-ion cell batteries with parameters of H_2O and O_2 below 0.5 parts per million (ppm).

Figure 12: Image of glovebox workstation.

The LANHE battery testing system in figure 13 is used to test the charge/discharge performance, the cycle stability, and Coulombic efficiency of the Li-ion batteries. The electrochemical performances of the batteries are studied under a constant current density with the LAND software.

Figure 13: Image of LANHE battery testing system.

The Arbin battery testing system in figure 14 is used to test the rate performance of the batteries. The electrochemical performances of the batteries are analyzed at different current densities between 50 and 500 mA g^{-1} with the MITS Pro software.

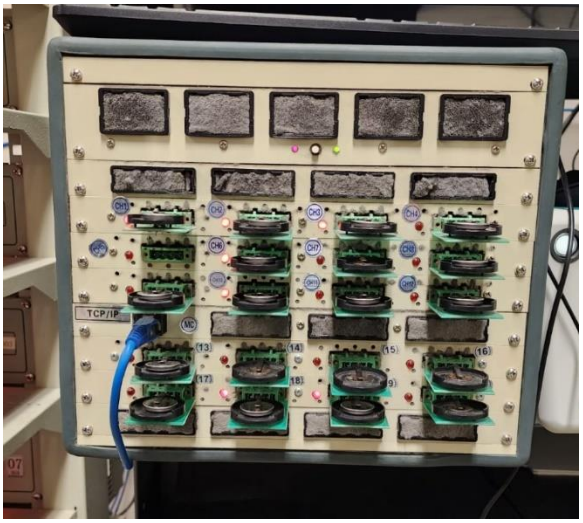

Figure 14: Image of Arbin battery testing system.

The Autolab battery testing system in figure 15 is used to test the impedance of the batteries using an Electrochemical Impedance Spectroscopy (EIS). Both the real and imaginary numbers of the impedance are graphed to show the resistance of the batteries over a frequency range of 0.1 and 1000 Hz using NOVA software.

Figure 15: Image of Autolab battery testing system.

In figure 16, the BioLogic battery testing system is used to analyze the redox reaction in the batteries. The experiment is done with a scan rate of 0.1 mV s^{-1} using the BT-Lab software.

Figure 16: Image of BioLogic battery testing system.

3.2 Preparation of Active Material

For the preparation of the composite active material, polyacrylonitrile (PAN) (*Mw* 150,000), polyvinylpyrrolidone (PVP) (*Mw* ~1,300,000), Super P carbon black, ethylene carbonate (EC), dimethyl carbonate (DMC), tin (II) 2-ethylhexanoate, and titanium (IV) butoxide (reagent grade, 97%) were purchased from Sigma Aldrich and used as received. N, N-dimethyl formamide (DMF), and absolute ethanol (200 proof) were purchased from Fisher Chemical and were used as received. Whatman glass microfibers were used as separators in li-ion battery half-cells and were purchased from GE Healthcare. Commercial lithium metal and lithium salt ($LiPF_6$) were purchased from MTI, USA.

3.2.1 Composite Micro-Fiber Preparation

Micro-fibers were spun by making 20-gram solutions of ethanol and PVP with weight concentrations of 85% and 15%, respectively. SnO_2 and TiO_2 precursors were mixed with 50

wt.% PVP to prepare solutions with SnO_2 and TiO_2, as well as 4 different SnO_2 to TiO_2 ratios: 1:1, 2:1, 3:1, and 3:2. The solutions were magnetically stirred for 24 hrs and then centrifugally spun using a spinneret equipped with 30-gauge needles. Rotational speeds of 9000 rpm were used at 2 min intervals until the 20-gram solutions were completely spun. The fibrous mats were collected as shown in figure 17 and dried at room temperature for 24 hrs in a vacuum oven.

Figure 17: Images of fibers and collected mat.

The mats were then placed in an oven to be calcined at 700 °C for 3 hrs. Different ramp-up rates between 0.5 to 3.3 °C/min were used during the calcination process of the SnO_2/TiO_2 fibers to modify the structure of the short fibers into flat micro-belts as shown in figure 18.

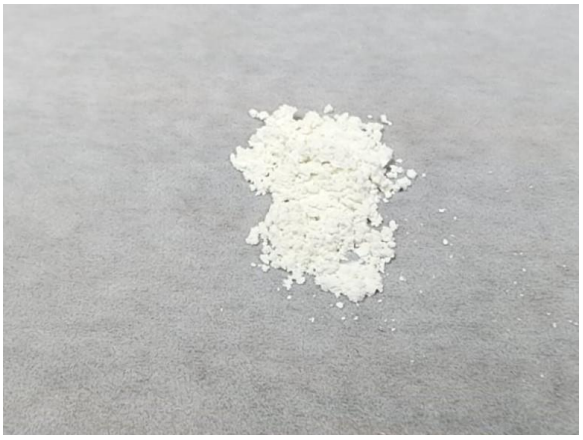

Figure 18: SnO_2/TiO_2 material.

After calcination, the SnO_2/TiO_2 micro-belts with different ratios were mixed into an active material/PAN/carbon black slurry with a ratio of 8:1:1, using DMF as a solvent, and prepared for use as anode material in lithium-ion batteries. The slurry mixture was applied as a thin film (10 μm) onto a copper foil as shown in figure 19 and set to dry in vacuum for 24 hrs. The copper foil was then placed in a tube furnace (MTI Corporation, OTF-1200X) at a temperature of 450 °C for 5 hr under argon atmosphere. The copper foil was then cut into ½" diameter anodes and assembled into a Li-ion half-cell. The assembled batteries were evaluated using the LAND Battery Testing Monitor system software with a charge/discharge voltage of 3V and 0.05V, respectively.

Figure 19: SnO_2/TiO_2 slurry on copper oil

3.2.2 Preparation of Carbon-Coating

The process of carbon-coating the SnO_2/TiO_2 material started by placing the material in a quartz boat in a tube furnace. The material was heated to 1000 °C at a rate of 33 °C/min with 160 standard cubic centimeters per min (SCCM) of argon flowing in the chamber. Once the furnace reached 1000 °C, 32 SCCM of methane (CH4) gas filled the furnace so that the synthesis of carbon can take place. Different deposition times were done to test the effects of CVD on the electrochemical performance of SnO_2/TiO_2: 30 mins and 60 mins. After the coating times were done, the furnace ramped down to room temperature and the material was collected. The white material turned black after the heat treatment as shown in figure 20 and some of the material fused together to form small circular objects. The resulting material was harder than the previous material and manual grinding was not possible. A Hauschild Speed Mixer (DAC 150.1 FVZ-K) was used at a speed of 2300 rpm for 5 min with 2 mm Zirconia ceramic beads to grind the material down to a fine powder. Afterwards, the carbon-coated material was used to make a

slurry on copper foil with the same method as the non-carbon coated material. Anodes were cut out to make half-cell batteries and the electrochemical performances were compared to the non-carbon coated material.

Figure 20: Carbon-coated SnO_2/TiO_2.

3.3 Half-Cell Assembly

The ½" diameter anodes were placed in an argon gas-filled glovebox (MBRAUN) with H_2O and O_2 levels <0.5 ppm. Anodes were placed on the top cap of the cell battery, followed by electrolyte, separator, lithium metal (cathode), spacer, spring, and bottom cap. The electrolyte was made from 1M of $LiPF_6$ in EC/DMC (1:1 v/v). A hydraulic crimping machine was used to close the cell battery with 1000 psi. The assembled batteries were taken out of the glovebox to perform electrochemical testing including cycle performance, rate performance, electrochemical impedance spectroscopy (EIS), and cyclic voltammetry (CV).

3.4 Structure Characterization of Non-Coated Active Material

The structure and morphology of the SnO_2/TiO_2 fibers were characterized by scanning electron microscope (SEM) (Zeiss Sigma VP), energy dispersive X-ray spectroscopy (EDS) (EDAX Octane Super), thermogravimetric analysis (TGA) (Netzsch TG 209 F3 Tarsus), X-ray photoelectron spectroscopy (XPS) (ThermoScientific K-Alpha), X-ray diffraction spectroscopy (XRD) (Bruker D2 Phaser) and Raman spectroscopy. The pre-calcined fibers were sprayed with gold particles using gold sputtering to collect clearer images from SEM and EDS. The diameters of 100 pre-calcined fibers from each ratio were measured and collected to compare while 100 measurements of length, thickness, and width of calcined short fibers were collected to compare. The fibers were placed in the TGA and heated to 700 °C at a rate of 5 °C/min to examine the thermal degradation of the fibers.

The morphology and structure of the SnO_2/TiO_2/PVP precursor fibers were analyzed by SEM at 500x magnification. Figure 21 (a-h) shows the SEM images and the corresponding size distribution histograms of the SnO_2/TiO_2/PVP precursor fibers. The images show long thin fiber morphology with the highest diameter distribution between 3.5 to 3.8 μm. There does not seem to be a clear correlation between the ratio of the material and the size of the diameter. The results, in order of increasing SnO_2 quantity, are 3.834, 3.524, 3.7, and 3.612 μm.

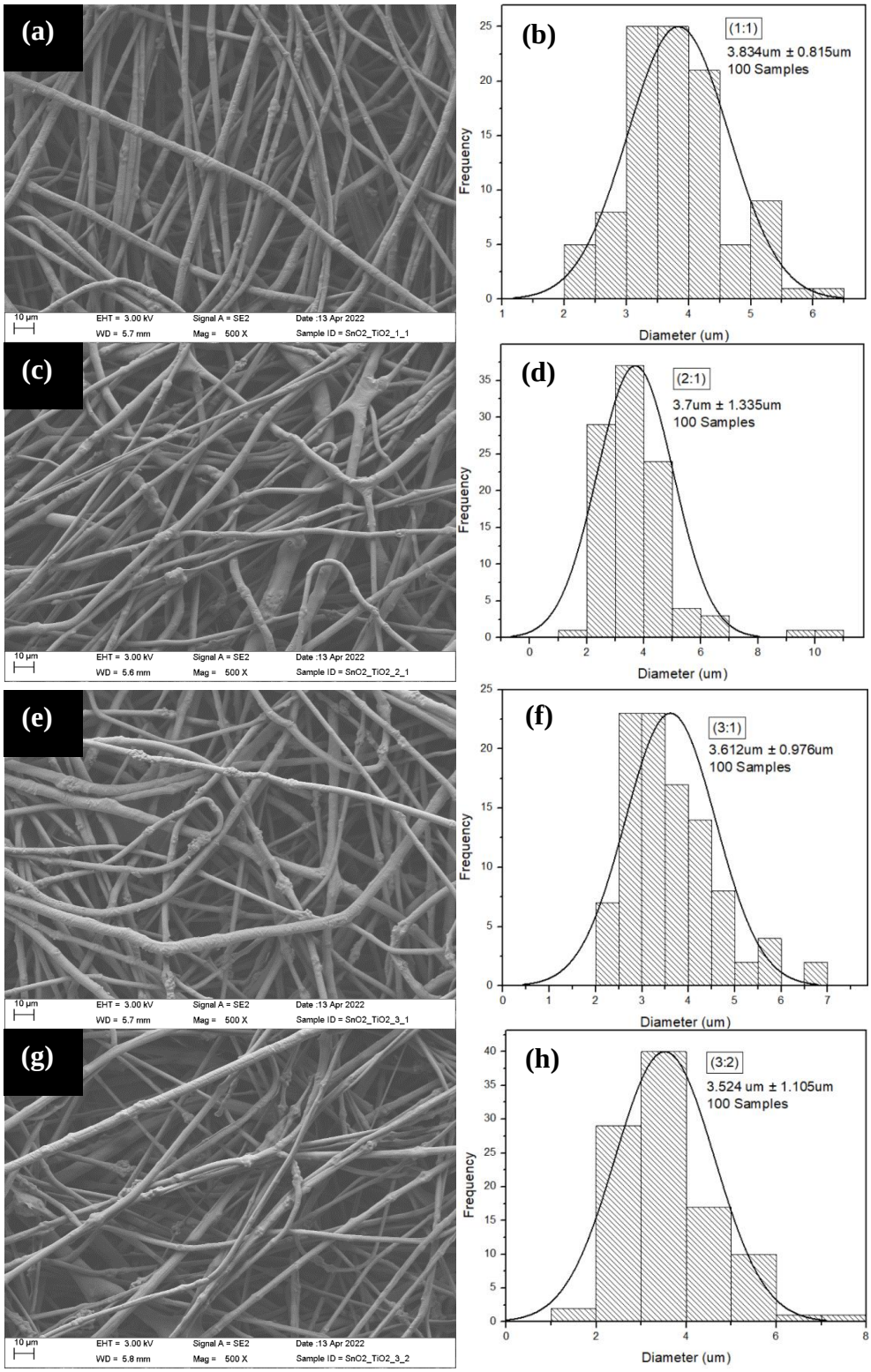

Figure 21: SEM images and histograms of SnO_2/TiO_2/PVP fibers at different ratios: (a-b) 1:1, (c-d) 2:1, (e-f) 3:1, and (g-h) 3:2.

EDS was used to determine the composition of SnO_2/TiO_2 in the composite fibers at 500x magnification. The EDS mappings (figure 22) show that the SnO_2/TiO_2/PVP (1:1) composite fibers are composed of distributed carbon (C), nitrogen (N), oxygen (O), tin, and titanium. The EDS mappings of the other ratios are shown in figures 52-54 in the appendix.

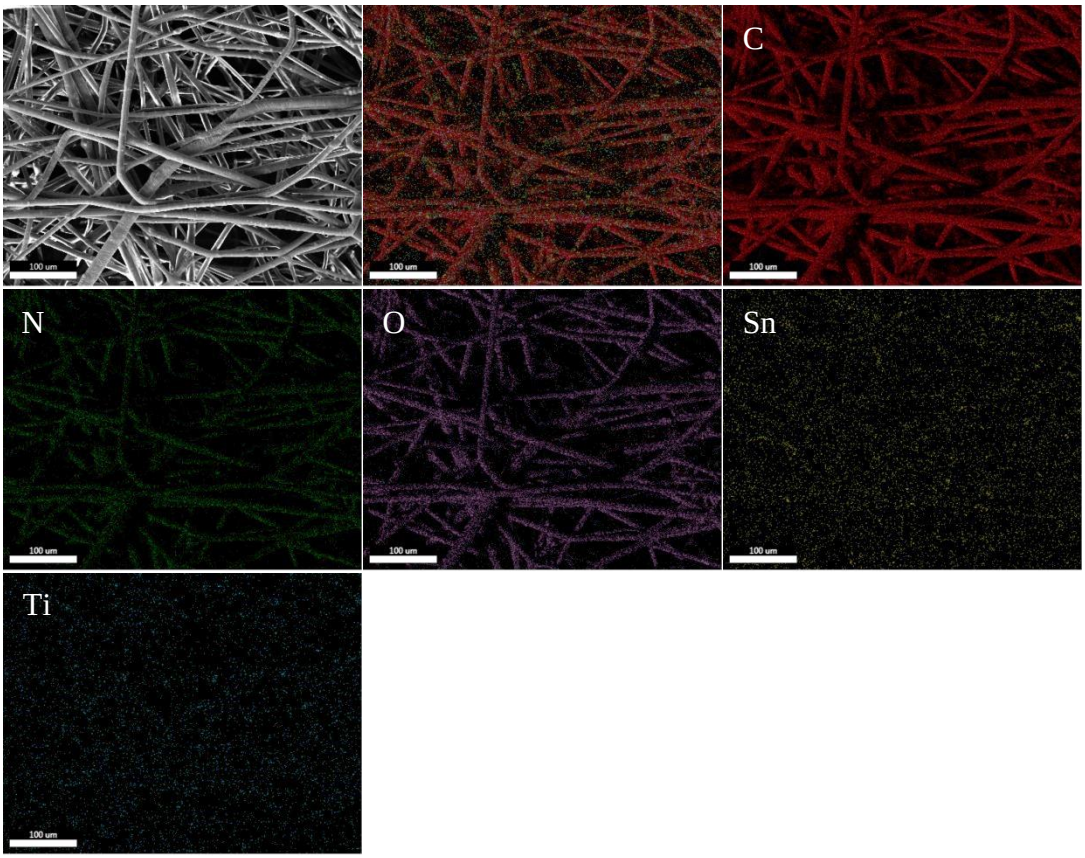

Figure 22: EDS mappings of SnO_2/TiO_2/PVP fibers (1:1).

Additionally, table 1 shows the EDS mapping results of the 1:1 pre-calcined fibers. According to the results, the 1:1 (50 %:50 %) fibers show a ratio of 45.8 %:54.2 %. The other ratios are listed in tables 16-18 of the appendix. The results for the other ratios are 62.9 %:37.1 % for the 2:1 (66 %:33 %) fibers, 65.3 %:34.7 % for the 3:1 (75 %:25 %) fibers, and 54.7 %:45.3 % for the 3:2 (60 %:40 %) fibers. These results show the solutions mixed with the different ratios were spun into pristine fibers with ratios close to the intended mixtures.

Table 1: EDS mapping results of SnO_2/TiO_2 (1:1) pre-calcined fibers.

Element	Weight %	Atomic %	Net Int.	Error %	K ratio	Z	A	F
C K	59.82	86.74	607.92	5.49	0.5246	1.1714	0.7487	1.0000
O K	7.50	8.16	48.31	22.08	0.0279	1.1091	0.3355	1.0000
AuM	15.47	1.37	69.85	12.00	0.1044	0.5740	1.1707	1.0045
SnL	11.66	1.71	24.52	27.47	0.0771	0.6430	1.0269	1.0011
TiK	5.56	2.02	13.45	30.69	0.0449	0.8254	0.9836	0.9954

Figure 23 shows the SEM images of the calcined SnO_2/TiO_2 fibers with 1:1 (a-c); 2:1 (d-e), 3:1 (g-i) and 3:2 (j-l), at 2000x magnification. The SnO_2/TiO_2/PVP precursor composite fibers were calcined in a tube furnace using different heating (ramp-up) rates to determine the effect of the heating rate on the micro-belts formation. The rates used for the SnO_2/TiO_2 fibers with (1:1) ratio (figure 23 (a-c)) ranged from 1.0 to 3.3 °C/min. The SEM image in figure 23 (b) shows that the SnO_2/TiO_2 micro-belts were formed after the heat treatment at a rate of 3.0 °C/min. The SnO_2/TiO_2 prepared at a rate of 1 °C/min (figure 23 (a)) showed some micro-belts formation but mostly had random oxidized short fibers. It is worthwhile to note even a low-rate change of 0.3 °C/min (i.e., @ 3.3 °C/min) above the previous rate to form micro-belts, the ramp-up rate caused the fibers to have a completely different morphology (figure 23 (f)). The thermal treatment of the precursor fibers using a ramp-up rate of 3.3 °C/min (figure 23 (c)) resulted in the formation of short fibers with an abundance of nodules with no definitive shape.

The SEM images of SnO_2/TiO_2 fibers with 2:1 ratio (figure 23 (d-f)), prepared at a ramp rate of 1.1 °C/min (figure 23(d)) showed the formation of flat fibers with many nodules. The fibers became wider and flatter at a rate of 1.3 °C/min (figure 23 (e)) with fewer nodules than that at 1.1 °C/min. At 1.5 °C/min (figure 23(f)), the SEM images showed the formation of micro-belts.

The SEM images of SnO_2/TiO_2 fibers with 3:1 ratio (figure 23 (g-i)), prepared at a ramp rate of 0.5 °C/min (figure 23(g)) showed short fibers with nodules with no definitive shape. The fibers showed no visual difference at a higher rate of 0.6 °C/min (figure 23 (h)) than that at 1.1 °C/min. At 1.0 °C/min (figure 23(i)), the SEM images showed the formation of micro-belts with the indications of the short fibers becoming smooth.

The SEM images of SnO_2/TiO_2 fibers with 3:2 ratio (figure 23 (j-l)) showed micro-belts at a rate of 2.0 °C/min (figure 23 (k)). Figure 23 (j) showed that flat belts started to form at a rate of 1.5 °C/min, while the 2.5 °C/min rate (figure 23 (k)) showed a few micro-belts starting to blend to form bigger nodules.

The SEM images in figure 23 showed a pattern for micro-belts formations: the higher the ratio of SnO_2 in the fibers, the slower the ramp-up rate used during the thermal treatment of the SnO_2/TiO_2 precursor fibers. The minimum (or lowest) SnO_2 concentration in the precursor fibers was 50 wt. % for the 1:1 ratio while the required heating rate for the micro-belts formation was 3 °C/min. The maximum (or highest) SnO_2 concentration in the precursor fibers was 75 wt. % for the 3:1 ratio while the required heating rate for the micro-belts formation was 1.0 °C/min. At SnO_2 concentrations of 60 (3:2) and 66 (2:1) wt. %, the heating rates required to form micro-belts were 2.0 and 1.5 °C/min, respectively. Alternatively, the pattern can also be described in terms of the TiO_2 concentration in the precursor fibers: the higher the concentration of TiO_2 (25 %, 33 %, 40 %, and 50 %), the faster the ramp-up rate needs to be (1.0 °C/min, 1.5 °C/min, 2 °C/min and 3 °C/min).

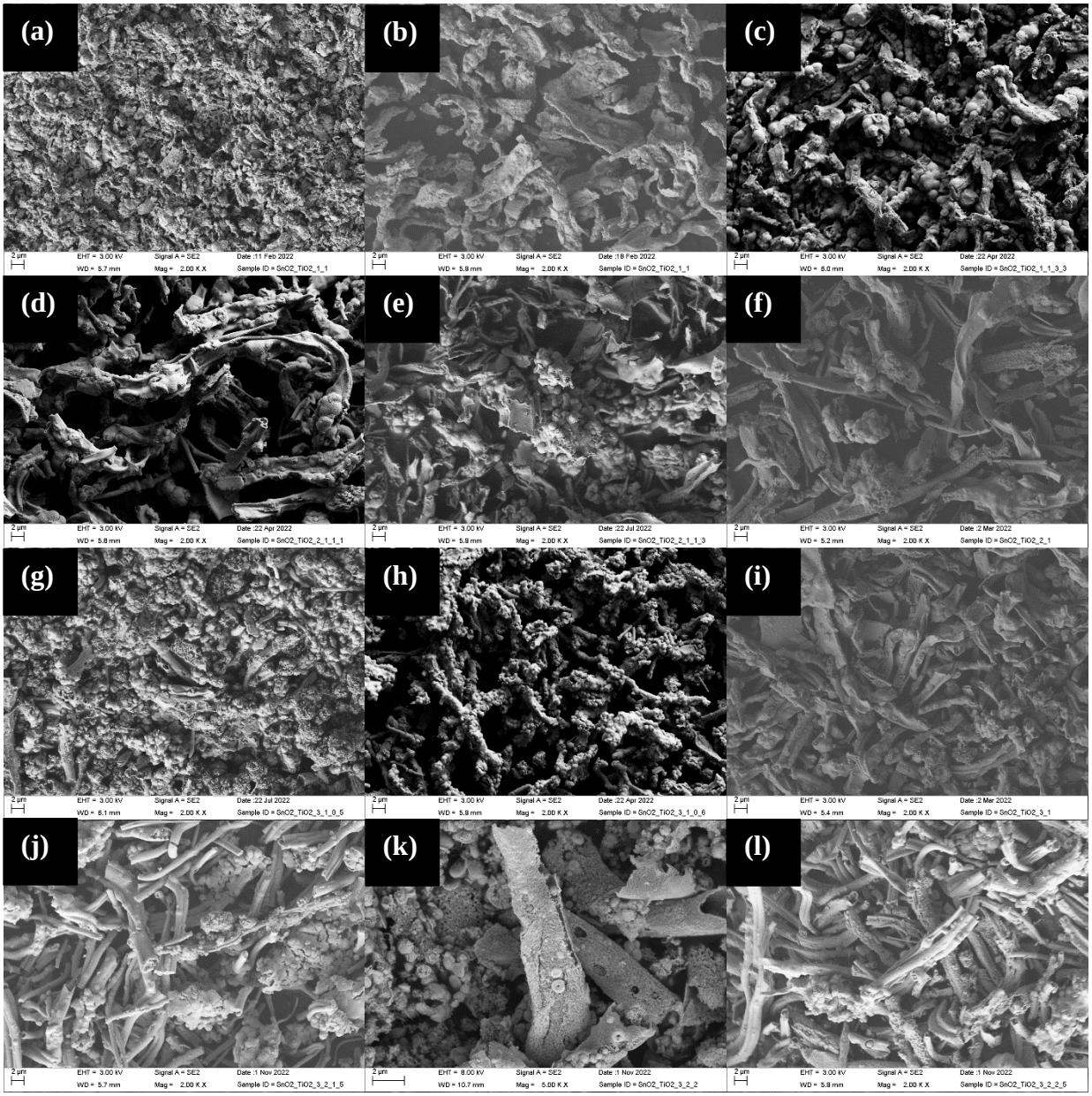

Figure 23: SEM images of calcined SnO_2/TiO_2 fibers: 1:1 fibers at rates of (a) 1.0, (b) 3.0, and (c) 3.3 °C/min, 2:1 fibers at rates of (d) 1.1, (e) 1.3,and (f) 1.5 °C/min, 3:1 fibers at rates of (g) 0.5, (h) 0.6, and (i) 1.0 °C/min, and 3:2 fibers at rates of (j) 1.5, (k) 2.0, and (l) 2.5 °C/min.

Figure 24 (a-l) shows the histograms of length, thickness, and width of the calcined fibers for all the different ratios. The lengths (figures 24 (a), 24 (d), 24 (g), 24 (j)) for the different ratios have a range between 5.743 and 6.753 μm with the 3:2 ratio being the shortest and the 2:1

ratio being the longest. The thicknesses (figures 24 (b), 24 (e), 24 (h), 24 (k)) have a range between 0.52 and 0.685 μm with the 1:1 ratio being the thinnest and the 3:2 being the thickest. The widths (figures 24 (c), 24 (f), 24 (i), 24 (l)) have a range between 2.048 and 2.384 μm with the 3:1 ratio being the thinnest and the 2:1 ratio being the widest. The results show no pattern of one ratio being the longest, thickest, or widest between the different ratios. This concludes that the different ratios can have different sizes depending on the location chosen for measurements, but the measurements are close enough to each other that there are no significant differences between each ratio.

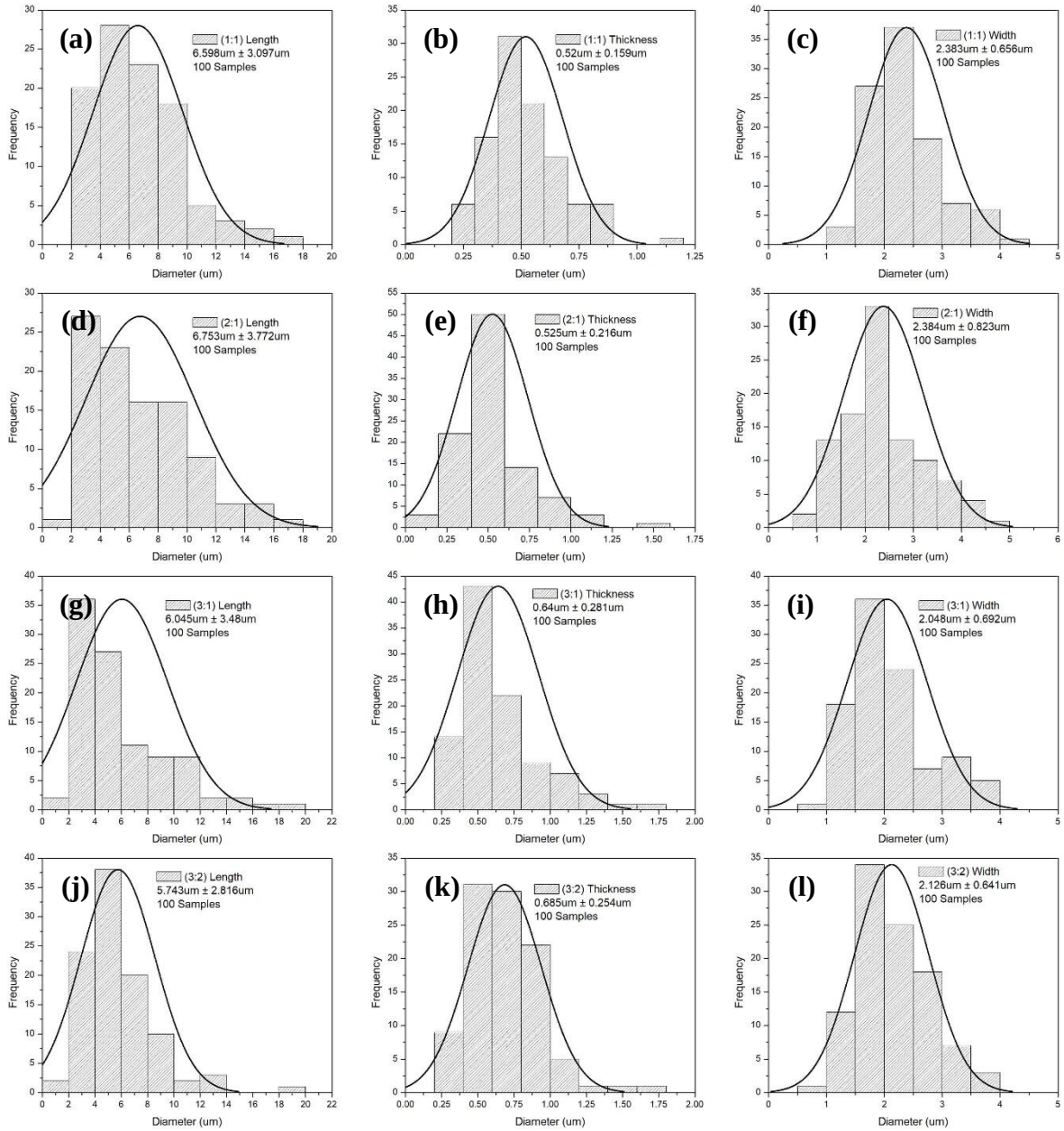

Figure 24: Length, thickness, and width histograms of SnO_2/TiO_2 calcined fibers: (a-c) 1:1, (d-f) 2:1, (g-i) 3:1, and (j-l) 3:2.

Figure 25 shows the EDS mapping of the SnO_2/TiO_2 (3:2) micro-belt. After heat treating at a rate of 2.0 °C/min, the precursor fibers have carbon (C), nitrogen (N), oxygen (O), tin (Sn), and titanium (Ti). The EDS mappings of the other calcined ratios are shown in figure 55-57 in the appendix.

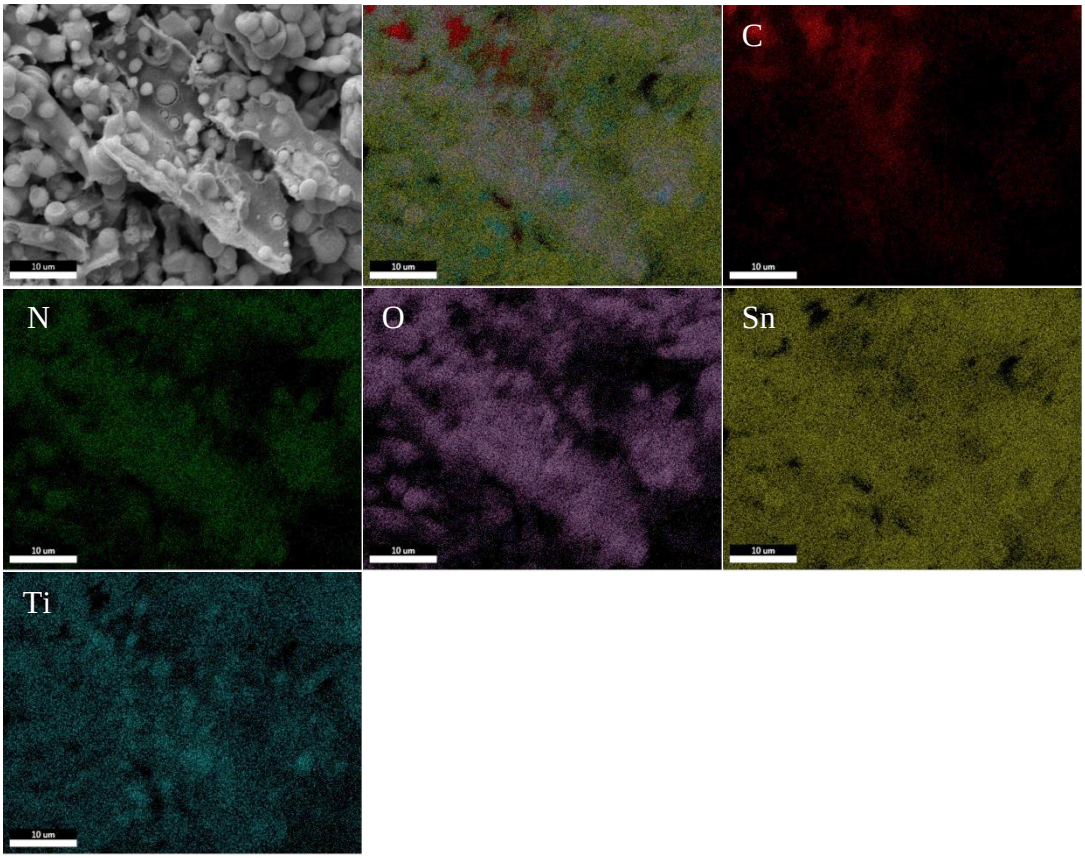

Figure 25: EDS mapping of calcined micro-belt SnO_2/TiO_2 (3:2) at 2.0 °C/min.

Additionally, table 2 shows the EDS mapping results of the 3:2 calcined fibers. The results show the 3:2 fibers have a 61.3 %:38.7 % ratio. The tables for the rest of the ratios are in tables 19-21 in the appendix. The results for the other ratios are 47.3 %:52.7 % for the 1:1 calcined fibers, 70.7 %:29.3 % for the 2:1 fibers, 78.2 %:21.8 % for the 3:1 fibers. These results follow closely to the pre-calcined fibers of the ratios matching closely to the intended mixtures.

Table 2: EDS mapping results of SnO_2/TiO_2 (3:2) calcined fibers.

Element	Weight %	Atomic %	Net Int.	Error %	K ratio	Z	A	F
C K	3.40	13.52	92.60	5.21	0.0358	1.4873	0.7068	1.0000
N K	2.28	7.75	48.20	5.94	0.0231	1.4483	0.7017	1.0000
O K	11.98	35.71	261.60	8.21	0.0663	1.4144	0.3916	1.0000
SnL	65.63	26.38	483.40	3.31	0.5750	0.8570	1.0198	1.0024
TiK	16.71	16.64	147.70	5.00	0.1691	1.0967	0.9196	1.0036

Figure 26 shows the thermal degradation of the SnO_2/TiO_2/PVP precursor fibers and calcined SnO_2/TiO_2 composite fibers using TGA in air from 27 to 700 °C at a rate of 5 °C/min. The results showed that the temperature at which the fibers are stripped of their polymer and solvent, leaving only the active material.

The degradation mechanism of the precursor fibers with different SnO_2 to TiO_2 ratios showed a similar trend. At temperatures between 21 and 200 °C, the weight percentage decreases with increasing temperature which was due to the evaporation of the remaining solvent. Ethanol at this temperature completely evaporates, leaving about 85 % of the PVP fibers with the active material. At a temperature between 250 and 525 °C, the weight percentage of the precursor fibers drastically drops from 80 % to 14 % due to the decomposition of the polymer. At temperatures above 525 °C, the TGA results showed that the content of SnO_2 and TiO_2 in the precursor fibers were 13.6, 14.8, 14.7, and 13.7 % for the 1:1, 2:1, 3:1, and 3:2 ratios, respectively. The TGA results for the precursor SnO_2/TiO_2 fibers showed no weight loss upon heating between 550 to 700 °C. Furthermore, the calcined fibers showed no losses throughout the experiment. This concludes that the calcined fibers were completely oxidized with no leftover residue.

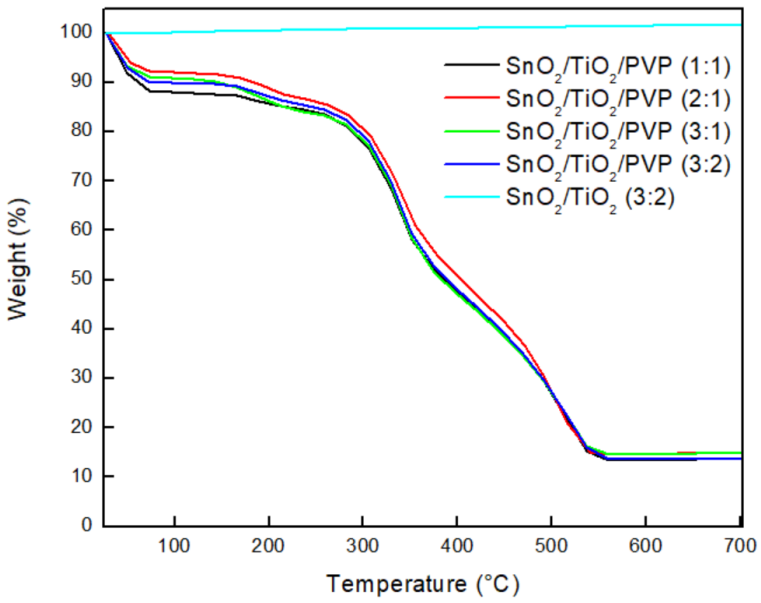

Figure 26: TGA analysis of SnO_2/TiO_2 pre-calcined and calcined fibers.

Figure 27 (a) shows the diffraction pattern of the SnO_2/TiO_2/PVP fibers, which only shows weak broad diffraction peaks for the PVP fibers located at 13.1 and 24.0 in 2θ, which are consistent with the position of the diffraction peaks for PVP [75]. Figure 27 (b) shows the fitting of the diffraction pattern for SnO_2/TiO_2 (2:1) composite fibers after calcination while the fitting results are shown in table 3, which indicated the presence of both TiO_2 and SnO_2 in the crystal structure of the fibers. The fitting was determined to agree with the results reported on the diffraction patterns of both bulk TiO_2 and SnO_2. From the Le Bail fitting, the χ^2 was determined to be 1.67 (a χ^2 below 5 is considered a good fitting). In the SnO_2 phase, the following Bragg peaks were observed at 110 (31.00°), 101 (39.67°), 200 (44.40°), 111 (45.71°), 210 (49.98°), 211 (61.04°), 220 (64.61°), and 002 (68.62°), which indicated the presence of a rutile phase of SnO_2 in the sample. The TiO_2 phase showed the following diffraction peaks: 110 (31.91°), 101 (40.99°), 200 (45.76°), 111 (47.22°), 210 (51.53°), 211 (63.10°), and 220 (66.71°), which indicated the presence of a rutile phase of TiO_2 in the sample. Figure 27 (c) shows the diffraction

patterns collected for the SnO_2/TiO_2 composite fibers at all the synthesis ratios and showed that the synthesized samples have consistent diffraction patterns independent of the ratio of Sn:Ti in the precursor fibers, indicating both SnO_2 and TiO_2 in the sample, were present as their respective rutile phases [76-79].

Table 3: LeBail fitting of the SnO_2/TiO_2 (2:1) calcined fibers.

Phase	Space Group	a(Å)	b(Å)	c(Å)	α(°)	β(°)	γ(°)	χ^2
TiO_2	$P4_2/mnm$	4.638(9)	4.638(9)	3.054(9)	90.0	90.0	90.0	1.67
SnO_2	$P4_2/mnm$	4.737(4)	4.737(4)	3.175(9)	90.0	90.0	90.0	
TiO_2 [79]	$P4_2/mnm$	4.616	4.616	2.977	90.0	90.0	90.0	N/A
SnO_2 [79]	$P4_2/mnm$	4.737	4.737	3.185	90.0	90.0	90.0	N/A

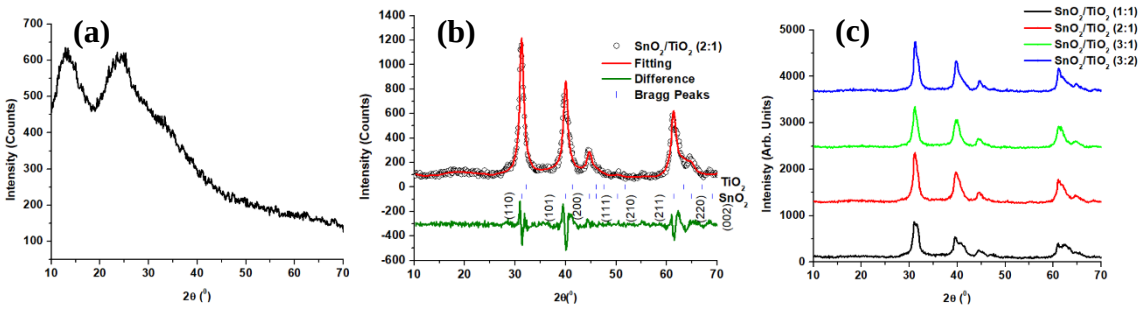

Figure 27: XRD analysis of (a) SnO_2/TiO_2/PVP fibers, (b) SnO_2/TiO_2 (2:1) calcined fibers, and (c) SnO_2/TiO_2 all ratios calcined fibers.

Figure 28 (a-d) shows the XPS spectra collected for the Ti2p which includes the $Ti2p_{3/2}$ and $Ti2p_{1/2}$ regions. Figure 28 (a) shows the $Ti2p_{3/2}$ for the SnO_2/TiO_2 at a ratio of 1:1, 28 (b) shows the 2:1 ratio, 28 (c) shows the 3:1, and 28 (d) shows the 3:2 data. All the SnO_2/TiO_2 XPS data for the $Ti2p_{3/2}$ region were deconvolved into two peaks centered at 457.1 and 457.9 which correspond to the presence of some Ti^{3+} and Ti^{4+} bound to oxygen as is observed in TiO_2 [80]. The lower energy TiO_2 may be due to defects present at the surface. For all the samples, the $Ti2p_{1/2}$ peak was determined to consist of one peak centered at 465 eV, which is consistent with

Ti^{4+} bound to oxygen as is found in TiO_2. The third peak located around 472 eV corresponds to the Ti2p satellite peak [81]. The XPS data agree with the XRD results in that the titanium oxide present in the sample is present as TiO_2.

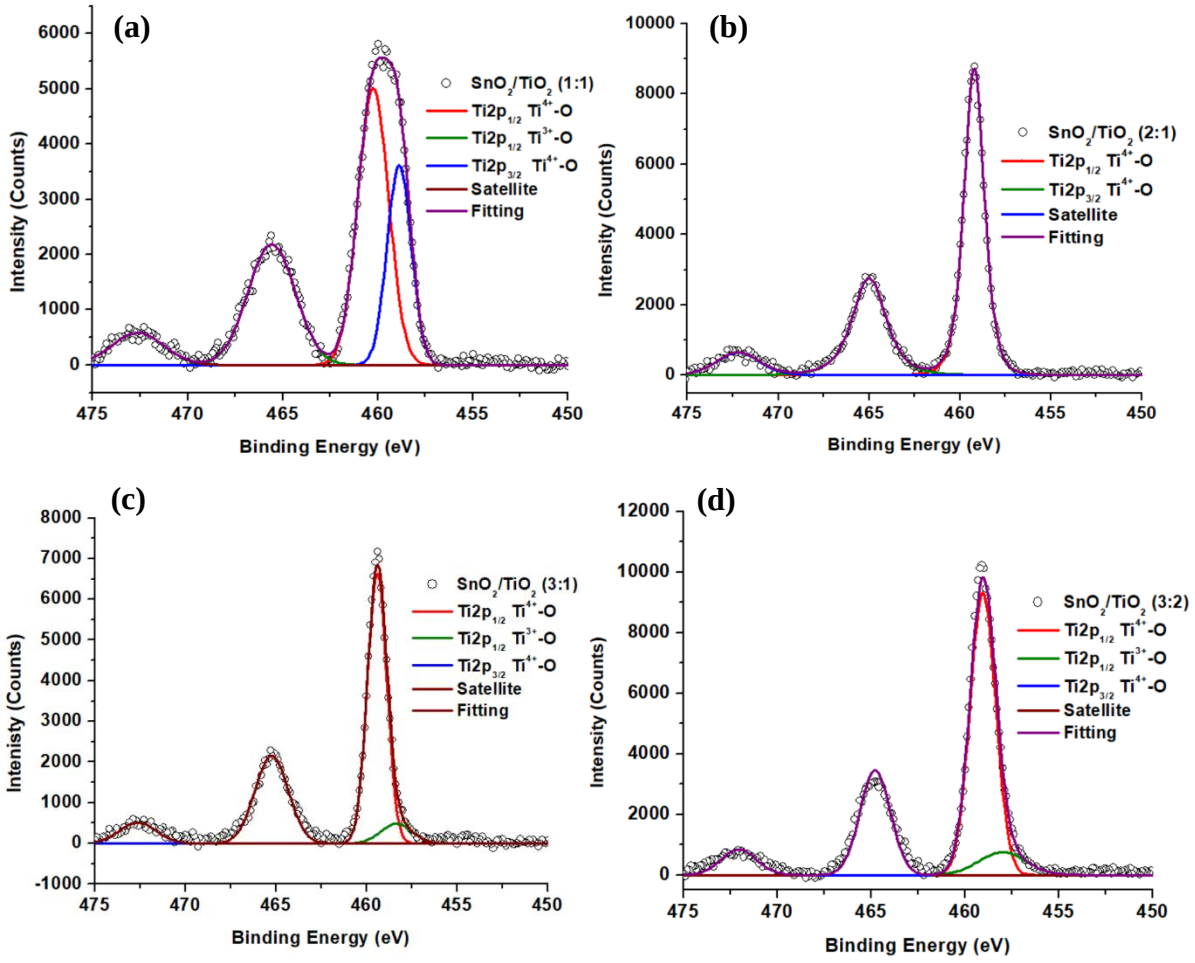

Figure 28: XPS analysis of $Ti2p_{3/2}$ and $Ti2p_{1/2}$ in (a) SnO_2/TiO_2 1:1, (b) 2:1, (c) 3:1, and (d) 3:2 calcined fibers.

Figure 29 (a-d) show the $Sn3d_{5/2}$ and $Sn3d_{3/2}$ XPS region for the SnO_2/TiO_2 data collected for the samples synthesized at different ratios: 29 (a) shows the 1:1, 29 (b) shows the 2:1 ratio, 29 (c) shows the 3:1 and 29 (d) shows the 3:2 data. Superficially, XPS spectra for all samples are similar with two $Sn3d_{5/2}$ and $Sn3d_{3/2}$ peaks located at 486.8 and 495.3 eV,

respectively. The peaks observed at 486.8 eV and 495.3 eV correspond to Sn^{4+}-O binding environment. The XPS results for the SnO_2/TiO_2 composite fibers with 1:1 and 3:2 ratios show an additional peak in the $Sn3d_{5/2}$ and $Sn3d_{3/2}$ regions located at 484.7 and 493.1 eV. The additional peaks may be indicating the presence of a small amount of SnO (Sn(II)O) in the sample as observed in the literature [82].

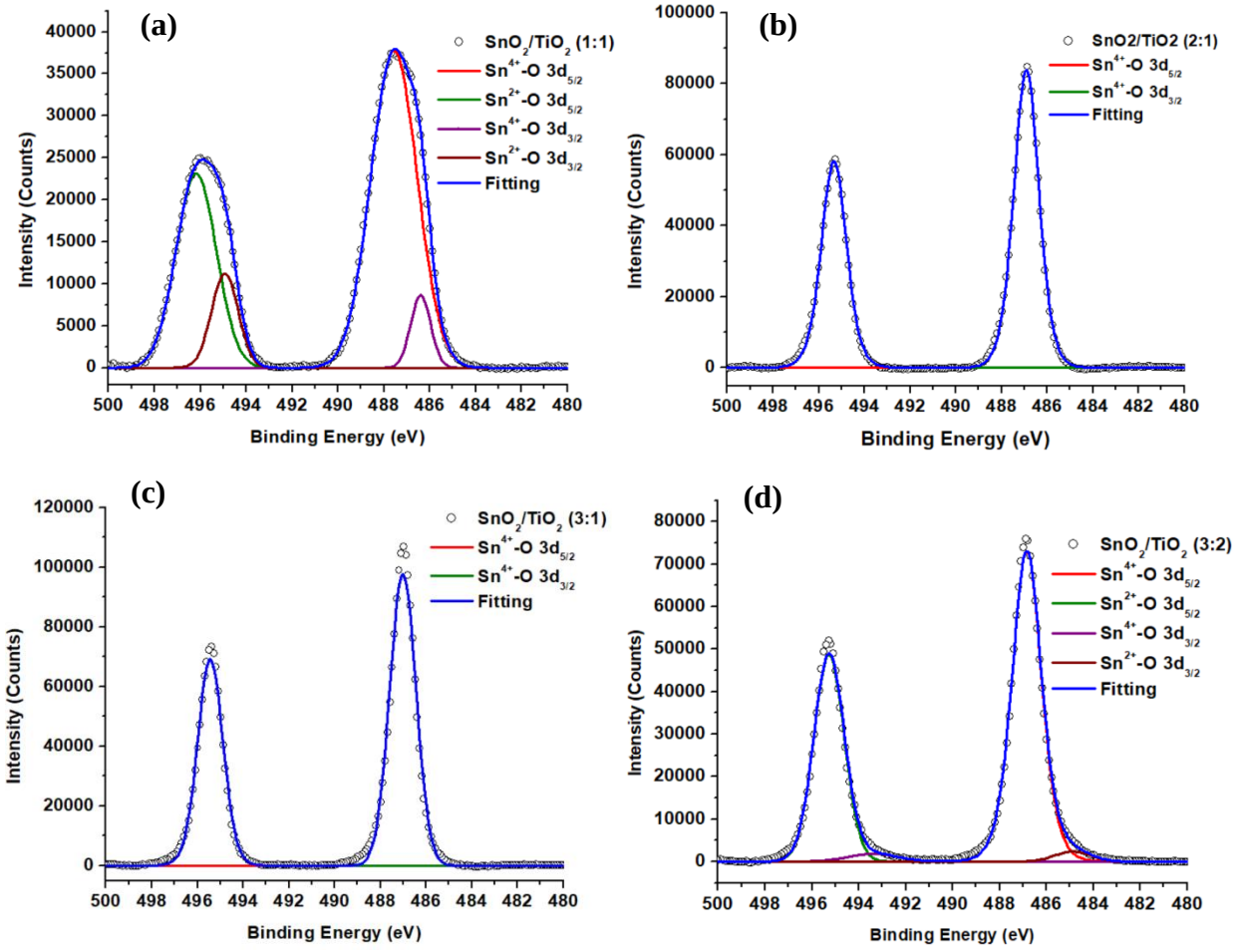

Figure 29: XPS analysis of $Sn3d_{5/2}$ and $Sn3d_{3/2}$ in (a) SnO_2/TiO_2 1:1, (b) 2:1, (c) 3:1, and (d) 3:2 calcined fibers.

Figure 30 (a-d) shows the O1s spectra for SnO_2/TiO_2 composite fibers with different ratios: 30 (a), 30 (b), 30 (c) and 30 (d) show the spectra for the 1:1, 2:1 3:1, and 3:2 ratios,

respectively. The O1s spectra for all samples were deconvolved into two peaks located at 530.7 and 531.6 eV, which have been shown to correspond to oxygen bound to a high oxidation state metal ion such as Ti^{4+} or Sn^{4+} and the presence of oxygen in surface hydroxyl species, respectively [81, 83]. However, the SnO_2/TiO_2 at a ratio of 1:1 shows a higher amount of O than the other samples, this may be due to the formation of carbonate on the surface during the heat treatment [83].

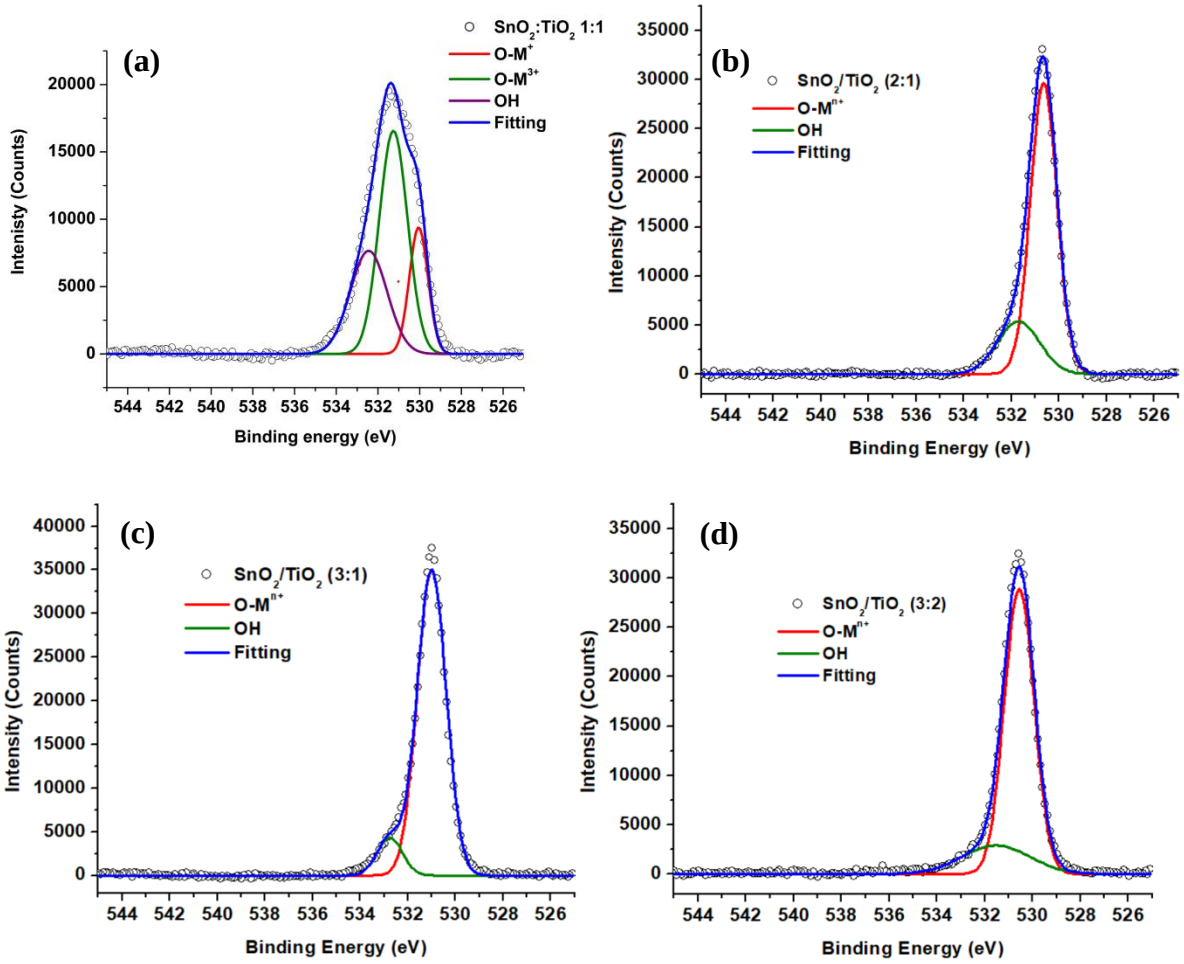

Figure 30: XPS analysis of O1s spectra in (a) SnO_2/TiO_2 1:1, (b) 2:1, (c) 3:1, and (d) 3:2 calcined fibers.

Figure 31 (a-d) shows the C1s XPS spectrum for the SnO_2/TiO_2 calcined fibers with different ratios: 31 (a), 31 (b), 31 (c), and 31 (d) show the spectra for the 1:1, 2:1, 3:1 and 3:2 ratios, respectively. The amount of carbon present in the samples is very low as indicated by the low counts observed in the spectrum. The carbon spectra for all the samples were deconvolved into two peaks located at 285.6 and 288.6 eV, which correspond to C in an Sp3 bond (C-C) and the presence of oxidized carbon (C=O) [83].

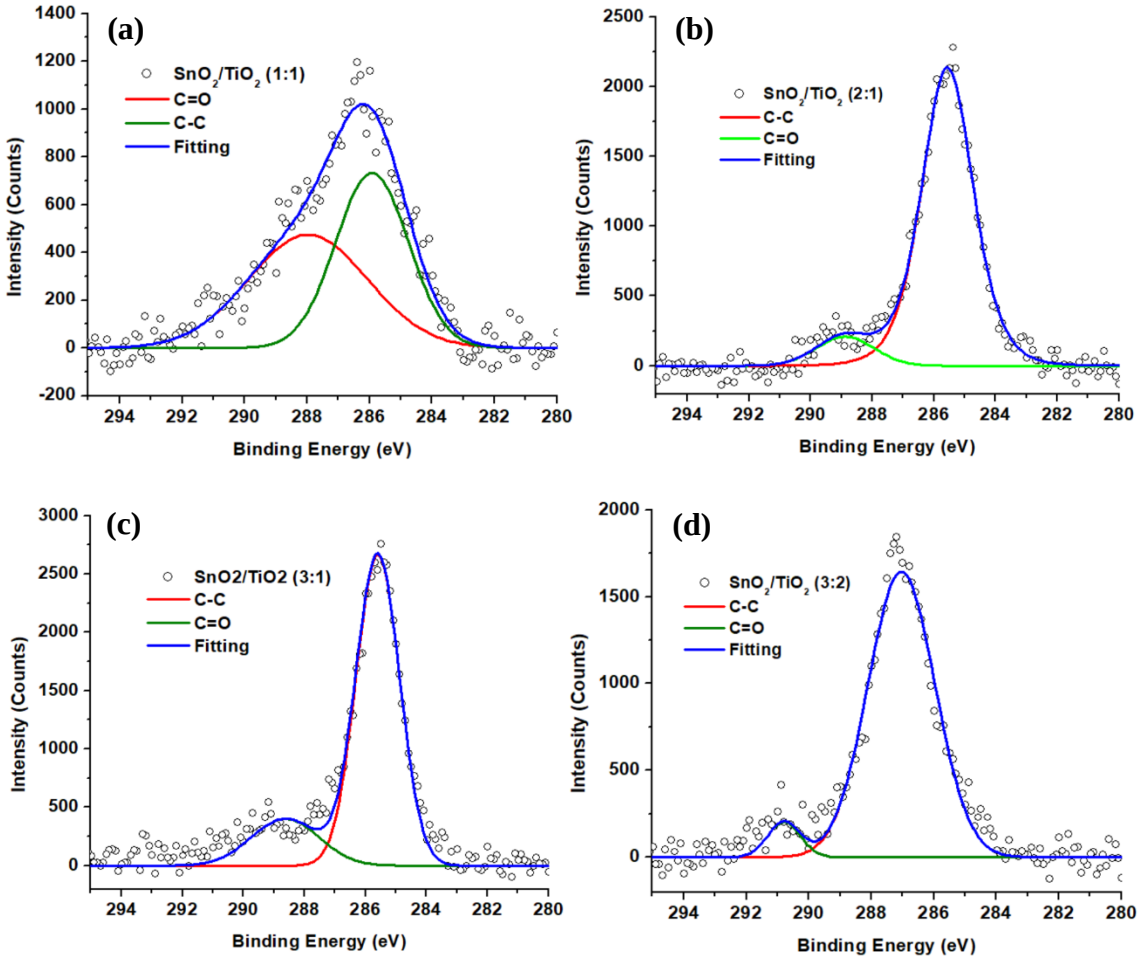

Figure 31: XPS analysis of C1s spectra in (a) SnO_2/TiO_2 1:1, (b) 2:1, (c) 3:1, and (d) 3:2 calcined fibers.

Figure 32 shows the Raman spectra for the (a) precursor fibers and (b) SnO_2/TiO_2 composite fibers with 1:1 ratio. Figure 32 (a) shows the spectra vibrations of the precursor fibers at 549, 748, 927, and 1477 cm^{-1}, which are consistent with the Raman spectra found in the literature for PVP fibers[84, 85]. Figure 32 (b) shows the Raman spectra for the SnO_2/TiO_2 (1:1) sample which show the following vibrations, 153.3, 243.1, 341.5, 424.0, 606.36, and 786.8 cm^{-1}. The peaks correspond to a mixture of TiO_2 (rutile phase) and SnO_2 (cassiterite phase) which was observed in the x-ray diffraction patterns. The stretches located 150, 243.1, 445.610, and 610 cm^{-1} correspond to the TiO_2 Rutile B_{1g}, multiphoton processes, E_g, and A_{1g} processes occurring in the TiO_2 rutile materials [86]. In addition, the vibration at 341.5 cm^{-1} can be attributed to multi-photon processes. The SnO_2 Raman vibration for the most part is not visible in the spectrum due to their intensities buried by the TiO_2 rutile vibrations [87]. However, the peak observed at 786.8 cm^{-1} can be characterized as the SnO_2 B_{2g} vibration.

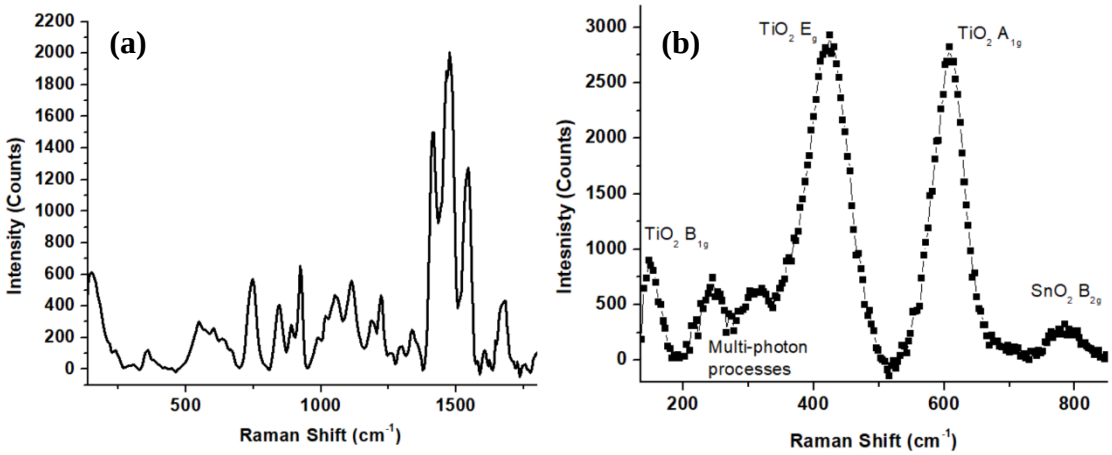

Figure 32: Raman analysis of (a) SnO_2/TiO_2/PVP pre-calcined fibers and (b) SnO_2/TiO_2 (1:1) calcined fibers.

3.5 Electrochemical Performance of Non-Coated Active Material

The electrochemical performances for the non-coated active material was conducted using various tests. The cyclic performance was analyzed by galvanostatic charge/discharge testing with a voltage potential range between 0.5 – 3.0 V and a current density of 100 mA g^{-1}. The rate performance was conducted to analyze the materials' rate capability by running the test with different current densities. Additionally, the materials' redox reactions were analyzed by conducting cyclic voltammetry (CV) experiments at a voltage range between 0.1 – 3.0 V with a scan rate of 0.1 mV s^{-1} for 4 cycles. Lastly, the resistance of the battery cell was studied by electrochemical impedance spectroscopy (EIS).

3.5.1 Cycle Performance of Non-Coated Material

The non-coated material of all the different ratios were compared to their parent materials of SnO_2 and TiO_2 to analyze the different contributions each one had on the composite material. Likewise, the different ratios were compared to one another to single out the best ratio. This ratio would then be coated with the CVD method.

Initially, the cycle performance was the first test conducted on all the materials. Figure 33 shows the data for the SnO_2 and TiO_2 parent materials. As mentioned in literature, SnO_2 has a high capacity and in figure 33 (a) it shows that SnO_2 has an irreversible discharge specific capacity of 2365 mAh g^{-1}. After the first discharge the battery's first charge has a capacity loss of 43.5 % (1337 mAh g^{-1}) indicating the formation of the SEI layer. Consequently, SnO_2 quickly starts to fade with a steep incline presented in figure 33 (c). After 10 cycles, the battery has lost 32% of its initial charge capacity from 1337 to 910 mAh g^{-1}. At 100 cycles, the anode has inevitably been pulverized due to the vast volume change experienced. This results in the battery ending with a low charge specific capacity of 95 mAh g^{-1} and a poor capacity retention (from

first charge to last charge) of 7.1 %. Furthermore, the Coulombic efficiency of the SnO_2 battery from figure 33 (d) shows an efficiency of around 90 % between the 2^{nd} and 40^{th} cycles indicating poor cyclability. Afterwards, the efficiency increases to >98 % for the rest of the cycles indicating good cyclability for the second half of its life. On the other hand, TiO_2 has shown to have low capacity and in the data, it has an irreversible discharge specific capacity of 815 mAh g^{-1} as shown in figure 33 (c). However, the SEI layer that forms between the first cycle greatly reduces the specific capacity by 66.0 % resulting in a charge specific capacity of 277 mAh g^{-1}. Fortunately, the TiO_2 data stays consistent and after 35 cycles it has surpassed the charge specific capacity of SnO_2 with 264 mAh g^{-1}. After 100 cycles, the TiO_2 battery has a charge specific capacity of 307 mAh g^{-1} (212 more than SnO_2 at 100 cycles) and a superior capacity retention of 110.8 %. Table 4 shows the cycle performance data of SnO_2 and TiO_2. Additionally, figure 33 (d) shows the efficiency of the TiO_2 battery to be >95 % after the 4^{th} cycle indicating great cyclability throughout its 100 cycles. The work done in this project is to combine these two materials and combine them to bring out the best of both: the high capacity of SnO_2 and the stable life cycle of TiO_2. After finding the best composite material CVD will be performed to analyze the effects of carbon-coating.

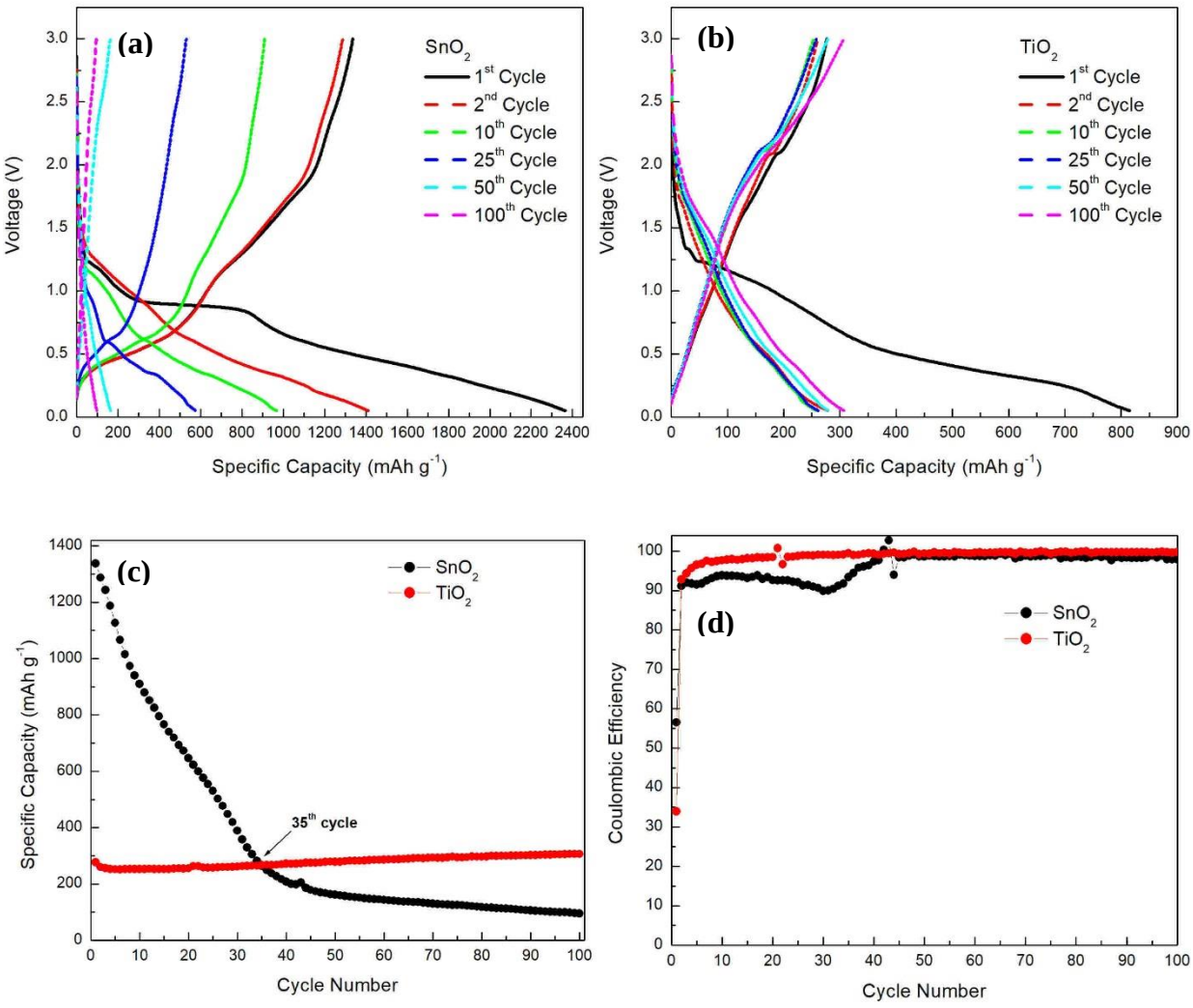

Figure 33: Charge/discharge curves of (a) SnO_2 and (b) TiO_2, charge specific capacity cycle performances of SnO_2 and TiO_2, and (d) Coulombic efficiency of SnO_2 and TiO_2 over 100 cycles at a current density of 100 mA g^{-1}.

Table 4: Cycle performance data for SnO_2 and TiO_2.

Material	**Initial Specific Discharge Capacity (mAh g^{-1})**	**Specific Charge Capacity (mAh g^{-1})**		**SEI Layer Capacity Loss (%)**	**Capacity Retention (%)**
		1st Cycle	100th Cycle		
SnO_2	2365	1337	95	43.5	7.1
TiO_2	815	277	307	66.0	110.8

Afterwards, the different ratios of the composite material were analyzed to single out the best performing ratio. Figure 34 shows the data for the different SnO_2/TiO_2 ratios. During the initial charge/discharge cycle, the 3:1 ratio has the highest specific capacity with 1677 mAh g^{-1} followed by 3:2 (1600 mAh g^{-1}), 2:1 (1542 mAh g^{-1}), and 1:1 (1475 mAh g^{-1}). After the first discharge, the SEI layer forms and reduces the capacities of all the ratios as shown in figure 34 (a). The resulting charge specific capacities are 956 mAh g^{-1} for 3:1 (specific capacity loss of 42.99 %), 854 mAh g^{-1} for 3:2 (46.63 % loss), 886 mAh g^{-1} for 2:1 (42.54 % loss), and 732 mAh g^{-1} for 1:1 (50.37 % loss). The 3:1 ratio maintains the highest capacity after the SEI layer formed followed by 2:1, 3:2 and 1:1. After 100 cycles, figure 34 (b) shows that the 3:1 ratio has the highest charge specific capacity at 289 mAh g^{-1} followed by 1:1 with 190 mAh g^{-1}, 2:1 with 172 mAh g^{-1}, and 3:2 with 125 mAh g^{-1}. The results show a capacity retention of 30.23 % for 3:1, 25.96 % for 1:1, 19.41 % for 2:1, and 14.64 % for 3:2. Figure 34 (c) shows a visual comparison of the life cycle of each ratio. It shows an initial correlation between the amount of SnO_2 in the material and the charge specific capacity of the battery: the higher the SnO_2 content the higher the specific capacity. At the end of 100 cycles this correlation is not so obvious. The previous results are presented in table 5. Figure 34 (d) shows the efficiency of each ratio. During the first cycles (2-30), the efficiencies for 1:1, 2:1, and 3:1 show steady efficiencies between 94 and 99 % while 3:2 has an inconsistent efficiency between 91 and 98 %. Towards the middle cycles (31-70), the efficiencies for 3:1 and 3:2 become inconsistent between 93 and 101 % while 1:1 and 2:1 maintain consistent efficiencies between 95 and 100 %. In the final cycles (71-100), the efficiencies of all ratios start to trend towards high and consistent percentages between 97 and 100 %. The ranges that the ratios show throughout their life cycles show poor cyclability and should be improved upon to be consistent above 98 %. Overall, the data in figure 34 shows the

3:1 battery to have the highest initial and final specific capacity, and it is the ratio to be further analyzed and compared to its parent materials and be carbon-coated by CVD.

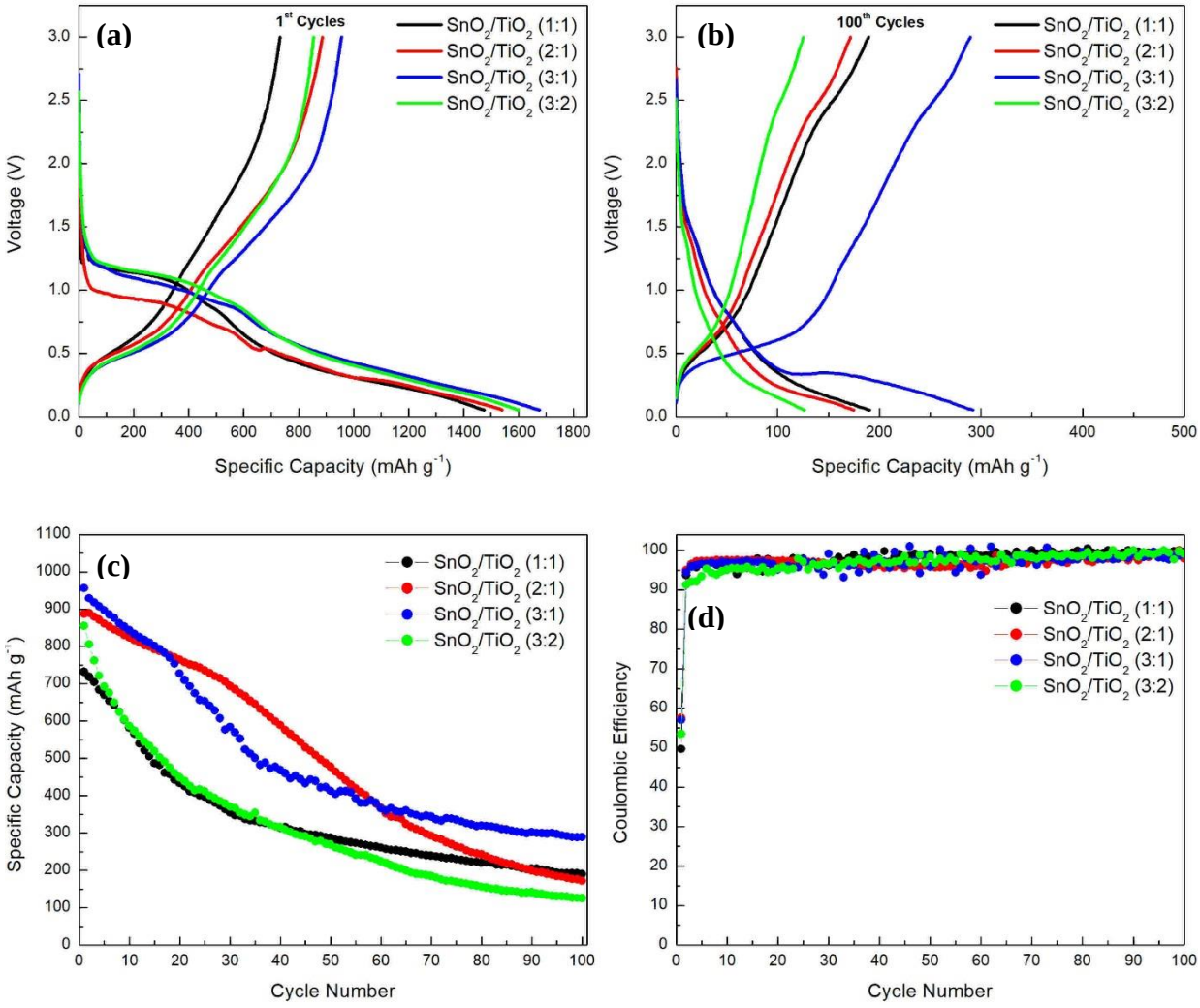

Figure 34: Charge/discharge curves of SnO_2/TiO_2 all ratios of (a) 1st cycles and (b) 100th cycles, (c) charge specific capacity cycle performances, and (d) Coulombic efficiency over 100 cycles at a current density of 100 mA g-1.

Table 5: Cycle performance data for all SnO_2/TiO_2 ratios.

SnO_2/TiO_2 Ratio	Initial Specific Discharge Capacity (mAh g^{-1})	Specific Charge Capacity (mAh g^{-1})		SEI Layer Capacity Loss (%)	Capacity Retention (%)
		1st Cycle	100th Cycle		
1:1	1475	732	190	50.37	25.96
2:1	1542	886	172	42.54	19.41
3:1	1677	956	289	42.99	30.23
3:2	1600	854	125	46.63	14.64

To compare the 3:1 sample to its parent materials, figure 35 shows the cycle performances and Coulombic efficiency of SnO_2, TiO_2, and SnO_2/TiO_2 (3:1) for the first 100 cycles. Table 6 and figure 35 (a) and (b) show that the composite ratio of 3:1 has enough SnO_2 to start with a high irreversible specific capacity of 1677 mAh g^{-1}, which is 29.1 % less than SnO_2. It also has enough TiO_2 to keep the capacity retention after 100 cycles at 30.2 %, which is significantly better than the 7.1 % of SnO_2 but considerably worse than the 110.8 % of TiO_2. Furthermore, the 3:1 ratio had a capacity loss due to the formation of the SEI layer of 43.0 %, which is similar to the capacity loss of SnO_2 at 43.5 % and a significant improvement from the loss of 66.0 % of TiO_2. In figure 35 (c), it shows that the composite material of SnO_2/TiO_2 (3:1) surpasses the specific capacity of SnO_2 after 14 cycles at 810 mAh g^{-1}. After 89 cycles the 3:1 ratio's specific capacity falls below TiO_2 at 299 mAh g^{-1}. However, the 3:1 ratio outperformed both SnO_2 and TiO_2 for 75 of its 100 cycles. In figure 35 (d), the comparison of efficiencies between the three samples shows that the TiO_2 sample had the best cyclability, a quality that was not reflected in the 3:1 ratio.

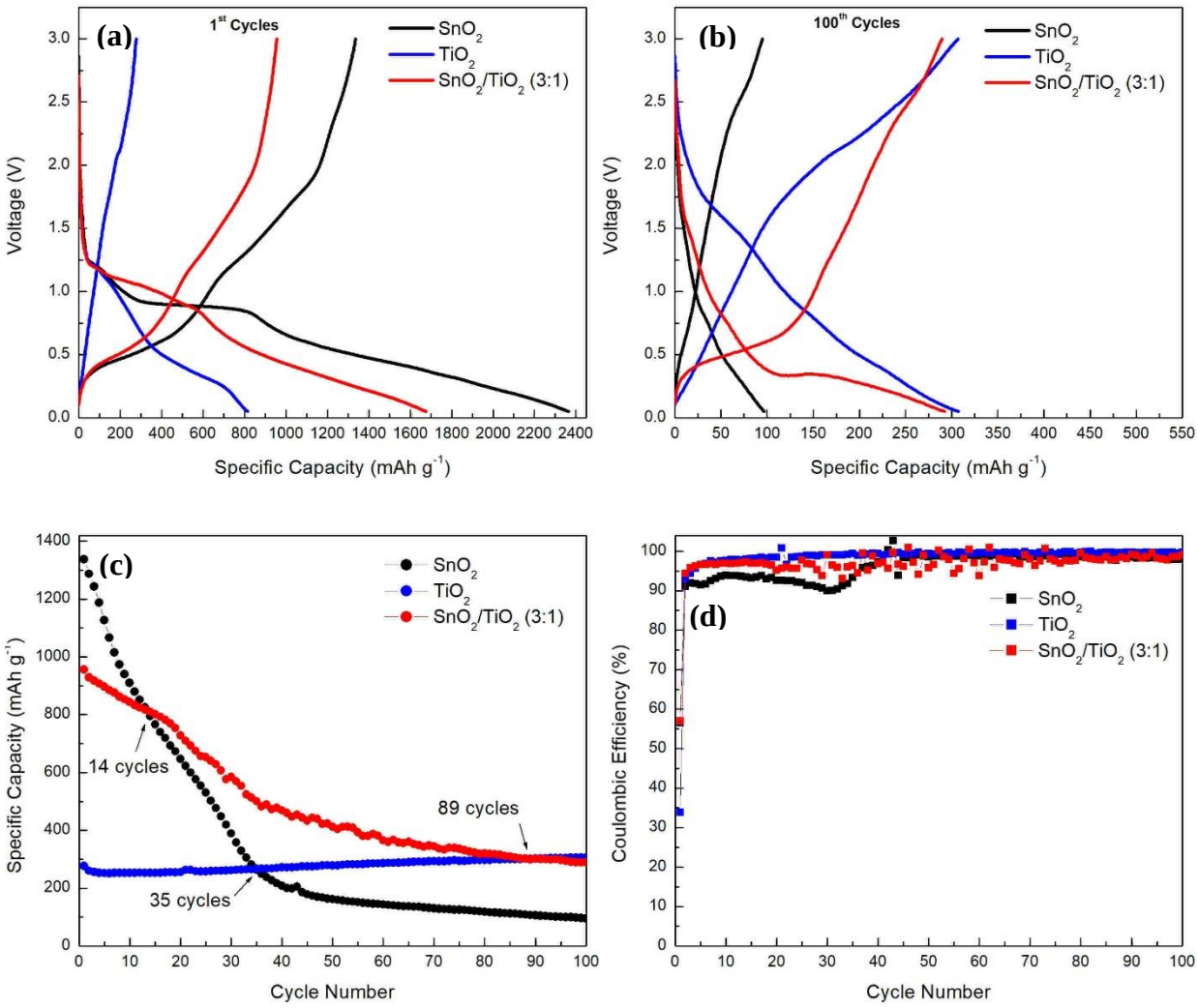

Figure 35: Charge/discharge curves of SnO_2, TiO_2, and SnO_2/TiO_2 (3:1) of (a) 1st cycles and (b) 100th cycles, (c) charge specific capacity cycle performances, and (d) Coulombic efficiency over 100 cycles at a current density of 100 mA g^{-1}.

Table 6: Cycle performance data for SnO_2, TiO_2, and SnO_2/TiO_2 (3:1).

Material	**Initial Specific Discharge Capacity (mAh g^{-1})**	**Specific Charge Capacity (mAh g^{-1})**		**SEI Layer Capacity Loss (%)**	**Capacity Retention (%)**
		1st Cycle	100th Cycle		
SnO_2	2365	1337	95	43.5	7.1
TiO_2	815	277	307	66.0	110.8
3:1	1677	956	289	43.0	30.2

3.5.2 Rate Performance of Non-Coated Material

Apart from cycle performance, rate performance tests were also performed. The tests are conducted to analyze the batteries' performances under different current densities (50, 100, 200, 400, 500, and 50 mA g^{-1}) compared to the cycle performance test of a constant current density of 100 mA g^{-1}. Each current density is performed for 10 cycles for a total of 60 cycles. Figure 36 shows the rate performances of SnO_2, TiO_2, and SnO_2/TiO_2 (3:1). The data reinforces the cycle performance data in which SnO_2 starts with a high charge specific capacity (1358 mAh g^{-1}) followed by a steep decline to 965 mAh g^{-1} (28.9 % loss) at the end of the current density cycle due to the pulverization of the anode. As the current density ramps up the charge specific capacity falls. At 500 mA g^{-1} the charge specific of SnO_2 falls below TiO_2 to 37 mAh g^{-1} (97.3 % loss) before increasing to 204 mAh g^{-1} and finishing with 135 mAh g^{-1} at 50 mA g^{-1}. This results in a capacity retention (between initial and final current density of 50 mA g^{-1}) of 9.94 %. Similar to the cycle performance, TiO_2 starts at a low charge specific capacity (214 mAh g^{-1}) and maintains a consistent charge specific capacity throughout the current densities. In fact, the TiO_2 sample gains capacity at 200, 400, 500 and 50 mA g^{-1} with gains of 5.60, 10.3, 11.1, and 1.72 %, respectively. At the final current density, the TiO_2 sample ends with an impressive capacity retention of 82.7 %. Furthermore, the 3:1 ratio followed the same trend as the SnO_2 parent material with a high initial charge specific capacity of 940 mAh g^{-1} followed by a decline to 808 mAh g^{-1} (14 % loss) due to the pulverization of the anode. At 500 mA g^{-1} the charge specific capacity falls to 190 mAh g^{-1} (79.8% loss) and rises to 494 mAh g^{-1} at 50 mA g^{-1}. The 3:1 sample finishes with a capacity retention of 40.3 %. Table 7 shows the data for the rate performances.

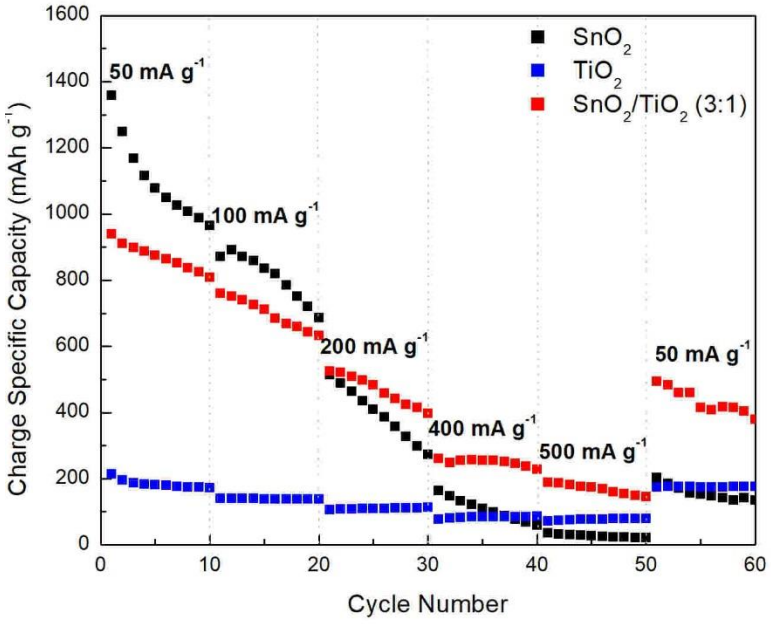

Figure 36: Rate performance data for SnO_2, TiO_2, and SnO_2/TiO_2 (3:1) at varying current densities of 50, 100, 200, 400, 500, and 50 mA g^{-1}.

Table 7: Rate performance data for SnO_2, TiO_2, and SnO_2/TiO_2 (3:1).

Material	**Initial / Final Charge Specific Capacity (mAh g^{-1}) (Capacity Gain/Loss (%))**						**Capacity Retention (%)**
	50 mA g^{-1}	**100 mA g^{-1}**	**200 mA g^{-1}**	**400 mA g^{-1}**	**500 mA g^{-1}**	**50 mA g^{-1}**	
SnO_2	1358 / 965 (-28.9)	872 / 687 (-21.2)	514 / 274 (-46.7)	164 / 59 (-64.0)	37 / 21 (-43.2)	204 / 135 (-33.8)	9.94
TiO_2	214 / 173 (-19.2)	141 / 139 (-1.42)	107 / 113 (+5.60)	78 / 86 (+10.3)	72 / 80 (+11.1)	174 / 177 (+1.72)	82.7
3:1	940 / 808 (-14.0)	760 / 632 (-16.8)	526 / 397 (-24.5)	260 / 229 (-11.9)	190 / 146 (-23.2)	494 / 379 (-23.3)	40.3

3.5.3 Cyclic Voltammetry for Non-Coated Material

The lithiation/de-lithiation reactions of the sample anodes were studied using cyclic voltammetry tests. The tests were performed for four cycles using a voltage window of 0.01 – 3 V at a scan rate of 0.1 mV s^{-1}. Figure 37 shows the cyclic voltammogram of the first three cycles for (a) SnO_2, (b) TiO_2, and (c) SnO_2/TiO_2 (3:1), as well as (d) the first cycles of all three samples

together. All three samples (figure 37 (a-c)) show a difference between the first cycle (black line) and the second cycle (red line), indicating the formation of the solid electrolyte interface (SEI) layer on the surface of the electrode. Afterward, the second and third cycles (red and blue lines) overlap, indicating good reversibility and high Coulombic efficiency.

In figure 37 (a), the SnO_2 sample shows two main reduction peaks occurring during the first discharge cycle at 0.7 and 0.14 V, which are due to the irreversible formation of the Li_2O-SEI layer and the reduction of SnO_2 to Sn (eq. 1) and the alloying formation of Li_xSn (eq. 2 where x = 4.4), respectively. It also shows a minor peak at 1.12 V, which is due to the initial reduction of SnO_2. This minor peak becomes more evident in subsequent cycles at 1.18 and 0.91 V. Conversely, the SnO_2 sample shows three oxidation peaks occurring at 0.54, 1.25, and 1.85 V due to the dealloying of Li_xSn, the re-oxidation of Sn to SnO, and the continued re-oxidation of SnO to SnO_2 (eq. 3) [19, 66, 88]. The CV results closely match Zhao et al. results using SnO_2/Sn sample with reported initial cathodic peaks of 0.71 and 0.08 V and anodic peaks of 0.60, 1.29, and 1.82 V [66]. Furthermore, the cathodic peaks after the first cycle shift to a higher voltage (a shift to the right) at 0.16 and 0.29 V and indicate the alloying process of Li_xSn (eq. 2). The process of the SnO_2 reduction/oxidation can be written out in the following equations:

$$SnO_2 + 4Li^+ + 4e^- \rightarrow Sn + 2Li_2O \quad (1)$$

$$Sn + xLi^+ + xe^- \leftrightarrow Li_xSn\ (0 \leq x \leq 4.4) \quad (2)$$

$$SnO_2 + xLi^+ + xe^- \leftrightarrow Li_xSnO_2 \quad (3)$$

Figure 37 (b) shows the first three cycles of TiO_2 batteries. The sample shows one main reduction peak at 1.0 V, which does not correspond to any subsequent cycles indicating the formation of the SEI layer. This reduction peak is similar to peaks found in literature at ~1.3 V [89] and 1.1 V [90]. The TiO_2 sample also shows two minor peaks at 1.36 and 1.72 V which

indicates the reduction of TiO_2 to TiO to Ti. Additionally, the oxidation process shows a peak at 2.1 V that is attributed to the de-lithiation of Li_xTiO_2 (eq. 4). The anodic peaks overlap with the second and third cycles indicating good reversibility. The following equation can express the reversible lithium insertion/extraction process [67]:

$$TiO_2 + xLi^+ + xe^- \leftrightarrow Li_xTiO_2 \qquad (4)$$

Figure 37 (c) shows the first three cycles of the composite sample SnO_2/TiO_2 (3:1). The CV shows a similarity between the composite sample and the parent sample of SnO_2. The main cathodic peaks of the composite sample are 0.84 and 0.05 V (compared to the peaks of SnO_2 at 0.7 and 0.14 V), which result from the formation of the SEI layer and reduction of SnO_2 to Sn and the alloying of Sn and Li. There is also a minor peak of 1.15 V (compared to the minor peak of SnO_2 at 1.12 V) indicating the initial reduction of SnO_2 to SnO. Similarly, the anodic peaks of the composite sample are 0.62, 1.29, and 1.9 V (compared to SnO_2 peaks at 0.54, 1.25, and 1.85 V), which are the results of the dealloying of Sn and Li and the reoxidation of SnO_2. These cathodic peaks are also found in literature at 1.68, 0.78, and 0.02 V as well as the anodic peaks at 0.56, 1.32, and 2.5 V [91]. The subsequent cycles show curves that overlap, indicating good reversibility. The close similarities between the SnO_2 and the composite sample could be due to the low current responses of TiO_2 (current range from -0.66 – 0.12 mA) compared to SnO_2 (current range from -3.41 – 1.42 mA), causing the reaction voltage to minimally shift the voltage to the right and minimally reduce the current at which the reactions happen. The scale of this occurrence can be noticed visually in figure 5(d), where the first cycles of each sample are shown together; the peaks of the SnO_2 sample (black line) are the biggest, followed by the 3:1 composite sample (blue line) and lastly by the TiO_2 sample (red line).

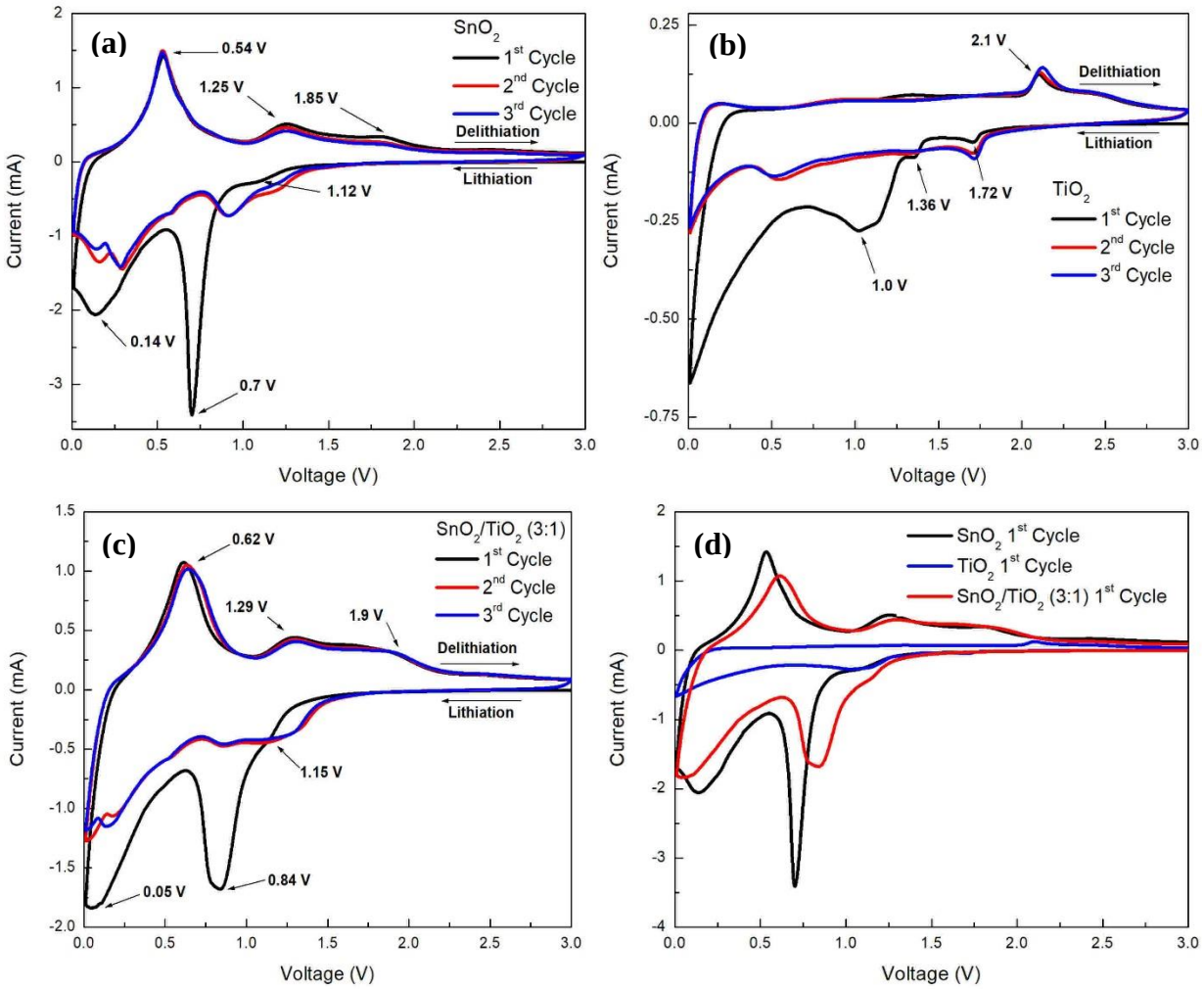

Figure 37: Cyclic voltammetry of the first three cycles for (a) SnO_2, (b) TiO_2, and (c) SnO_2/TiO_2 (3:1), as well as (d) the first cycles of all three samples.

3.5.4 Electrochemical Impedance Spectroscopy (EIS) of Non-Coated Material

Electrochemical impedance spectroscopy (EIS) tests were utilized to study the batteries electrochemical kinetics. The tests were done in a range from 0.1 to 100,000 Hz and graphed with the imaginary axis of -Z'' (Ohm) vs. the real axis of Z' (Ohm). Figure 38 (a) shows the Nyquist plots for the different sample batteries. Nyquist plots are used to visually explain the batteries' impedances and are shown as a depressed semi-circle (high-medium frequeny range) with a sloping tail (low frequency range). In general, Li-ion batteries behave like an electrical

circuit comparible to a resistor (R_s) in series with a resistor (R_p) and a Warburg impedance (W) that are in parallel with a double layer capacitance (CPE) as shown in figure 38 (c-e) [92]. The first resistor, R_s, is the resistance of the electrolyte solution and its value is associated with the distance between the origin and the first x-value before the semi-circle begins. The second resistor, R_p, also known as R_{ct}, is representative of the entire depressed semi-circle and is the polarization resistance (charge transfer resistance) within the interface between the electrolyte solution and the electrodes. The CPE variable is the constant phase element with the Y_0 variable representing the resistance in Mho and the "N" variable representing a constant ranging between 0 and 1; if N = 1 then the CPE acts as an ideal capacitor [93]. In the low frequency range, the sloping tail corresponds with the Warburg resistance that relates to the diffusion of Li^+ in the electrode and is represented by the variable Y_0 in Mho. Additionally, the Warburg resistance can be used to find the Warburg factor, σ, by calculating the slope of the real resistance (Z') vs the inverse square root of the angular velocity ($\omega^{-1/2}$) plot in figure 38 (b) [94].

According to the results found in table 8, the SnO_2 sample has the lowest Warburg factor indicating higher diffusivity of Li^+. The solution resistance for all samples are similar with a small range between 4.33 and 7.84 Ω (3:1 and SnO_2, respectively). The polarization resistance of the samples shows that the 3:1 sample has the lowest resistance with a value of 135 Ω, which is graphically represented in figure 38 (a) by having a smaller semi-circle diameter. The low charge transfer resistance could be explained by the synergetic effect of the SnO_2 and the TiO_2 material.

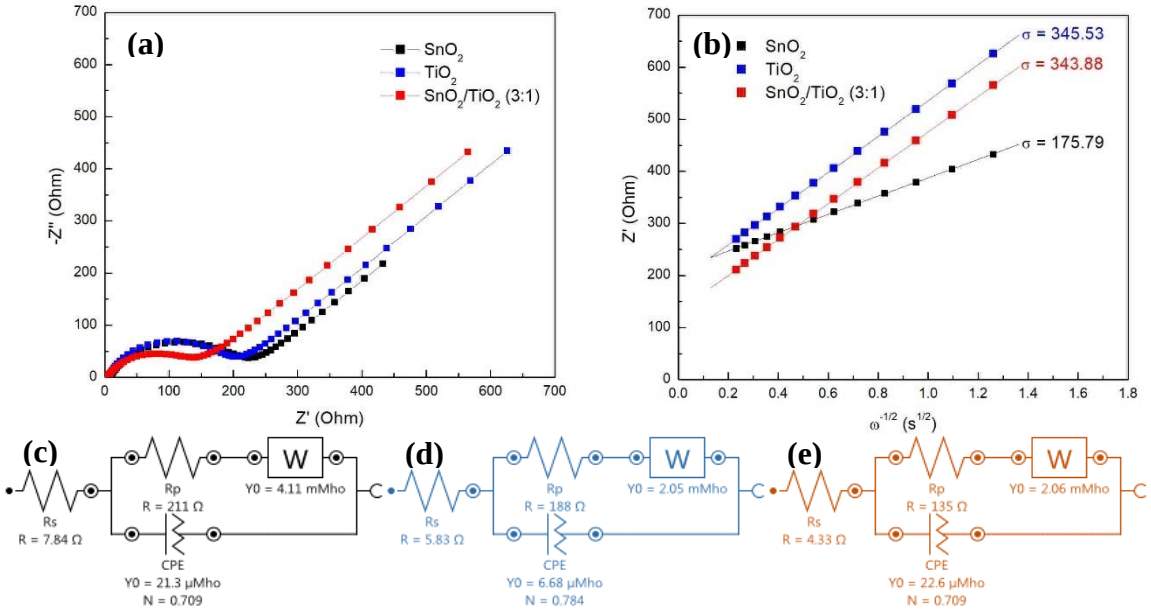

Figure 38: EIS data of (a) fitted Nyquist plot and (b) Warburg plot for SnO_2, TiO_2, and SnO_2/TiO_2 (3:1), and equivalent circuits for (c) SnO_2, (d) TiO_2, and (e) SnO_2/TiO_2 (3:1).

Table 8: Nyquist data for equivalent circuits of SnO_2, TiO_2, and SnO_2/TiO_2 (3:1).

Sample	Rs (Ω)	Rp (Ω)	CPE		W	σ (Ω $s^{-0.5}$)
			Y_0 (μMho)	N	Y_0 (mMho)	
SnO_2	7.84	211	21.3	0.709	4.11	175.79
TiO_2	5.83	188	6.68	0.784	2.05	345.53
SnO_2/TiO_2 (3:1)	4.33	135	22.6	0.709	2.06	343.88

3.6 Structure Characterization of Coated Active Material

The structure and morphology of the SnO_2/TiO_2 (3:1) CVD 30- and 60-min active materials were characterized by SEM, EDS, TGA, XPS, XRD and Raman spectroscopy. The coated active materials were sprayed with gold particles using sputtering method to collect clearer images from SEM and EDS. They were also placed in the TGA and heated to 800 °C under an argon atmosphere and continued to 1000 °C in air at a rate of 5 °C/min to examine the thermal degradation.

The morphology and structure of the SnO_2/TiO_2 (3:1) CVD 30- and 60-min active materials were analyzed by SEM using 500x, 2000x, 5000x, and 10000x magnification. Figure 39 (a-h) shows the SEM images. Both the 30- and 60-min images show big rock-like structures ranging from 2 to 10 μm. Upon closer inspection some micro-belt structures were found scattered across the sample area. After the deposition of carbon-coating at 1000 °C, some of the material fused together to form large rock-like structures from the small particles placed in the furnace. To prevent a poor thin-film application onto the copper foil, the carbon-coated material was placed in a grinder and mixer to grind the material into smaller particles.

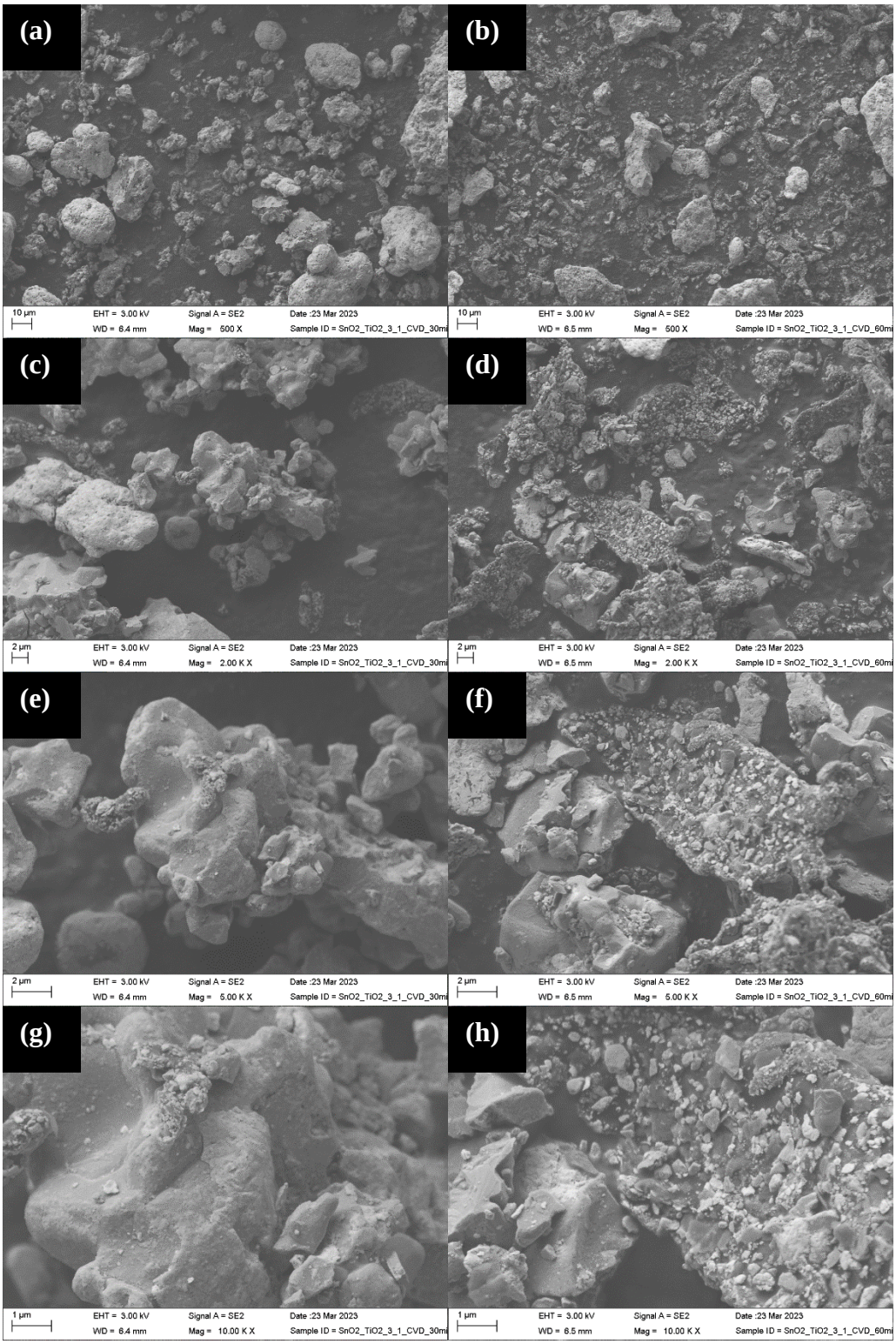

Figure 39: SEM images of SnO_2/TiO_2 (3:1) CVD 30- and 60-min at 500x (a-b), 2000x (c-d), 5000x (e-f), and 10000x (g-h) magnifications.

Figure 40 shows the EDS mapping of the SnO_2/TiO_2 (3:1) CVD 30-min sample. The mapping shows the material consists of the same elements as the pristine fibers and calcined micro-belt fibers: carbon (C), nitrogen (N), oxygen (O), tin (Sn), and titanium (Ti). However, the amount of Sn and Ti are completely different. For the SnO_2/TiO_2 (3:1) pristine fibers the weight % for Sn was 13.91 % and 2.97 % for Ti. For the SnO_2/TiO_2 (3:1) calcined fibers the weight % was 75.38 % and 8.49 %. In each mapping report the ratio stayed within the 3:1 ratio (65.3 %: 35.7 % and 78.2 %: 21.8 %, respectively), but in the CVD 30-min report, table 9, the ratio is Ti-heavy with a ratio of 19.7 %: 80.3 %. Figure 40 also shows that the elements are clustered together as opposed to being well-mixed like the calcined micro-belt fibers. The overlay image in figure 40 shows Sn (yellow) concentrated to the white rock-like structures, while the Ti (cyan) is concentrated to the bigger gray rock-like structures. Oxygen and nitrogen are spread across the entire area, while the carbon is concentrated to black pieces that seem to be broken up from smaller pieces similar to figure 39 (h).

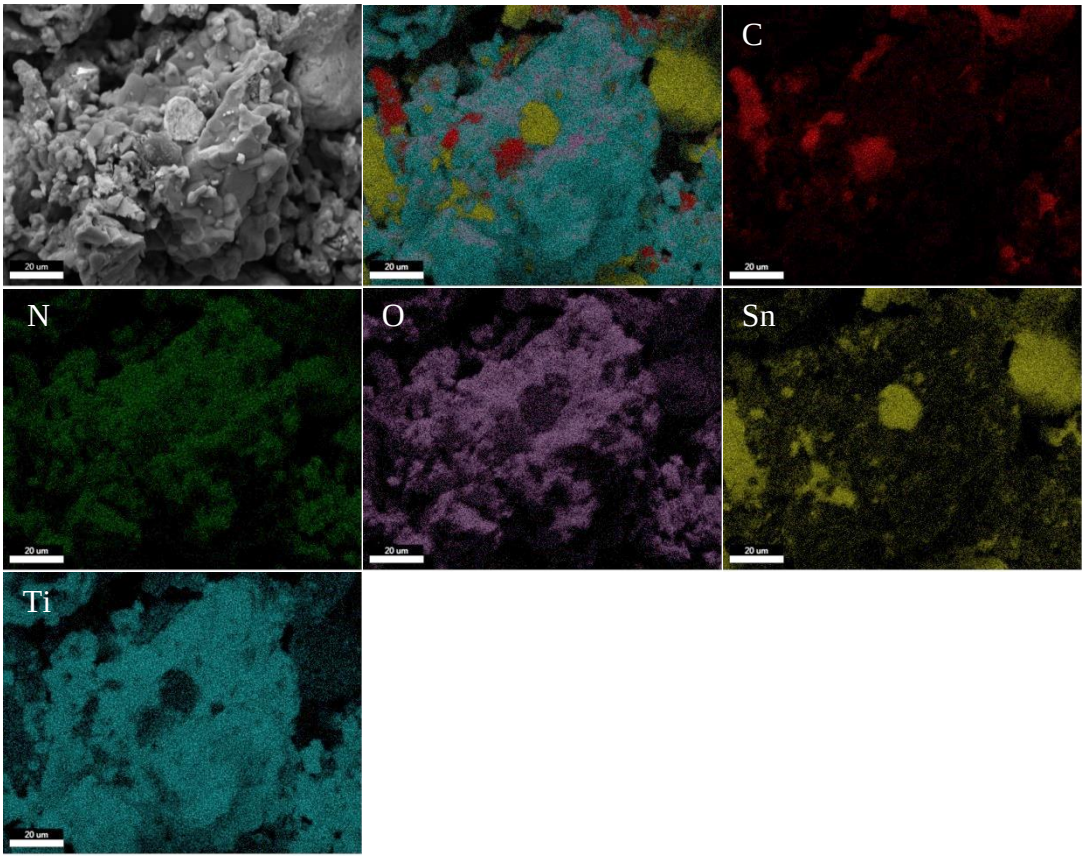

Figure 40: EDS mapping of SnO_2/TiO_2 (3:1) CVD 30-min.

Table 9: EDS mapping results of SnO_2/TiO_2 (3:1) CVD 30-min.

Element	Weight %	Atomic %	Net Int.	Error %	Kratio	Z	A	F
C K	4.82	13.28	109.20	6.12	0.0370	1.3168	0.5823	1.0000
N K	1.57	3.71	31.10	7.15	0.0124	1.2839	0.6118	1.0000
O K	21.51	44.47	296.50	9.59	0.0600	1.2551	0.2223	1.0000
SnL	27.30	7.61	303.20	3.11	0.2232	0.7726	1.0475	1.0104
TiK	44.80	30.93	673.10	3.09	0.4142	0.9641	0.9562	1.0029

Figure 41 shows the EDS mapping of the SnO_2/TiO_2 (3:1) CVD 60-min sample. The figure shows the same pattern as figure 40: Ti-heavy structures, clustering of elements, white rock-like structures of Sn, oxygen and nitrogen throughout the area, and carbon in black broken up pieces. Table 10 shows the SnO_2/TiO_2 (3:1) CVD 60-min sample to have a ratio of 24.5%:75.5% (0.98:3.02). It is worthwhile to note that the ratios from figures 40 and 41 pertain

to their specific areas only, but other areas not included in these images showed the same trend. Additionally, EDS mapping does an elemental composition of the surface of the selected areas and will be compared to the elemental compositions found in the XPS characterization.

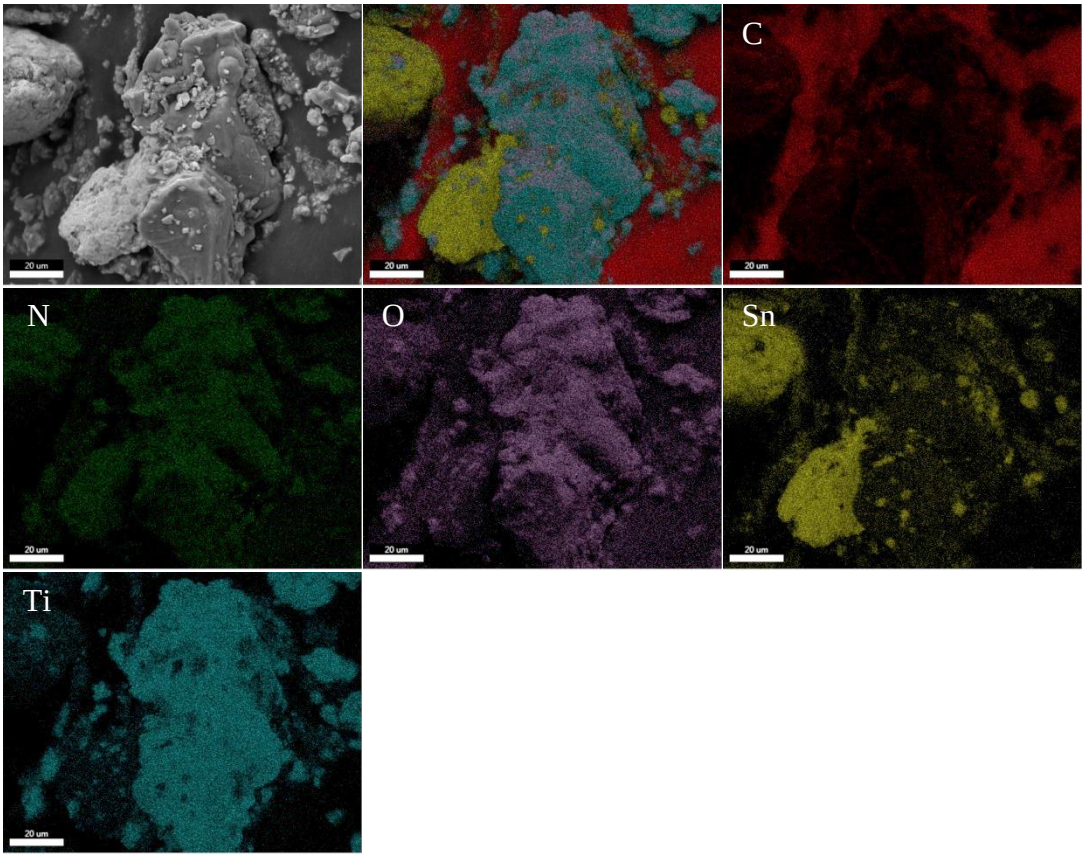

Figure 41: EDS mapping of SnO_2/TiO_2 (3:1) CVD 60-min.

Table 10: EDS mapping results for SnO_2/TiO_2 (3:1) CVD 60-min.

Element	Weight %	Atomic %	Net Int.	Error %	Kratio	Z	A	F
C K	19.16	39.61	480.50	5.19	0.1536	1.2411	0.6460	1.0000
N K	5.21	9.24	68.30	8.32	0.0256	1.2097	0.4063	1.0000
O K	19.08	29.62	277.70	9.55	0.0531	1.1822	0.2354	1.0000
SnL	25.20	5.27	279.30	3.30	0.1944	0.7252	1.0542	1.0088
TiK	31.35	16.26	471.20	3.14	0.2742	0.9040	0.9636	1.0040

To verify the results of the separation of elements in figures 40 and 41, a sample of SnO_2/TiO_2 (3:1) was heat treated to 1000 °C under argon without methane for the same amount

of time as the CVD sample (30-min). Figure 42 shows the elemental mapping of the heat-treated sample without methane gas. It shows no element separation and keeps the ratio of 77.2%:22.8% (3.1:0.9). These results conclude that the high temperature alone was not the cause of the element separation and that the cause could be the methane gas used to carbon-coat the sample.

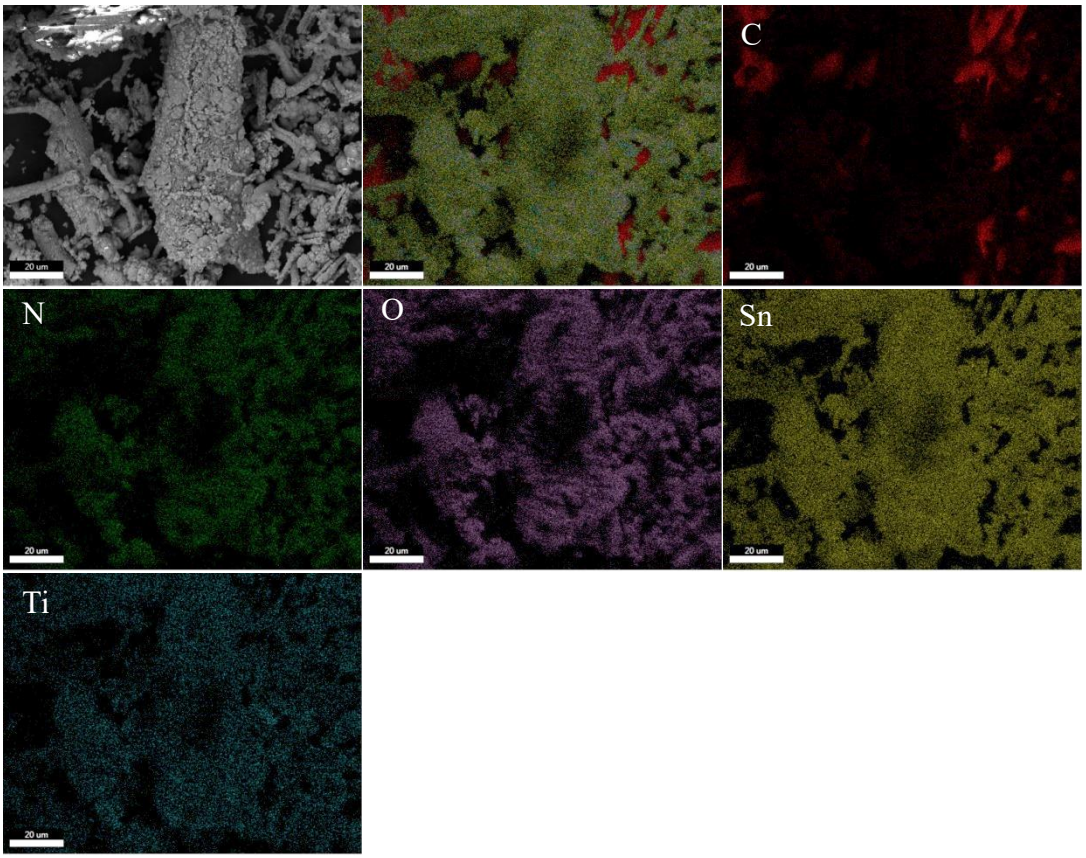

Figure 42: EDS mapping of SnO_2/TiO_2 (3:1) heat treated at 1000 °C under argon without methane.

Table 11: EDS mapping results for SnO_2/TiO_2 (3:1) heat treated at 1000 °C under argon.

Element	Weight %	Atomic %	Net Int.	Error %	Kratio	Z	A	F
C K	4.43	19.12	94.70	4.94	0.0512	1.5418	0.7499	1.0000
N K	2.25	8.34	34.80	6.23	0.0240	1.4999	0.7100	1.0000
O K	9.28	30.06	171.90	7.71	0.0638	1.4638	0.4700	1.0000
SnL	75.09	32.79	324.30	3.77	0.6672	0.8756	1.0138	1.0011
TiK	8.95	9.68	42.90	7.20	0.0945	1.1391	0.9234	1.0037

Figure 43 shows the XRD analysis for both the 30- and 60-minute samples, which appear to be very similar with respect to the major phases present. The LeBail fitting of the samples show 2 major phases present which were TiO_2 in the rutile phase and Sn as metallic tin. The reduction of the Sn from the SnO_2 may have occurred through the presence of hydrogen gas or during the carbonization process, which has been shown in the literature [82, 95, 96]. The results of the LeBail fitting are shown in table 12, which show a good agreement between the literature and fitting for the presence of both phases in the 60-minute. Due to the similarity between the phases present in the samples only one sample was fitted in figure 43 (b). The reduced $\chi 2$ of the fitting was 2.62 which shows a great agreement between the literature and the current data. The TiO_2 present in the sample was determined to be in the rutile phase, and the Sn present in the sample was in the metallic form β-Tin [78].

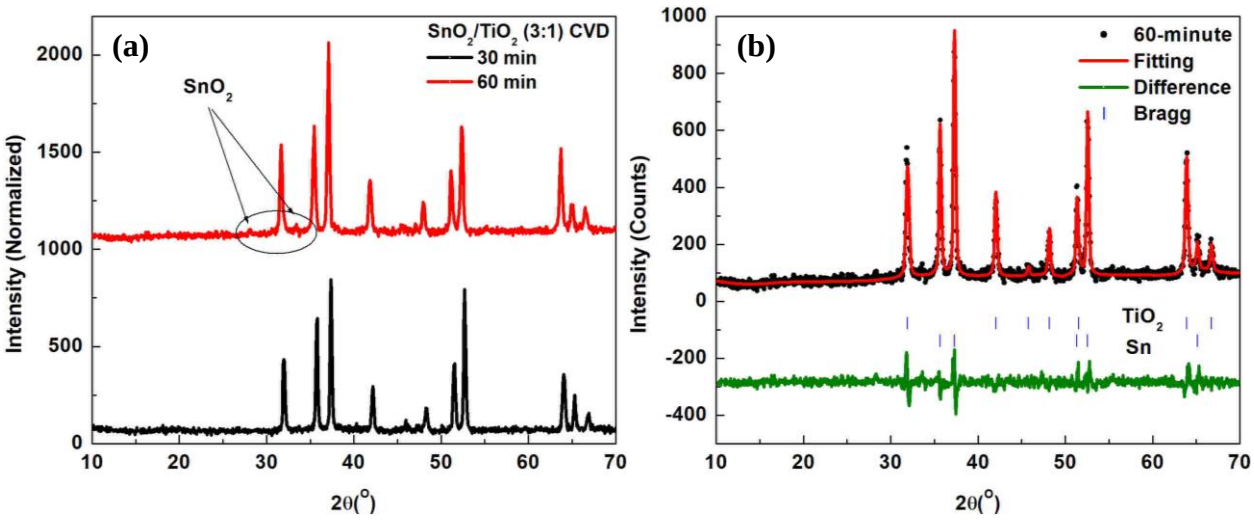

Figure 43: XRD analysis of SnO_2/TiO_2 (3:1) CVD (a) combined and (b) 60-min.

Table 12: LeBail fitting of the SnO_2/TiO_2 (3:1) CVD 30- and 60-min.

Phase	Space Group	a	b	c	α(°)	β(°)	γ(°)	χ^2
TiO_2	$P4_2/mnm$	4.603	4.603	2.969	90.0	90.0	90.0	2.62
Sn	$I4_1/amd$	5.847	5.847	3.187	90.0	90.0	90.0	

Figure 44 show both the Ti 2P XPS spectra for the 30- and 60-min samples. The samples consisted of 3 peaks, centered at 458.3, 464.5, and 471.9 eV which represent the Ti $2P_{1/2}$, Ti $2P_{3/2}$, and the Ti 2P satellite, respectively. For the 30-min sample, the intensity was not high enough to determine the surface chemistry of the sample with any degree of certainty. However, the 60-min sample showed ample signal for determination of the chemistry of the 458.4 and 459.7 eV. The peak centered at 458.4 eV is consistent with TiO_2 [97-99]. However, the peak centered at 459.7 eV is consistent with samples that have been annealed at 450 °C in hydrogen gas [97]. The energy shift has been attributed to the loss of oxygen from the sample surface [97]. The Ti $2P_{3/2}$ peak was deconvolved into two individual peaks as well, which were centered at 464.4 and 466.1 eV. The peak centered at 464.4 eV is representative of TiO_2 in the rutile phase [97-99]. The presence of the peak at 466.1 eV is representative of the process described of the Ti 2P.

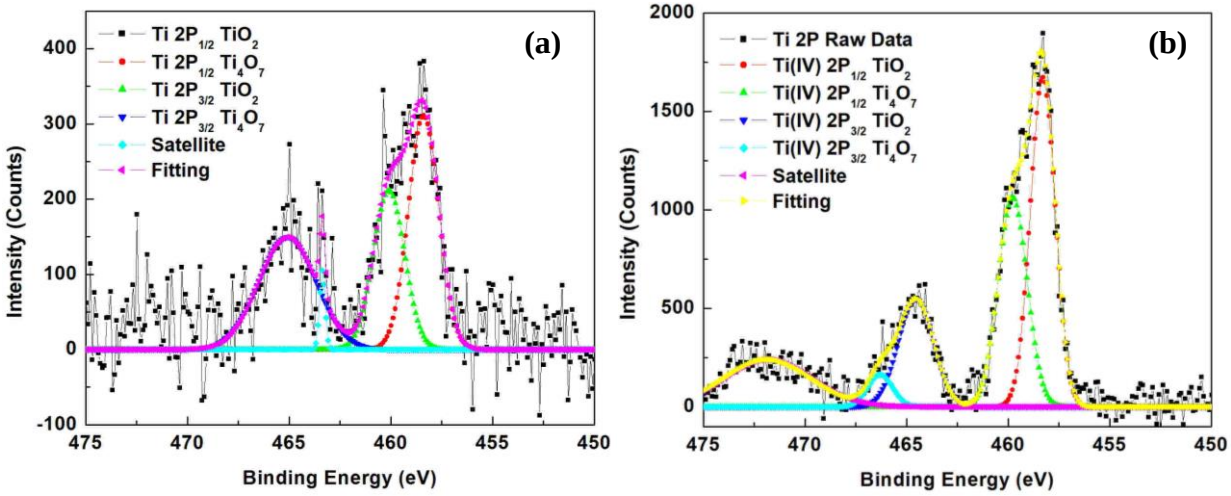

Figure 44: XPS analysis of Ti $2P_{1/2}$ and Ti $2P_{3/2}$ spectra for SnO_2/TiO_2 (3:1) CVD (a) 30- and (b) 60-min.

Figure 45 shows the Sn 3d XPS spectrum which consisted of 2 peaks located at 486.7 and 495.08 eV for both the 30- and 60-min samples. The peak at 486.7 eV represents the $Sn3d_{5/2}$ was further deconvolved into 3 component peaks, located at 484.8, 486.3, and 487.5 eV. The 3 component peaks represent the Sn in the Sn(0) metal, Sn(II)-O, and the Sn(IV)-O_2 binding environments [100-103]. Whereas the peak centered at 495.08 eV represents the $Sn3d_{3/2}$ spectra, which was deconvolved into 2 peaks, centered at 495.0 and 496.6 eV, which are representative of the $Sn3d_{3/2}$ binding environments for Sn(II)-O and the Sn(IV)-O_2 [100-103]. The Sn(0) peak was not observed due to the low intensity of the peak in the spectra. The Sn3d XPS data does appear to be contradictory to the XRD data, which showed a major phase of Sn metal and a minor oxide phase. The minor oxide phase was only observed in the 60-min samples. There is no contradiction between the data, the XPS sample of Sn(0) metal with thin oxide films show larger amounts of oxide compared to the amount of metal present. This has to do with the X-ray passing through an oxide film before hitting the reduced metal, which give the appearance of a large amount of oxide and small amount of metal present.

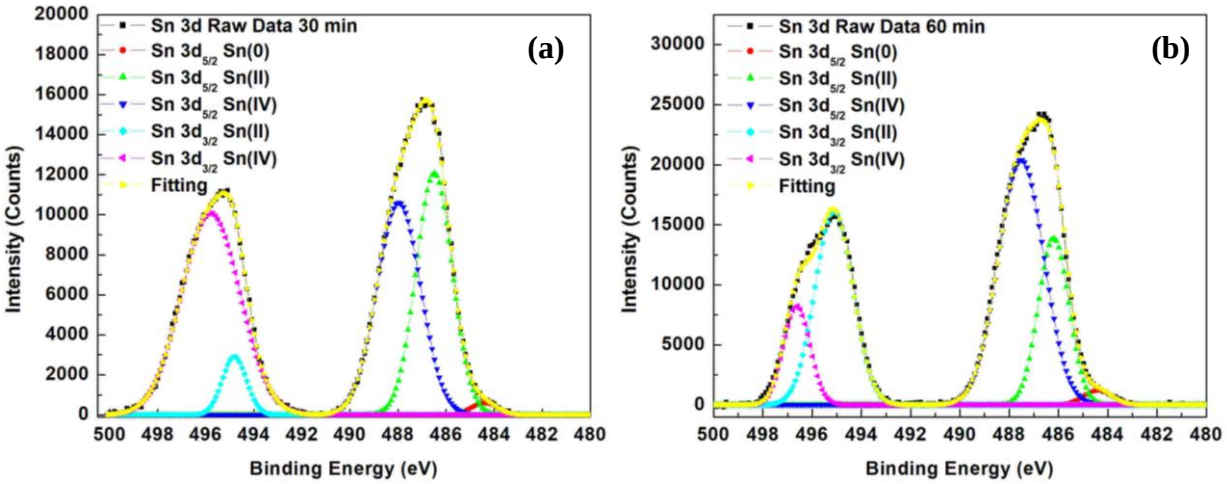

Figure 45: XPS analysis of Sn $3d_{5/2}$ and Sn $3d_{3/2}$ spectra of SnO_2/TiO_2 (3:1) CVD (a) 30- and (b) 60-min.

Figure 46 shows the C1S XPS spectrum for the 30- and 60-min samples, which show a single peak in the spectrum centered at 284.8 eV. In both samples the peak was deconvolved into 2 peaks centered at 284.2 eV and 285.8 eV, which correspond to C-C/C=C and C-O binding environments [104, 105].

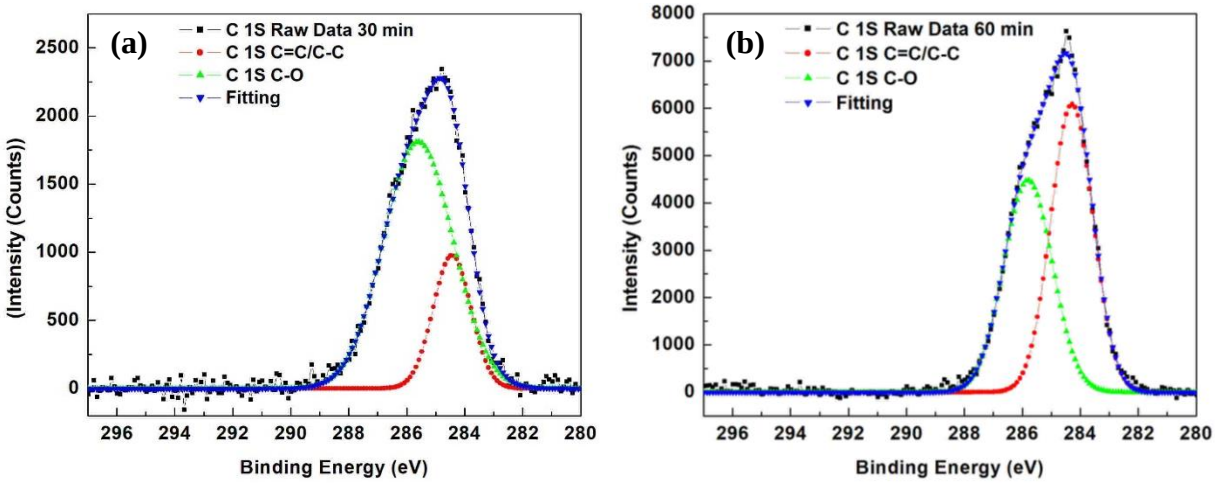

Figure 46: XPS analysis of C1S spectra for SnO_2/TiO_2 (3:1) CVD (a) 30- and (b) 60-min.

Figure 47 shows the O1S XPS spectra for the 30- and 60-min samples, which consisted of one peak centered at 531.3 eV. The peak was deconvolved into to individual peaks located at 530.0 and 531.8 eV. The peaks are representative of oxygen bound to a high oxidation state metal such as Ti or Sn with the oxygen in the 2-oxidation state and the presence of a hydroxyl species [106].

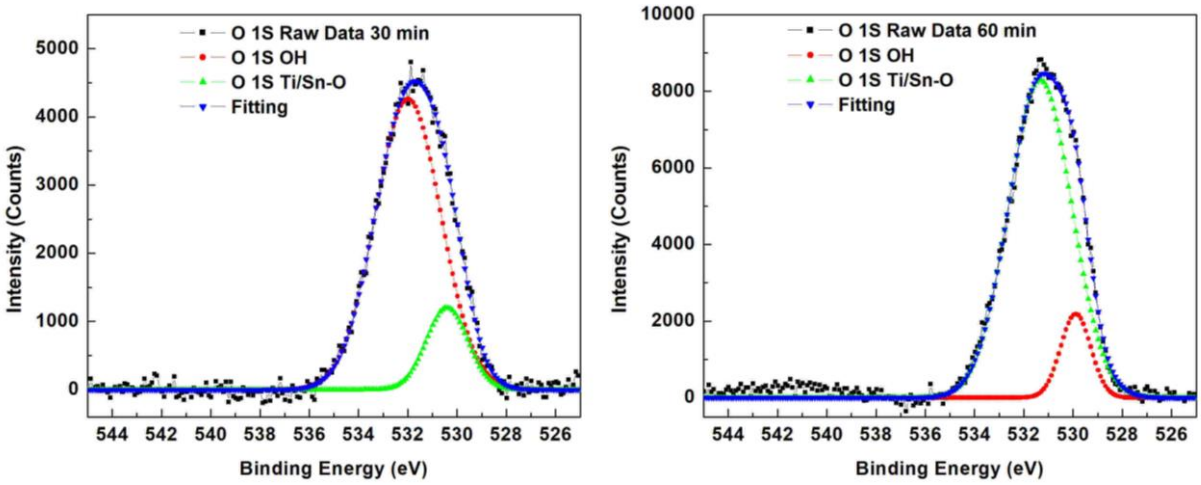

Figure 47: XPS analysis of O1S spectra for SnO_2/TiO_2 (3:1) CVD (a) 30- and (b) 60-min.

3.7 Electrochemical Performance of Coated Active Material

The electrochemical performance tests of the coated active material were conducted using the same tests and parameters as the SnO_2/TiO_2 (3:1) non-coated samples for comparison. The active materials have been named in accordance with their deposition time: CVD 0-, 30-, and 60-min, with CVD 0-min pertaining to the SnO_2/TiO_2 (3:1) data from previous sections.

3.7.1 Cycle Performance of Coated Active Material

The coated material of 30- and 60-min samples were compared to the base sample of 0-min to analyze the effects of carbon-coating by CVD on the electrochemical performance of SnO_2/TiO_2 (3:1) metal-oxide as anode material.

Figure 48 shows the cycle performance of the CVD samples of 0-, 30-, and 60-min. Figure 48 (a) shows the first cycles of the CVD samples showing that 0-min had the highest irreversible specific capacity and initial charge specific capacity with 1677 and 956 mAh g^{-1} (43.0 % loss), respectively. This is followed by 30-min with initial specific capacities of 1002 and 691 mAh g^{-1} (31.0 % loss). 60-min had the lowest initial specific capacities at 825 and 449

mAh g^{-1} (45.6 % loss). These results indicate a lower capacity from the original sample as the deposition time increases with a 40.3 % reduction in initial discharge specific capacity for 30-min and a 50.8 % reduction for 60-min. Figure 48 (b) illustrates the performances of the samples after 100 cycles and shows 30-min having the highest charge specific capacity with 653 mAh g^{-1} (after 61 cycles) followed by 60-min with 499 mAh g^{-1} and 0-min with 289 mAh g^{-1}. The CVD samples show great cycle performances with capacity retentions of 94.4% (projected to be 93.2% after 100 cycles) for the 30-min sample and 111.1% for the 60-min sample. The capacity retentions of the CVD samples are a vast improvement from the 30.3 % of the original 0-min sample and indicate that carbon-coating the sample by CVD provides better cycle performance despite initial capacity reduction. Figure 48 (c) shows the performances of the samples over each cycle. After 25 cycles, 30-min outperforms 0-min with a charge specific capacity of 652 mAh g^{-1}, and after 38 cycles 0-min's capacity fades below 60-min with a charge specific capacity of 479 mAh g^{-1}. At the end of the test the 60-min sample outperforms the 0-min sample by 210 mAh g^{-1} while the 30-min sample is projected to outperform the 0-min sample by 355 mAh g^{-1}. Figure 48 (d) shows the efficiency of each sample. The 30- and 60-min show great efficiency throughout their entire life cycle maintaining efficiencies above 99 % after the 4^{th} cycle. Before the 4^{th} cycle, the 30-min sample shows an efficiency of 69 % at the 1^{st} cycle due to the formation of the SEI layer but improves immediately to 97 % on the 2^{nd} cycle and 99 % on the 3rd cycle. Additionally, the 60-min sample shows an efficiency of 42 % at the 1^{st} cycle and improves to 95 % on the 2^{nd} cycle and 98 % on the 3^{rd} cycle. The efficiency results indicate an improvement on reversibility by the addition of carbon-coating by CVD regardless of the deposition time. Table 13 shows the previous cycle performance data.

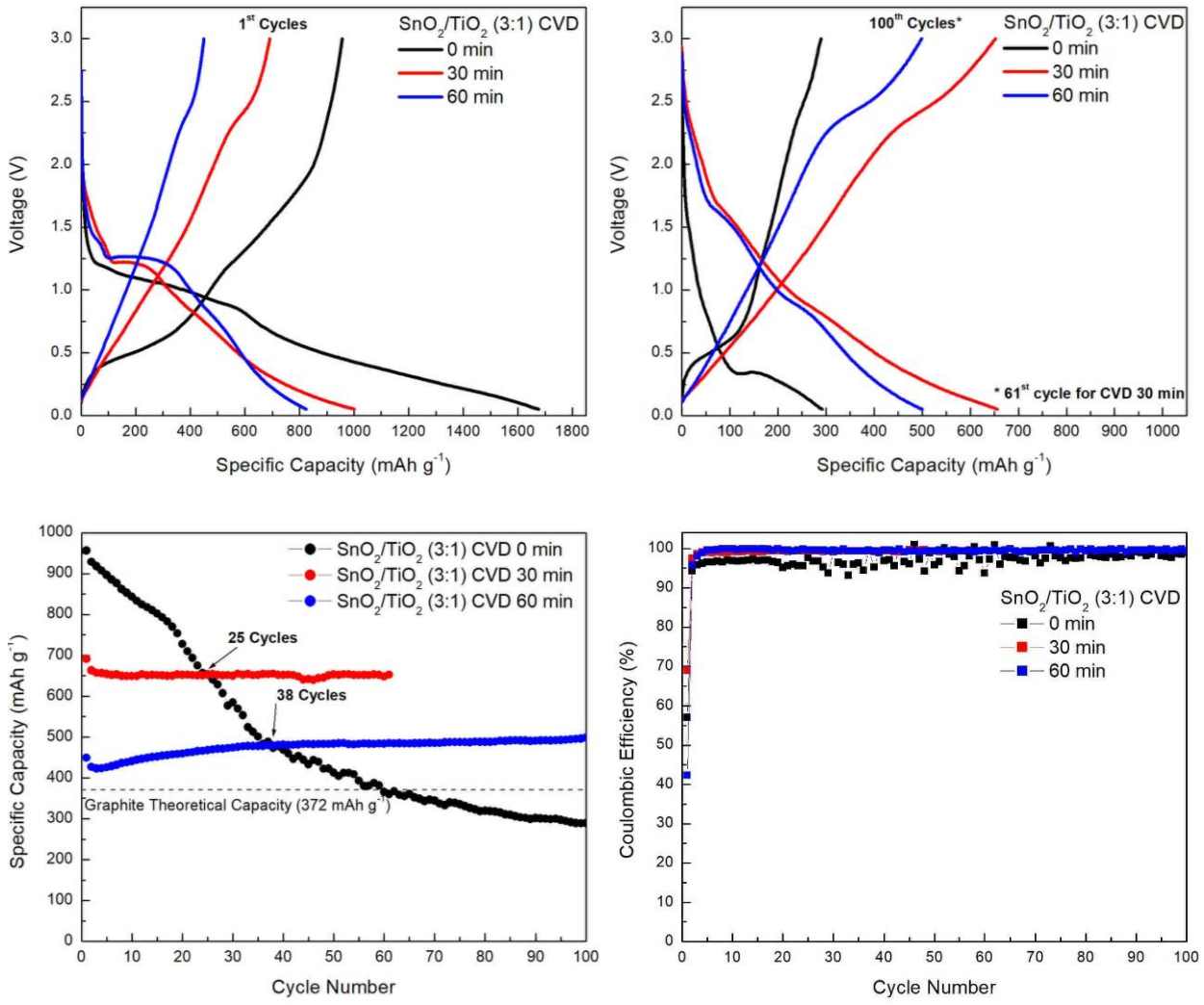

Figure 48: Charge/discharge curves of SnO_2/TiO_2 (3:1) CVD 0-, 30-, and 60-min of (a) 1st cycles and (b) 100th cycles, (c) charge specific capacity cycle performances, and (d) Coulombic efficiency over 100 cycles at a current density of 100 mA g^{-1}.

Table 13: Cycle performance of SnO_2/TiO_2 (3:1) CVD 0-, 30-, and 60-min data.

CVD Deposition Time	Initial Specific Discharge Capacity (mAh g^{-1})	Specific Charge Capacity (mAh g^{-1})		SEI Layer Capacity Loss (%)	Capacity Retention (%)
		1st Cycle	100th Cycle		
0-min	1677	956	289	43.0	30.23
30-min	1002	691	653*	31.0	94.5
60-min	825	449	499	45.6	111.1

3.7.2 Rate Performance of Coated Active Material

The rate performance for the coated active material was conducted using the current densities of 50, 100, 200, 400, 500, and 50 mA g^{-1}, and compared to the non-coated active material of 3:1 CVD 0-min. Figure 49 shows that both CVD 30- and 60-min have a stable rate performance compared to their baseline sample of CVD 0-min. However, both 30- and 60-min samples have lower initial charge specific capacities, 644 and 464 mAh g^{-1}, respectively, than the 0-min sample at 940 mAh g^{-1}. Additionally, losses throughout the current densities were lower for the 30- and 60-min sample. The 30-min sample had capacity losses of 22.0, 6.72, 1.31, 9.39, 3.23, and 5.08 % from the initial to the final charge specific capacity of each current density. Furthermore, the 60-min sample had the highest performance with capacity losses of 17.0, 4.07, 2.69, and 1.18 % from 50 to 400 mA g^{-1} and capacity gains of 0.42 and 2.01 % from 500 to 50 mA g^{-1}. The 60-min also maintained a similar charge specific capacity of 239 mAh g^{-1} to the 30-min sample of 248 mAh g^{-1} at 500 mA g^{-1}. As the current densities returned to 50 mA g^{-1}, the 30-min sample ended with a charge specific capacity of 433 to 411 mAh g^{-1} and a capacity retention of 63.8 %, while the 60-min sample finished with a charge specific capacity of 348 to 355 mAh g^{-1} and a capacity retention of 76.3 %. Compared with the 0-min sample, both the 30- and 60-min sample had more consistent rate performances and better capacity retentions as shown in table 14. Also, both samples had higher charge specific capacities at 400 and 500 mA g^{-1} than the 0-min sample. The rate performance data concludes that the addition of a carbon-coating by CVD helps by preventing, or at the very least by delaying, the pulverization of the anode compared to the non-coated active material.

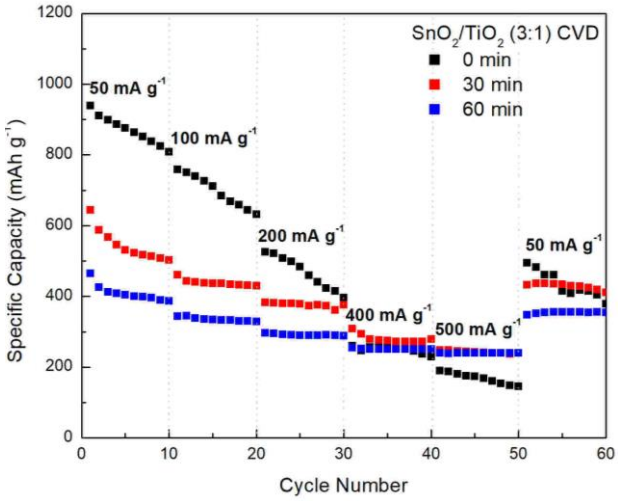

Figure 49: Rate performance data for SnO_2/TiO_2 (3:1) CVD 0-, 30-, and 60-min at current densities of 50, 100, 200, 400, 500, and 50 mA g^{-1}.

Table 14: Rate performance data for SnO_2/TiO_2 (3:1) CVD 0-, 30-, and 60-min.

CVD Deposition Time	**Initial / Final Charge Specific Capacity (mAh g^{-1}) (Capacity Gain/Loss (%))**						**Capacity Retention (%)**
	50 mA g^{-1}	**100 mA g^{-1}**	**200 mA g^{-1}**	**400 mA g^{-1}**	**500 mA g^{-1}**	**50 mA g^{-1}**	
0-min	940 / 808 (-14.0)	760 / 632 (-16.8)	526 / 397 (-24.5)	260 / 229 (-11.9)	190 / 146 (-23.2)	494 / 379 (-23.3)	40.3
30-min	644 / 502 (-22.0)	461 / 430 (-6.72)	383 / 378 (-1.31)	309 / 280 (-9.39)	248 / 240 (-3.23)	433 / 411 (-5.08)	63.8
60-min	465 / 386 (-17.0)	344 / 330 (-4.07)	297 / 289 (-2.69)	254 / 251 (-1.18)	239 / 240 (+0.42)	348 / 355 (+2.01)	76.3

3.7.3 Cyclic Voltammetry for Coated Active Material

The lithiation/de-lithiation reactions of the CVD sample anodes were studied and compared using cyclic voltammetry tests. Figure 50 shows the cyclic voltammogram of the first three cycles for SnO_2/TiO_2 (3:1) CVD (a) 0-min, (b) 30-min, and (c) 60-min, as well as (d) the first cycles of all three samples together. Figure 50 (a) shows the same results as figure 37 (c) for comparison where the cathodic peaks are at 0.05, 0.84, and 1.15 V while the anodic peaks are at

0.62, 1.29, and 1.9 V. Figure 50 (b-c) show the cathodic peaks in both 30- and 60-min samples at slightly higher voltages (lower currents) from the 0-min sample at 0.84 to 0.98 V (-1.84 to -0.83 mA) indicating the formation of the SEI layer and alloying of Li_xSn and 1.15 to 1.35 V (-0.43 to -0.1 mA) indicating the reduction of SnO_2. However, the anodic peaks are barely visible in both 30- and 60-min samples. This reaction is found in literature where the introduction of carbon to the sample causes the redox peaks to weaken [13, 47, 66]. The anodic peaks at 0.49, 0.62, and 2.5 V are for both 30- and 60-min samples indicating that the SnO_2/TiO_2 (3:1) sample is coated entirely in carbon by CVD. The 0.49 and 0.62 V peaks can be attributed to the de-lithiation of Li_xSn and reoxidation of Sn while the 2.5 V corresponds in literature to the pyrolysis of the PAN binder during the heat treatment of the slurry [107]. The subsequent cycles show overlapping signifying good cyclability and reinforces the data of both Coulombic efficiency and rate performance. Figure 50 (d) shows the 1^{st} cycles of the 0-, 30-, and 60-min samples to visually compare the redox peaks. It clearly shows the effects of the carbon-coating causes the peaks to weaken.

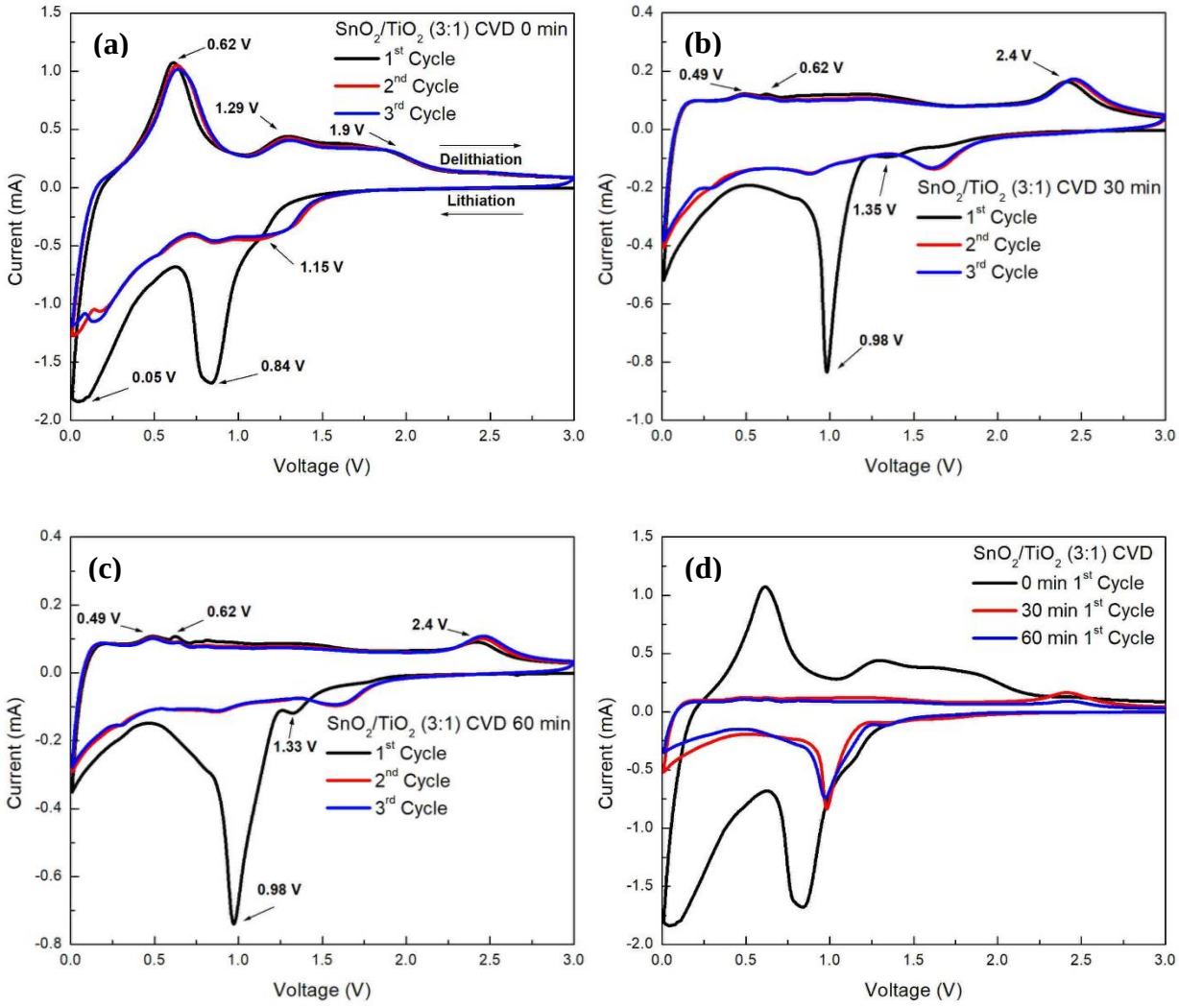

Figure 50: Cyclic voltammetry of the first three cycles for SnO_2/TiO_2 (3:1) (a) CVD 0-min, (b) 30-min, and (c) 60-min, as well as (d) the first cycles of all three samples.

3.7.4 Electrochemical Impedance Spectroscopy (EIS) of Coated Active Material

EIS tests were utilized to study the coated materail's electrochemical kinetics and compare them to the non-coated sample, 0-min. According to the results from figure 51 and table 15, the 60-min sample has the lowest Rs, solution resistance, with 2.67 Ω followed by the 0-min sample, 4.33 Ω, and the 30-min sample, 5.42 Ω. The polarization resistance, Rp, of the samples shows that the 60-min again has the lowest resistance with 91 Ω followed by 0-min, 135 Ω, and

30-min, 159 Ω. Since the 60-min sample had the lowest resistances and the 30-min sample had the highest resistance, no correlation could be made about the effect carbon-coating has on the resistance of the samples. However, figure 51 (b) show that the 30-min sample has the lowest Warburg constant, σ, with 285.86 Ω $s^{-1/2}$ signifying high Li^+ diffusion. Figures 51 (c-e) show the equivalent circuits of the 0-, 30-, and 60-min samples.

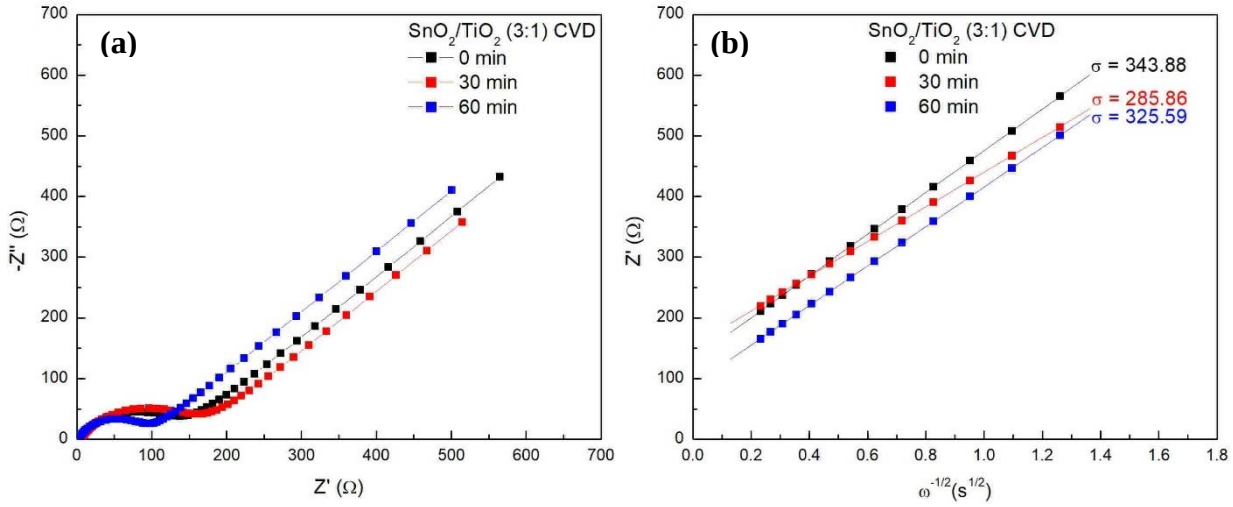

Figure 51: EIS data of (a) fitted Nyquist plot and (b) Warburg plot for SnO_2/TiO_2 (3:1) CVD 0-, 30-, and 60-min.

Table 15: Nyquist data for equivalent circuits of SnO_2/TiO_2 (3:1) CVD 0-, 30-, and 60-min.

SnO_2/TiO_2 (3:1) CVD:	**Rs (Ω)**	**Rp (Ω)**	**CPE**		**W**	**σ (Ω $s^{-0.5}$)**
			Y_0 (μMho)	**N**	**Y_0 (mMho)**	
0 min	4.33	135	22.6	0.709	2.06	343.88
30 min	5.42	159	29.1	0.693	2.49	285.86
60 min	2.67	91	13.2	0.766	2.17	325.59

CHAPTER IV

SUMMARY AND CONCLUSION

SnO_2/TiO_2 short fiber micro-belts were successfully synthesized at different Sn:Ti ratios. The micro-belt short fibers were synthesized using ethanol and PVP polymer solution with tin and titanium precursors. The magnetically stirred solutions were spun using centrifugal spinning at 9000 rpm for 2 min. Heat treatments at different ramp rates were done to the collected fibers to oxidize micro-belts. Additionally, the SnO_2/TiO_2 calcined fibers for the 3:1 ratio was selected to be carbon-coated by CVD based on its performance as active material in anodes for Li-ion batteries against the other ratios. The morphology, elemental composition, and thermal degradation of the fibers and carbon-coated materials were studied using SEM, EDS, and TGA analysis. Furthermore, the crystal structure was analyzed with XRD and XPS spectroscopies which concluded that the SnO_2 and the TiO_2 from the pristine and calcined fibers were in their rutile phases. On the other hand, the carbon-coated active material showed that the SnO_2 material had been reduced to Sn(0). When the active material was tested for its performance, the 3:1 composite ratio showed an irreversible capacity of 1677 mAh g^{-1} and a reversible capacity starting at 956 mAh $g^{-1}$when tested at a constant current density of 100 mA g^{-1}. After many charge/discharge cycles, the capacity of the 3:1 ratio decayed and resulted in a capacity retention of 30.2%. However, when the 3:1 ratio was carbon-coated for 30- and 60-min its performance

showed lower irreversible capacities of 1002 and 825 mAh g^{-1} and a reversible capacity of 691 and 449 mAh g^{-1}, respectively. Although these initial capacities were 40 to 51 % lower than the non-coated material, their capacity retention after 100 cycles was improved from 30.2% of the non-coated material to 94.5% for the 30-min sample (after 61 cycles) and 111% for the 60-min sample while maintain an efficiency above 98% throughout their life cycles. Additionally, when the current density was increased to 500 mA g^{-1}, the capacities of both 30- and 60-min samples were higher than the 0-min sample. After returning the current density back to 50 mA g^{-1}, the final capacities were along the same levels for all samples with 379 mA g^{-1} for the 3:1 sample, 411 mA g^{-1} for the 30-min sample, and 355 mA g^{-1} for the 60-min sample. Overall, the effects of the carbon-coating by CVD showed lower initial capacities relative to its non-coated material, but a higher capacity retention after 100 cycles.

The use of carbon-coating by method of chemical vapor deposition showed great promise for the future Li-ion batteries, but it is important that further work be completed to solidifying its potential. Such works include the performing CVD on different ratios other than 3:1 to analyze its effects on different ratios of Sn:Ti as well performing the deposition time for different intervals such as 15- and 90-min. Other works also include studying the effects of methane on the active material to conclude the effects it has on element separation on the composite fibers. Furthermore, an important experiment to study is using acetylene as the reactive precursor for CVD as opposed to methane. Finally, the batteries included in these experiments are still running for 500 cycles and the data for the entire life cycle needs to be analyzed to have a complete understanding of the effects of carbon-coating by CVD on the electrochemical performance of metal oxide anodes for Li-ion batteries.

REFERENCES

1. Scrosati, B. and J. Garche, *Lithium batteries: Status, prospects and future.* Journal of Power Sources, 2010. **195**(9): p. 2419-2430.

2. Manthiram, A., *Materials Challenges and Opportunities of Lithium Ion Batteries.* Journal of Physical Chemistry Letters, 2011. **2**(3): p. 176-184.

3. Akhilash, M., et al., *A journey through layered cathode materials for lithium ion cells - From lithium cobalt oxide to lithium-rich transition metal oxides.* Journal of Alloys and Compounds, 2021. **869**.

4. Mekonnen, Y., A. Sundararajan, and A.I. Sarwat, *A Review of Cathode and Anode Materials for Lithium-Ion Batteries.* Southeastcon 2016, 2016.

5. Ammundsen, B. and J. Paulsen, *Novel lithium-ion cathode materials based on layered manganese oxides.* Advanced Materials, 2001. **13**(12-13): p. 943-+.

6. Li, J.L., C. Daniel, and D. Wood, *Materials processing for lithium-ion batteries.* Journal of Power Sources, 2011. **196**(5): p. 2452-2460.

7. Wu, Y.P., E. Rahm, and R. Holze, *Carbon anode materials for lithium ion batteries.* Journal of Power Sources, 2003. **114**(2): p. 228-236.

8. Evarts, E.C., *Lithium batteries To the limits of lithium.* Nature, 2015. **526**(7575): p. S93-S95.

9. Azam, M.A., et al., *Recent advances of silicon, carbon composites and tin oxide as new anode materials for lithium-ion battery: A comprehensive review.* Journal of Energy Storage, 2021. **33**.

10. Li, H.Y., et al., *Circumventing huge volume strain in alloy anodes of lithium batteries.* Nature Communications, 2020. **11**(1).

11. Chan, C.K., et al., *High-performance lithium battery anodes using silicon nanowires.* Nature Nanotechnology, 2008. **3**(1): p. 31-35.

12. Szczech, J.R. and S. Jin, *Nanostructured silicon for high capacity lithium battery anodes.* Energy & Environmental Science, 2011. **4**(1): p. 56-72.

13. Tzeng, Y., et al., *Effects of In Situ Graphitic Nanocarbon Coatings on Cycling Performance of Silicon-Flake-Based Anode of Lithium Ion Battery.* Coatings, 2021. **11**(2).

14. Ying, H.J. and W.Q. Han, *Metallic Sn-Based Anode Materials: Application in High-Performance Lithium-Ion and Sodium-Ion Batteries.* Advanced Science, 2017. **4**(11).

15. Li, W.H., X.L. Sun, and Y. Yu, *Si-, Ge-, Sn-Based Anode Materials for Lithium-Ion Batteries: From Structure Design to Electrochemical Performance.* Small Methods, 2017. **1**(3).

16. Wang, Y., et al., *Sn@CNT and Sn@C@CNT nanostructures for superior reversible lithium ion storage.* Chemistry of Materials, 2009. **21**(14): p. 3210-3215.

17. Lu, Y., et al., *Centrifugally Spun SnO2 Microfibers Composed of Interconnected Nanoparticles as the Anode in Sodium-Ion Batteries.* Chemelectrochem, 2015. **2**(12): p. 1947-1956.

18. Chen, J.S. and X.W. Lou, *SnO2-Based Nanomaterials: Synthesis and Application in Lithium-Ion Batteries.* Small, 2013. **9**(11): p. 1877-1893.

19. Zoller, F., et al., *Tin Oxide Based Nanomaterials and Their Application as Anodes in Lithium-Ion Batteries and Beyond.* Chemsuschem, 2019. **12**(18): p. 4140-4159.

20. Mukherjee, R., et al., *Photothermally Reduced Graphene as High-Power Anodes for Lithium-Ion Batteries.* Acs Nano, 2012. **6**(9): p. 7867-7878.

21. Bhardwaj, T., et al., *Enhanced Electrochemical Lithium Storage by Graphene Nanoribbons.* Journal of the American Chemical Society, 2010. **132**(36): p. 12556-12558.

22. Yoo, E., et al., *Large reversible Li storage of graphene nanosheet families for use in rechargeable lithium ion batteries.* Nano Letters, 2008. **8**(8): p. 2277-2282.

23. Abouimrane, A., et al., *Non-Annealed Graphene Paper as a Binder-Free Anode for Lithium-Ion Batteries.* Journal of Physical Chemistry C, 2010. **114**(29): p. 12800-12804.

24. Zhang, Y., L.Y. Zhang, and C.W. Zhou, *Review of Chemical Vapor Deposition of Graphene and Related Applications.* Accounts of Chemical Research, 2013. **46**(10): p. 2329-2339.

25. Fan, Z.J., et al., *Nanographene-Constructed Carbon Nanofibers Grown on Graphene Sheets by Chemical Vapor Deposition: High-Performance Anode Materials for Lithium Ion Batteries.* Acs Nano, 2011. **5**(4): p. 2787-2794.

26. Ning, G.Q., et al., *Chemical vapor deposition derived flexible graphene paper and its application as high performance anodes for lithium rechargeable batteries.* Journal of Materials Chemistry A, 2013. **1**(2): p. 408-414.

27. Li, X.M., et al., *Directly Drawing Self-Assembled, Porous, and Monolithic Graphene Fiber from Chemical Vapor Deposition Grown Graphene Film and Its Electrochemical Properties.* Langmuir, 2011. **27**(19): p. 12164-12171.

28. Cai, L. and G. Yu, *Recent Advances in Growth and Modification of Graphene-Based Energy Materials: From Chemical Vapor Deposition to Reduction of Graphene Oxide.* Small Methods, 2019. **3**(7).

29. Toriello, M., et al., *Progress on the Fabrication and Application of Electrospun Nanofiber Composites.* Membranes, 2020. **10**(9).

30. Eatemadi, A., et al., *Nanofiber: Synthesis and biomedical applications.* Artificial Cells Nanomedicine and Biotechnology, 2016. **44**(1): p. 111-121.

31. Chavez, R.O., T.P. Lodge, and M. Alcoutlabi, *Recent developments in centrifugally spun composite fibers and their performance as anode materials for lithium-ion and sodium-ion batteries.* Materials Science and Engineering B-Advanced Functional Solid-State Materials, 2021. **266**.

32. Ayala, J., et al., *Performance and morphology of centrifugally spun Co3O4/C composite fibers for anode materials in lithium-ion batteries.* Journal of Materials Science, 2021. **56**(28): p. 16010-16027.

33. Lopez, J., et al., *Centrifugally spun TiO2/C composite fibers prepared from TiS2/PAN precursor fibers as binder-free anodes for LIBS.* Journal of Physics and Chemistry of Solids, 2021. **149**.

34. Agubra, V.A., et al., *Forcespinning: A new method for the mass production of Sn/C composite nanofiber anodes for lithium ion batteries.* Solid State Ionics, 2016. **286**: p. 72-82.

35. Zuniga, L., et al., *Multichannel hollow structure for improved electrochemical performance of TiO2/Carbon composite nanofibers as anodes for lithium ion batteries.* Journal of Alloys and Compounds, 2016. **686**: p. 733-743.

36. Weitz, R.T., et al., *Polymer nanofibers via nozzle-free centrifugal spinning.* Nano Letters, 2008. **8**(4): p. 1187-1191.

37. Chen, H.S. and C.E. Miller, *Centrifugal Spinning of Metallic Glass Filaments.* Materials Research Bulletin, 1976. **11**(1): p. 49-54.

38. Gunn, J. and M.Q. Zhang, *Polyblend nanofibers for biomedical applications: perspectives and challenges.* Trends in Biotechnology, 2010. **28**(4): p. 189-197.

39. Wei, X.Z., et al., *Characterization and application of a thin-film composite nanofiltration hollow fiber membrane for dye desalination and concentration.* Chemical Engineering Journal, 2013. **223**: p. 172-182.

40. Wang, X.H., et al., *Enhanced gas sensing property of SnO2 nanoparticles by constructing the SnO2-TiO2 nanobelt heterostructure.* Journal of Alloys and Compounds, 2015. **639**: p. 571-576.

41. Chen, G., et al., *High-Energy Faceted SnO(2)-Coated TiO(2) Nanobelt Heterostructure for Near-Ambient Temperature-Responsive Ethanol Sensor.* ACS Appl Mater Interfaces, 2015. **7**(44): p. 24950-6.

42. Zhao, Z., et al., *Structure, synthesis, and applications of TiO2 nanobelts.* Adv Mater, 2015. **27**(16): p. 2557-82.

43. Zeng, W., T. Liu, and Z. Wang, *Enhanced gas sensing properties by SnO2 nanosphere functionalized TiO2 nanobelts.* Journal of Materials Chemistry, 2012. **22**(8).

44. Hassan, M.F., et al., *Carbon-coated MoO3 nanobelts as anode materials for lithium-ion batteries.* Journal of Power Sources, 2010. **195**(8): p. 2372-2376.

45. Zheng, F.C., et al., *Facile fabrication of highly porous Co3O4 nanobelts as anode materials for lithium-ion batteries.* Rsc Advances, 2016. **6**(12): p. 9640-9646.

46. Mai, L.Q., et al., *Lithiated MoO3 Nanobelts with Greatly Improved Performance for Lithium Batteries.* Advanced Materials, 2007. **19**(21): p. 3712-3716.

47. Tian, Q., et al., *Facile fabrication of robust TiO 2 @SnO 2 @C hollow nanobelts for outstanding lithium storage.* Journal of Power Sources, 2018. **376**: p. 1-10.

48. Gonzalez, G., et al., *Synthesis of SnO2/TiO2 micro belt fibers from polymer composite precursors and their applications in Li-ion batteries.* Polymer Engineering and Science, 2022. **62**(2): p. 360-372.

49. Zhou, W., et al., *Ag2O/TiO2 nanobelts heterostructure with enhanced ultraviolet and visible photocatalytic activity.* ACS Appl Mater Interfaces, 2010. **2**(8): p. 2385-92.

50. Wang, Y., et al., *Nanostructured Sheets of Ti□O Nanobelts for Gas Sensing and Antibacterial Applications.* Advanced Functional Materials, 2008. **18**(7): p. 1131-1137.

51. Zheng, F.L., et al., *Synthesis of hierarchical rippled Bi(2)O(3) nanobelts for supercapacitor applications.* Chem Commun (Camb), 2010. **46**(27): p. 5021-3.

52. Wang, C.X., et al., *Metal Oxide Gas Sensors: Sensitivity and Influencing Factors.* Sensors, 2010. **10**(3): p. 2088-2106.

53. Nguyen, V.D., et al., *Mixed SnO2/TiO2 included with carbon nanotubes for gas-sensing application.* Physica E-Low-Dimensional Systems & Nanostructures, 2008. **41**(2): p. 258-263.

54. Arora, P. and Z.M. Zhang, *Battery separators.* Chemical Reviews, 2004. **104**(10): p. 4419-4462.

55. Lautenschlaeger, M.P., et al., *Understanding Electrolyte Filling of Lithium-Ion Battery Electrodes on the Pore Scale Using the Lattice Boltzmann Method.* Batteries & Supercaps, 2022. **5**(7).

56. Balakrishnan, P.G., R. Ramesh, and T.P. Kumar, *Safety mechanisms in lithium-ion batteries.* Journal of Power Sources, 2006. **155**(2): p. 401-414.

57. Ali, Y., N. Iqbal, and S. Lee, *Role of SEI layer growth in fracture probability in lithium-ion battery electrodes.* International Journal of Energy Research, 2021. **45**(4): p. 5293-5308.

58. Wang, A.P., et al., *Review on modeling of the anode solid electrolyte interphase (SEI) for lithium-ion batteries.* Npj Computational Materials, 2018. **4**.

59. Kim, K.H., et al., *A key strategy to form a LiF-based SEI layer for a lithium-ion battery anode with enhanced cycling stability by introducing a semi-ionic C-F bond.* Journal of Industrial and Engineering Chemistry, 2021. **99**: p. 48-54.

60. An, S.J., et al., *The state of understanding of the lithium-ion-battery graphite solid electrolyte interphase (SEI) and its relationship to formation cycling.* Carbon, 2016. **105**: p. 52-76.

61. Nzereogu, P.U., et al., *Anode materials for lithium-ion batteries: A review.* Applied Surface Science Advances, 2022. **9**.

62. Ohzuku, T., Y. Iwakoshi, and K. Sawai, *Formation of Lithium-Graphite Intercalation Compounds in Nonaqueous Electrolytes and Their Application as a Negative Electrode for a Lithium Ion (Shuttlecock) Cell.* Journal of the Electrochemical Society, 1993. **140**(9): p. 2490-2498.

63. Masse, R.C., et al., *Energy storage through intercalation reactions: electrodes for rechargeable batteries.* National Science Review, 2017. **4**(1): p. 26-53.

64. Laresgoiti, I., et al., *Modeling mechanical degradation in lithium ion batteries during cycling: Solid electrolyte interphase fracture.* Journal of Power Sources, 2015. **300**: p. 112-122.

65. Yang, N., et al., *Stable and conductive carbon networks enabling high-performance silicon anodes for lithium-ion batteries.* Cell Reports Physical Science, 2022. **3**(5).

66. Zhao, W.C., et al., *Multi-shelled Hollow Nanospheres of SnO2/Sn@TiO2@C Composite as High-performance Anode for Lithium-Ion Batteries.* Chemelectrochem, 2021. **8**(17): p. 3282-3293.

67. Subasi, Y., et al., *Surface modified TiO2/reduced graphite oxide nanocomposite anodes for lithium ion batteries.* Journal of Solid State Electrochemistry, 2020. **24**(5): p. 1085-1093.

68. Madian, M., A. Eychmuller, and L. Giebeler, *Current Advances in TiO2-Based Nanostructure Electrodes for High Performance Lithium Ion Batteries.* Batteries-Basel, 2018. **4**(1).

69. Liang, C., et al., *Lithium alloys and metal oxides as high-capacity anode materials for lithium-ion batteries.* Journal of Alloys and Compounds, 2013. **575**: p. 246-256.

70. Liu, Y. and Y.F. Yang, *Recent Progress of TiO2-Based Anodes for Li Ion Batteries.* Journal of Nanomaterials, 2016. **2016**.

71. Chen, Z.H., et al., *Titanium-Based Anode Materials for Safe Lithium-Ion Batteries.* Advanced Functional Materials, 2013. **23**(8): p. 959-969.

72. Mou, H.Y., et al., *Encapsulating homogenous ultra-fine SnO2/TiO2 particles into carbon nanofibers through electrospinning as high-performance anodes for lithium-ion batteries.* Ceramics International, 2021. **47**(14): p. 19945-19954.

73. Song, C. and X.T. Dong, *Synthesis and formation mechanism of TiO2/SnO2 composite nanobelts by electrospinning.* Optoelectronics and Advanced Materials-Rapid Communications, 2011. **5**(12): p. 1296-1300.

74. Brutti, S., et al., *TiO2-(B) Nanotubes as Anodes for Lithium Batteries: Origin and Mitigation of Irreversible Capacity.* Advanced Energy Materials, 2012. **2**(3): p. 322-327.

75. Ramya, C.S., et al., *Vibrational and impedance spectroscopic study on PVP-NH4SCN based polymer electrolytes.* Physica B-Condensed Matter, 2007. **393**(1-2): p. 11-17.

76. Swope, R.J., J.R. Smyth, and A.C. Larson, *H in Rutile-Type Compounds .1. Single-Crystal Neutron and X-Ray-Diffraction Study of H in Rutile.* American Mineralogist, 1995. **80**(5-6): p. 448-453.

77. Meagher, E.P. and G.A. Lager, *POLYHEDRAL THERMAL EXPANSION IN THE TiO2 POLYMORPHS: REFINEMENT OF THE CRYSTAL STRUCTURES OF RUTILE AND BROOKITE AT HIGH TEMPERATURE.* Canadian Mineralogist, 1979. **17**: p. 77-85.

78. Baur, W.H. and A.A. Khan, *Rutile-Type Compounds .4. Sio2, Geo2 and a Comparison with Other Rutile-Type Structures.* Acta Crystallographica Section B-Structural Crystallography and Crystal Chemistry, 1971. **B 27**(Nov15): p. 2133-&.

79. Baur, W.H., *Uber Die Verfeinerung Der Kristallstrukturbestimmung Einiger Vertreter Des Rutiltyps - Tio2, Sno2, Geo2 Und Mgf2.* Acta Crystallographica, 1956. **9**(5): p. 515-520.

80. Toloman, D., et al., *Photocatalytic activity of SnO2-TiO2 composite nanoparticles modified with PVP.* Journal of Colloid and Interface Science, 2019. **542**: p. 296-307.

81. Huy, T.H., et al., *SnO2/TiO2 nanotube heterojunction: The first investigation of NO degradation by visible light-driven photocatalysis.* Chemosphere, 2019. **215**: p. 323-332.

82. Kwoka, M., et al., *XPS study of the surface chemistry of L-CVD SnO2 thin films after oxidation.* Thin Solid Films, 2005. **490**(1): p. 36-42.

83. Shi, H.M., et al., *Highly porous SnO2/TiO2 electrospun nanofibers with high photocatalytic activities.* Ceramics International, 2014. **40**(7): p. 10383-10393.

84. Agrawal, G. and S.K. Samal, *Raman Spectroscopy for Advanced Polymeric Biomaterials.* Acs Biomaterials Science & Engineering, 2018. **4**(4): p. 1285-1299.

85. de Faria, D.L.A., H.A.C. Gil, and A.A.A. de Queiroz, *The interaction between polyvinylpyrrolidone and I-2 as probed by Raman spectroscopy.* Journal of Molecular Structure, 1999. **478**(1-3): p. 93-98.

86. Secundino-Sanchez, O., et al., *Structural and optical characterization of the crystalline phase transformation of electrospinning TiO2 nanofibres by high temperatures annealing.* Revista Mexicana De Fisica, 2019. **65**(5): p. 459-467.

87. Leonardy, A., et al., *Structural Features of SnO2 Nanowires and Raman Spectroscopy Analysis.* Crystal Growth & Design, 2009. **9**(9): p. 3958-3963.

88. Lin, Z., et al., *Convenient fabrication of a core-shell Sn@TiO(2) anode for lithium storage from tinplate electroplating sludge.* Chem Commun (Camb), 2020. **56**(70): p. 10187-10190.

89. Yu, X.Y., et al., *Rutile TiO2 Submicroboxes with Superior Lithium Storage Properties.* Angewandte Chemie-International Edition, 2015. **54**(13): p. 4001-4004.

90. Marinaro, M., et al., *Low temperature behaviour of TiO2 rutile as negative electrode material for lithium-ion batteries.* Journal of Power Sources, 2011. **196**(22): p. 9825-9829.

91. Li, R., et al., *Sphere-like SnO2/TiO2 composites as high-performance anodes for lithium ion batteries.* Ceramics International, 2019. **45**(10): p. 13530-13535.

92. Choi, W., et al., *Modeling and Applications of Electrochemical Impedance Spectroscopy (EIS) for Lithium-ion Batteries.* Journal of Electrochemical Science and Technology, 2020. **11**(1).

93. Chang, B.Y., *The Effective Capacitance of a Constant Phase Element with Resistors in Series.* Journal of Electrochemical Science and Technology, 2022. **13**(4): p. 479-485.

94. Lee, Y.S. and K.S. Ryu, *Study of the lithium diffusion properties and high rate performance of TiNb6O17 as an anode in lithium secondary battery.* Scientific Reports, 2017. **7**.

95. Kim, B.-S., et al., *Reduction of SnO₂ with Hydrogen.* MATERIALS TRANSACTIONS, 2011. **52**(9): p. 1814-1817.

96. Ha, H., et al., *Design of Reduction Process of SnO2 by CH4 for Efficient Sn Recovery.* Scientific Reports, 2017. **7**(1).

97. Potlog, T., et al., *XRD and XPS analysis of TiO2 thin films annealed in different environments.* Journal of Materials Science and Engineering. B, 2014. **4**(6B).

98. Zheng, J., et al., *Facile Aluminum Reduction Synthesis of Blue TiO2 with Oxygen Deficiency for Lithium-Ion Batteries (vol 21, pg 18309, 2015).* Chemistry-a European Journal, 2016. **22**(22): p. 7316-7316.

99. Meng, C.L., et al., *Efficient electrochemical oxidation of COVID-19 treatment drugs favipiravir by a novel flow-through Ti/TiO2-NTA/Ti4O7 anode.* Electrochimica Acta, 2022. **430**.

100. Lu, F., et al., *Room temperature ionic liquid assisted well-dispersed core-shell tin nanoparticles through cathodic corrosion.* Rsc Advances, 2013. **3**(41): p. 18791-18793.

101. Yang, Y.C., et al., *Fabrication of pompon-like and flower-like SnO microspheres comprised of layered nanoflakes by anodic electrocrystallization.* Electrochimica Acta, 2012. **72**: p. 94-100.

102. You, H.J., et al., *Gold nanoparticle doped hollow SnO2 supersymmetric nanostructures for improved photocatalysis (vol 1, pg 4097, 2013).* Journal of Materials Chemistry A, 2013. **1**(48): p. 15558-15558.

103. Song, H.J., et al., *Graphene sheets decorated with SnO2 nanoparticles: in situ synthesis and highly efficient materials for cataluminescence gas sensors.* Journal of Materials Chemistry, 2011. **21**(16): p. 5972-5977.

104. Chen, X.N., X.H. Wang, and D. Fang, *A review on C1s XPS-spectra for some kinds of carbon materials.* Fullerenes Nanotubes and Carbon Nanostructures, 2020. **28**(12): p. 1048-1058.

105. Ranganathan, K., et al., *Study of photoelectrochemical water splitting using composite films based on TiO2 nanoparticles and nitrogen or boron doped hollow carbon spheres as photoanodes.* Journal of Molecular Catalysis a-Chemical, 2016. **422**: p. 165-174.

106. Erdem, B., et al., *XPS and FTIR surface characterization of TiO2 particles used in polymer encapsulation.* Langmuir, 2001. **17**(9): p. 2664-2669.

107. Zhang, C.Q., et al., *A binder-free Si-based anode for Li-ion batteries.* Rsc Advances, 2015. **5**(21): p. 15940-15943.

APPENDIX

APPENDIX

SUPPLEMENTAL INFORMATION

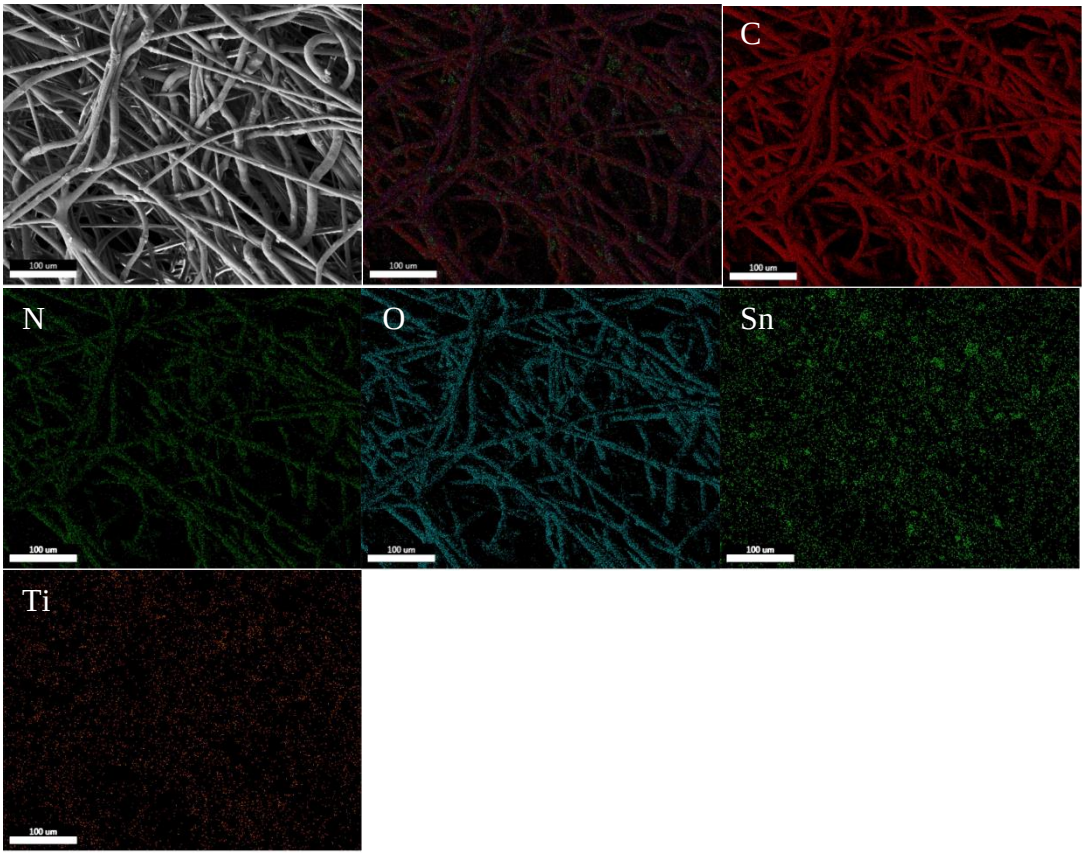

Figure 52: EDS mapping of SnO_2/TiO_2 PVP fibers (2:1).

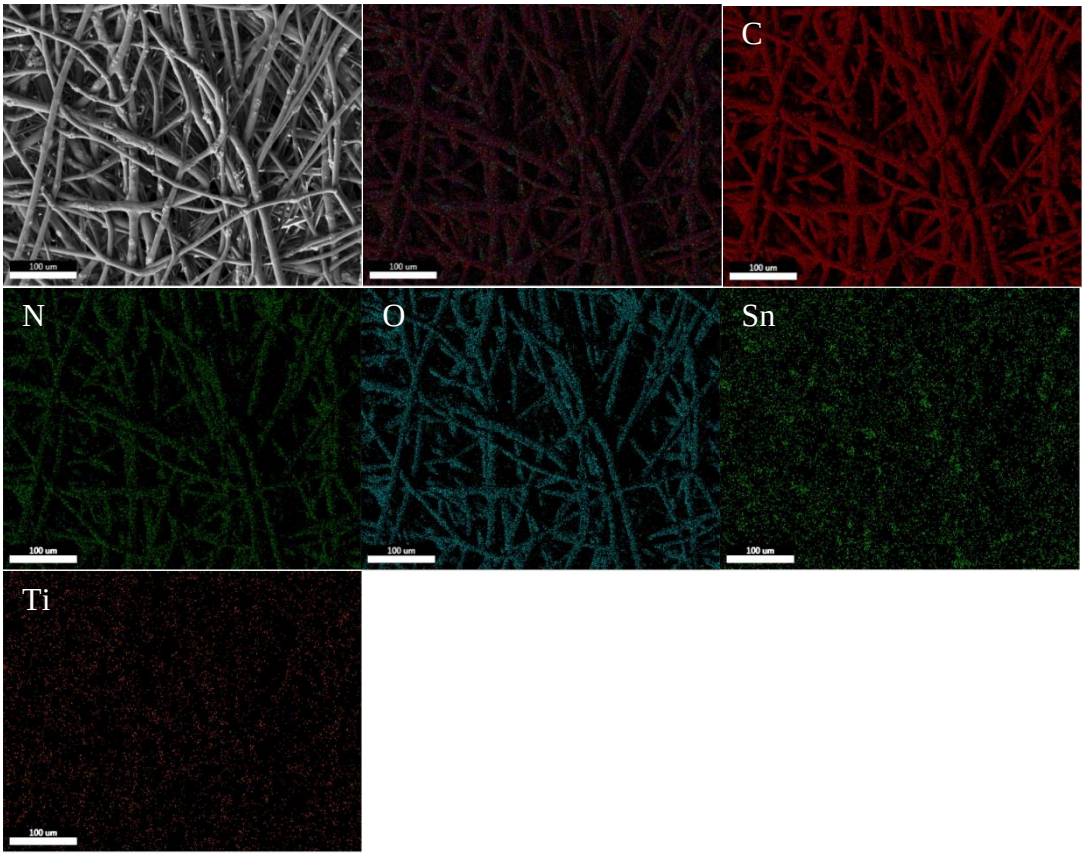

Figure 53: EDS mapping of SnO_2/TiO_2 PVP fibers (3:1).

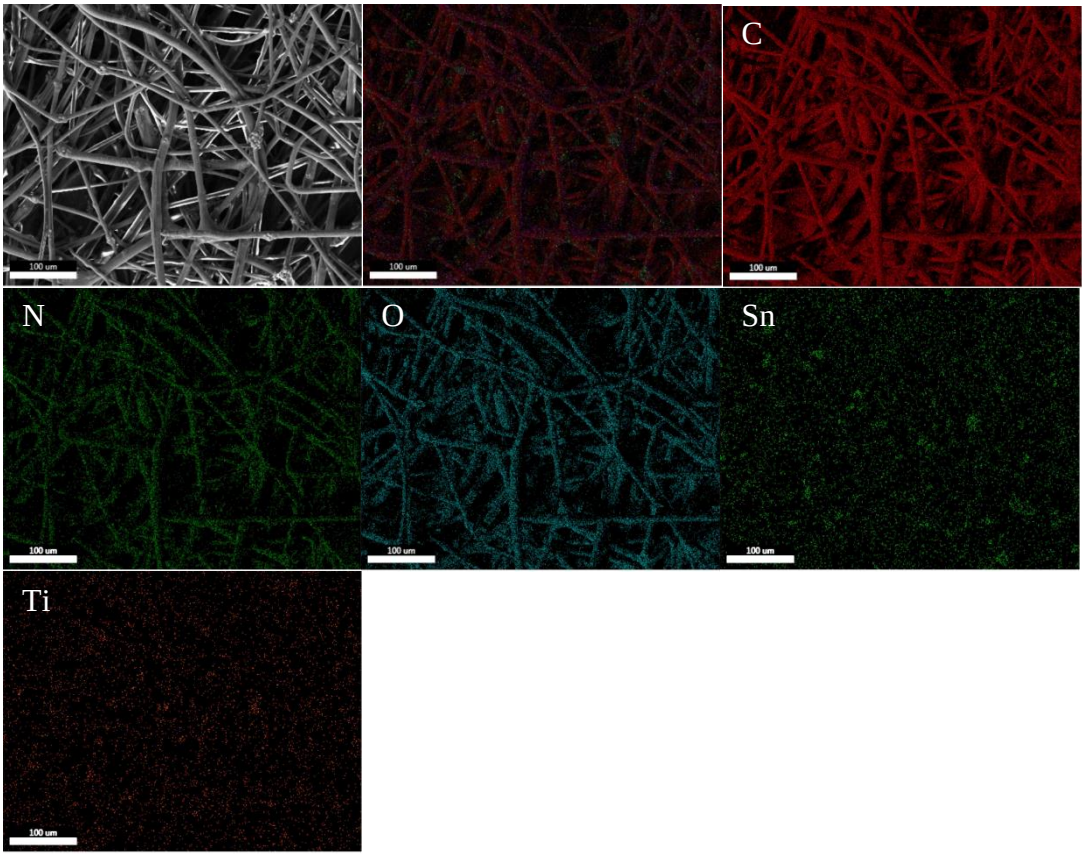

Figure 54: EDS mapping of SnO_2/TiO_2 PVP fibers (3:2).

Table 16: EDS mapping results of SnO_2/TiO_2 (2:1) pre-calcined fibers.

Element	Weight %	Atomic %	Net Int.	Error %	Kratio	Z	A	F
C K	59.45	87.26	642.90	5.66	0.5121	1.1828	0.7283	1.0000
O K	7.65	8.43	55.55	20.16	0.0296	1.1202	0.3449	1.0000
AuM	19.49	1.74	96.04	11.97	0.1324	0.5804	1.1677	1.0020
SnL	10.81	1.61	24.82	30.21	0.0718	0.6506	1.0208	1.0006
TiK	2.59	0.95	6.86	65.94	0.0211	0.8356	0.9810	0.9948

Table 17: EDS mapping results of SnO_2/TiO_2 (3:1) pre-calcined fibers.

Element	Weight %	Atomic %	Net Int.	Error %	Kratio	Z	A	F
C K	53.99	85.32	538.92	5.95	0.4649	1.2173	0.7073	1.0000
O K	7.77	9.22	54.86	18.83	0.0317	1.1537	0.3532	1.0000
AuM	21.36	2.06	99.32	14.06	0.1484	0.5990	1.1571	1.0024
SnL	13.91	2.22	30.25	29.23	0.0950	0.6725	1.0151	1.0006
TiK	2.97	1.18	7.46	64.91	0.0249	0.8647	0.9754	0.9947

Table 18: EDS mapping results of SnO_2/TiO_2 (3:2) pre-calcined fibers.

Element	Weight %	Atomic %	Net Int.	Error %	Kratio	Z	A	F
C K	58.72	86.50	608.88	5.59	0.5109	1.1816	0.7364	1.0000
O K	7.87	8.71	54.04	19.65	0.0304	1.1190	0.3448	1.0000
AuM	17.77	1.60	82.81	11.94	0.1205	0.5797	1.1665	1.0031
SnL	11.73	1.75	25.47	30.60	0.0780	0.6497	1.0229	1.0008
TiK	3.92	1.45	9.80	43.20	0.0319	0.8344	0.9816	0.9951

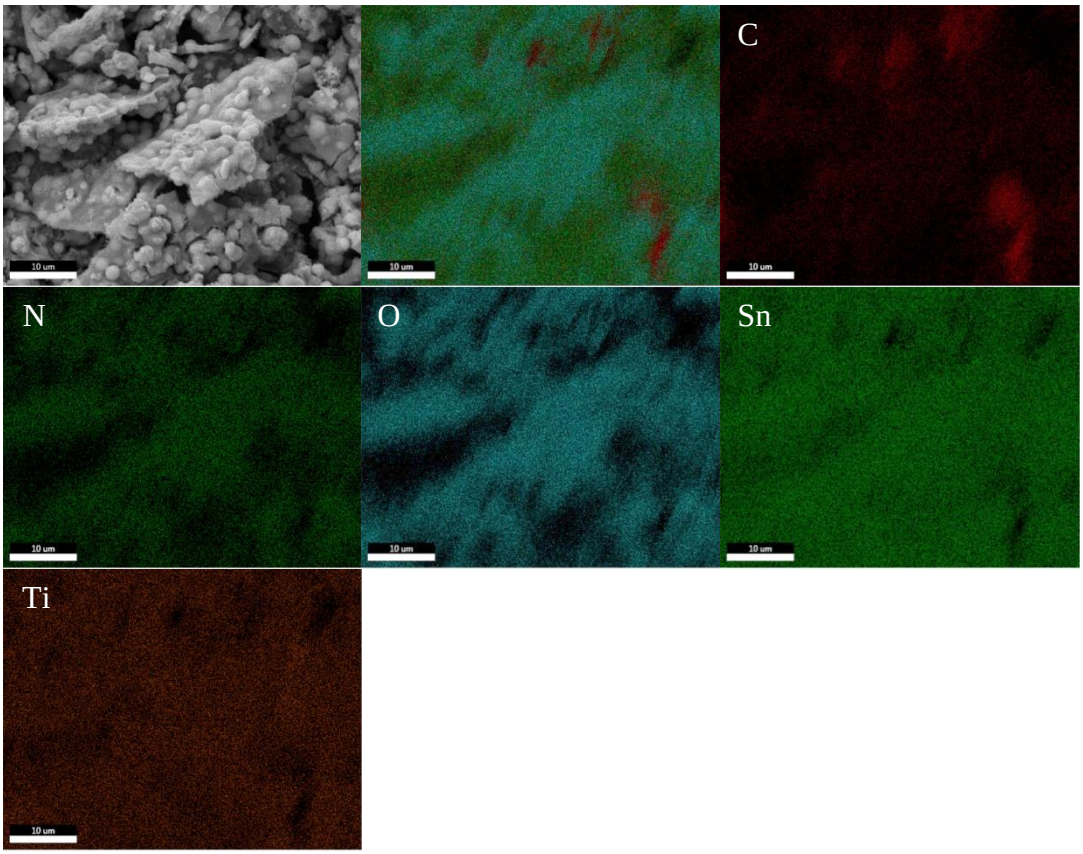

Figure 55: EDS mapping of SnO_2/TiO_2 (1:1) calcined fibers.

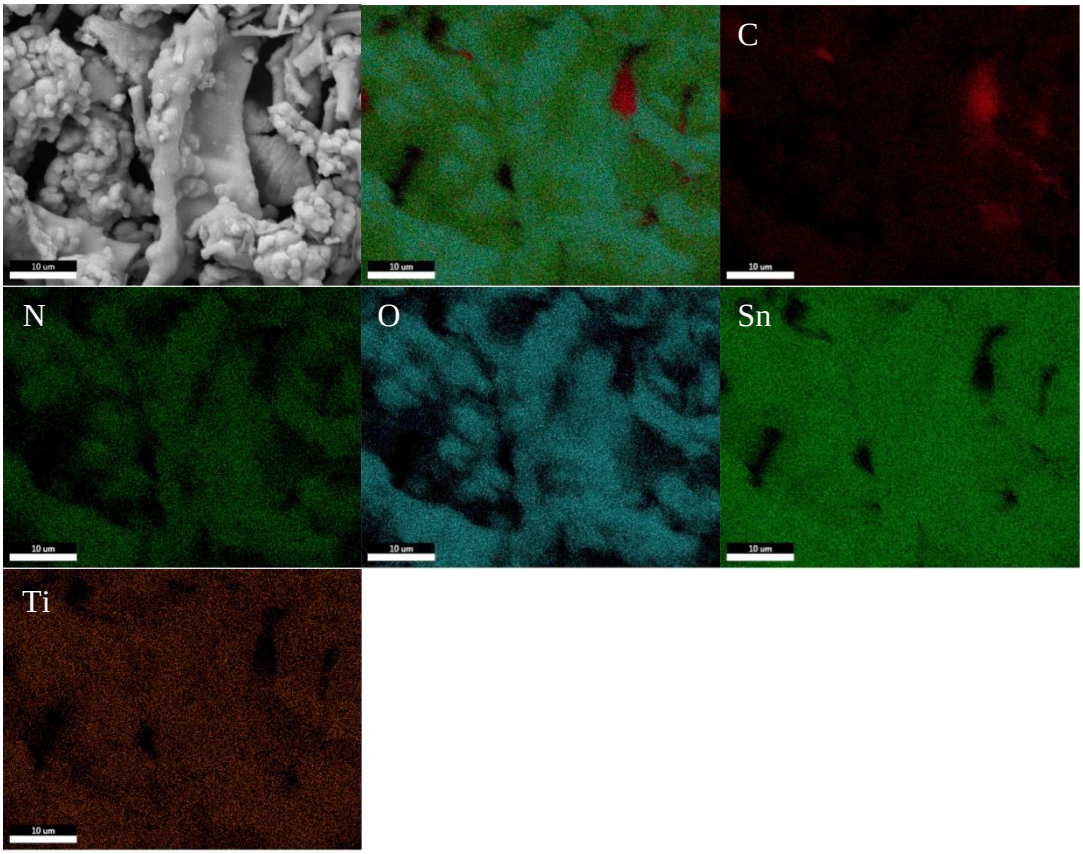

Figure 56: EDS mapping of SnO_2/TiO_2 (2:1) calcined fibers.

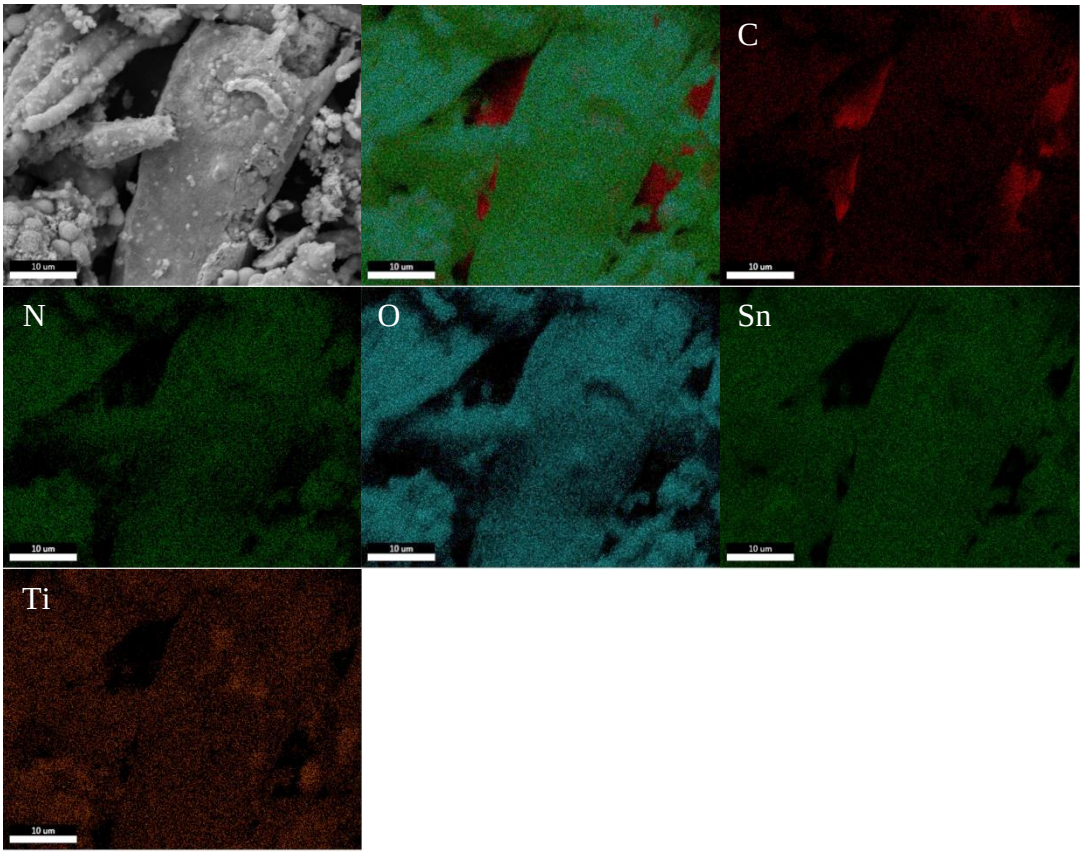

Figure 57: EDS mapping of SnO_2/TiO_2 (3:1) calcined fibers.

Table 19: EDS mapping results of SnO_2/TiO_2 (1:1) calcined fibers.

Element	Weight %	Atomic %	Net Int.	Error %	Kratio	Z	A	F
C K	3.20	11.04	98.70	5.41	0.0314	1.4332	0.6853	1.0000
N K	1.95	5.76	48.70	5.91	0.0193	1.3956	0.7085	1.0000
O K	16.76	43.43	398.70	8.41	0.0833	1.3628	0.3645	1.0000
SnL	53.89	18.82	465.40	3.26	0.4558	0.8218	1.0252	1.0040
TiK	24.20	20.95	252.90	4.54	0.2384	1.0494	0.9356	1.0035

Table 20:EDS mapping results of SnO_2/TiO_2 (2:1) calcined fibers.

Element	Weight %	Atomic %	Net Int.	Error %	Kratio	Z	A	F
C K	2.71	11.14	85.30	5.17	0.0291	1.5030	0.7159	1.0000
N K	2.51	8.87	62.20	5.60	0.0263	1.4635	0.7169	1.0000
O K	12.41	38.38	333.60	7.89	0.0746	1.4294	0.4207	1.0000
SnL	70.56	29.41	594.70	3.23	0.6241	0.8675	1.0179	1.0017
TiK	11.81	12.20	119.00	5.35	0.1202	1.1109	0.9129	1.0037

Table 21: EDS mapping results of SnO_2/TiO_2 (3:1) calcined fibers.

Element	Weight %	Atomic %	Net Int.	Error %	Kratio	Z	A	F
C K	2.69	11.59	82.70	5.09	0.0296	1.5210	0.7248	1.0000
N K	2.63	9.71	62.70	5.59	0.0279	1.4811	0.7172	1.0000
O K	11.40	36.90	308.40	7.71	0.0724	1.4465	0.4394	1.0000
SnL	74.88	32.69	607.90	3.20	0.6696	0.8793	1.0159	1.0011
TiK	8.41	9.10	81.40	5.89	0.0863	1.1269	0.9072	1.0037

BIOGRAPHICAL SKETCH

David A. Sanchez was born on July 18th, 1989, in Pharr, Texas. He lives with his wife Chanel Lee Borrego, and son Elam Aureliano Sanchez at 901 San Cristobal St, San Juan, Texas. David has always had a passion for mathematics and took advanced courses during his time at PSJA Memorial High School. After graduating high school in 2007, he went on to the University of Texas at Austin, where he completed his Bachelor of Business Administration (BBA) degree in 2010. He took his degree in finance to work at JPMorgan Chase in Edinburg, Texas, and worked there for almost 10 years before changing his career path. With the support of his wife, he enrolled at the University of Texas Rio Grande Valley in 2017 and completed his Bachelor of Science in Mechanical Engineering (BSME) degree in 2021. Excited to further his education, David enrolled in graduate school at UTRGV the following summer, where he was welcomed onto the lithium-ion battery research team by Dr. Mataz Alcoutlabi. After dedicating two years to research, he graduated with a Master of Science in Mechanical Engineering degree in 2023. David can be reached at dsanchez10@live.com.